

國立交通大學

光電工程研究所

博士論文

平面波導式凹面光柵元件之設計、分析與應用



Design, Analysis, and Application of the Planar  
Waveguide Concave Grating Devices

研究生：林俊廷

指導教授：黃中堯博士  
黃遠東博士

中華民國九十七年七月

# 平面波導式凹面光柵元件之設計、分析與應用

Design, Analysis, and Application of the Planar Waveguide  
Concave Grating Devices

研究生：林俊廷  
指導教授：黃中堯  
黃遠東

Student: Chun-Ting Lin  
Advisor: Dr. Jung-Yaw Huang  
Dr. Yang-Tung Huang

國立交通大學  
光電工程研究所



Submitted to Department of Photonics and Institute of Electro-Optical Engineering

College of Electrical Engineering and Computer Science

National Chiao Tung University

in Partial Fulfillment of the Requirements

for the Degree of

Doctor of Philosophy

in

Electro-Optical Engineering

July 2008

Hsinchu, Taiwan, Republic of China

中華民國九十七年七月

# 平面波導式凹面光柵元件之設計、分析與應用


研究生：林俊廷

指導教授：黃中堯 博士

黃遠東 博士

## 國立交通大學 光電工程研究所

### 摘要



本論文研究平頂 (flat-top) 頻譜響應平面波導式凹面光柵之設計與探討製程誤差之影響。另外，介電質反射面 (dielectric mirrors) 用於平面波導式凹面光柵之反射面和一種新型的光塞取多工器 (optical add/drop multiplexer) 結合平面波導式凹面光柵也被提出與設計。平面波導式凹面光柵解多工器之平頂頻譜響應，是以三聚焦點 (three-focal-point) 和五聚焦點 (five-focal-point) 方法設計。論文中，詳盡討論波導結構和元件的設計流程。三聚焦點的設計方法可以得到最大-1-dB 通帶寬度 (passband width) 為 27.19 GHz 和最小漣波值 (ripple) 為  $5.00 \times 10^{-3}$  dB。五聚焦點的設計方法以多目標函數基因演算法 (multiobjective genetic algorithm) 做最佳化，得到最大-1-dB 通帶寬度為 30.53 GHz 和最小漣波值為  $1.09 \times 10^{-4}$  dB。製程誤差所引起隨機相位和強度的誤差對於元件的影響也有加以評估。為了在光柵反射面達到高反射及低偏振依存性損耗 (polarization-dependent loss)，介電質反射面用於平面波導式凹面光柵的反射面被提出。當使用其設計時，其偏振依存性損耗可以小於 0.05 dB。一種新型的光塞取多工器 (optical add/drop multiplexer) 結合平面波導式凹面光柵被提出，其設計目標為達到較高的自由頻譜範圍 (free spectral range) 以及較小的裸片尺寸 (die size)。其設計的裸片尺寸為  $70 \times 61 \text{ mm}^2$ ，而消光比 (extinction ratio) 可以小於 -59.20 dB。

# Design, Analysis, and Application of the Planar Waveguide Concave Grating Devices

Student: Chun-Ting Lin

Advisor: Dr. Jung-Yaw Huang  
Dr. Yang-Tung Huang

Department of Photonics and Institute of Electro-Optical Engineering

National Chiao Tung University



## ABSTRACT

The design and the impact of the fabrication errors for a flat-top planar waveguide concave grating demultiplexer have been investigated. A planar waveguide concave grating employing dielectric mirrors and a novel optical add-drop multiplexer (OADM) employing a planar waveguide concave grating have been proposed. For the design of a flat-top grating based planar waveguide demultiplexer, the three-focal-point and five-focal-point methods are introduced and analyzed with a design example. The structures and design procedures are discussed in detail. For the three-focal-point method, the highest  $-1$ -dB passband width of 27.19 GHz and the lowest ripple of  $5.00 \times 10^{-3}$  dB are achieved. For the five-focal-point method optimized with the multiobjective genetic algorithm, the highest  $-1$ -dB passband width of 30.53 GHz and the lowest ripple of  $1.09 \times 10^{-4}$  dB are achieved. The impact of fabrication errors, resulting in the random phase and amplitude errors, is also estimated. To yield a high-reflectance and low polarization-dependent loss (PDL), a planar waveguide concave grating employing dielectric mirrors is proposed. The PDL is below 0.05 dB when the proposed dielectric mirrors are used. A novel OADM employing a planar waveguide concave grating for the higher free spectral range (FSR) and smaller die size is proposed. The total die size is  $70 \times 61$  mm<sup>2</sup> with the extinction ratios less than  $-59.20$  dB.

## Acknowledgement

I am gratefully thankful for the assistance of my advisors, Prof. Yang-Tung Huang and Prof. Jung-Yaw Huang, in my research on the integrated optics. They are always with the passion and inspiration as well as the forgiveness of my negligence.

I would like to thank Hui-Hsiung Lin at Industrial Technology Research Institute for the simulation discussions and continuous encouragement and Prof. Cheng-May Kwei for the advice and suggestion. My grateful thanks are due to Profs. Way-Seen Wang, Ching-Ting Lee, Jeng-Yang Chang, Chen-Shiung Chang, and Yin-Chieh Lai for their useful suggestions and comments of my dissertation.

My senior colleagues, Prof. Jiun-Shiou Deng, Prof. Ming-Feng Lu, Dr. Shih-Hsin Hsum, and Mr. Jiunn-Yann Hsu, gave me a lot of precious suggestions about my research, and my junior colleagues, Yu-Lin Yang, Yu-Wei Chang, Jian-Hua Chen, Hsin-Feng Hsu, and other members brings me a lot of happiness in my lab life.

Finally, I give my family the heartfelt gratitude for their support and encouragement, and this dissertation is dedicated to the memory of my parents.



# Contents

List of Tables	vi
List of Figures	vii
<b>1 Introduction</b>	<b>1</b>
<b>2 Analytic Theories for Planar Waveguide Concave Gratings</b>	<b>4</b>
2.1 Transfer-Matrix Method	4
2.1.1 TE Mode of Multilayer Stack	6
2.1.2 TM Mode of Multilayer Stack	10
2.2 Three-type Designs of Concave Gratings	11
2.2.1 Rowland-Circle Type	11
2.2.2 Taylor-Expansion Type	12
2.2.3 Recursive-Definition Type	13
<b>3 Flat-Top Planar Waveguide Demultiplexer</b>	<b>15</b>
3.1 Three-Focal-Point Method	15
3.1.1 Modified Formula Based on Gaussian Approximation	16
3.1.2 Design Example and Numerical Analysis	17
3.2 The Impact of Fabrication Errors	32
3.3 Five-Focal-Point Method	38
3.3.1 Design Formulas and Design Example	39
3.3.2 Numerical Analysis	41
3.4 Summary	46
<b>4 Planar Waveguide Concave Grating Employing Dielectric Mirrors</b>	<b>47</b>
4.1 Transfer-Matrix Analysis	47

4.2	2D Waveguide Analysis . . . . .	52
4.3	Summary . . . . .	55
<b>5</b>	<b>16-Channel Optical Add-Drop Multiplexer</b>	<b>57</b>
5.1	Structure and Design Considerations . . . . .	57
5.2	Design Example and Characteristics . . . . .	62
5.3	Summary . . . . .	66
<b>6</b>	<b>Conclusion</b>	<b>67</b>
<b>A</b>	<b>Characteristic Matrix</b>	<b>69</b>
<b>B</b>	<b>Modified Formula</b>	<b>70</b>
	<b>Bibliography</b>	<b>73</b>



# List of Tables

4.1 Bandwidth results of the high-reflectance region in a Littrow mount with  $N_{\text{slot}}$  of 15 and  $\lambda_0$  of 1544.69 nm . . . . . 51





# List of Figures

2-1	Schematic figure of the multilayer stack waveguide with the substrate index of $n_s$ and cover index of $n_c$ . . . . .	5
2-2	Schematic figure of the Rowland circle. . . . .	11
2-3	Schematic figure of the light diffracted by the concave grating for the Taylor-expansion type. . . . .	12
2-4	Schematic figure of the light diffracted by the concave grating for the recursive-definition type. . . . .	14
3-1	Schematic figure for the three-focal-point method based on the Gaussian approximation. . . . .	18
3-2	Schematic figure of the light propagating in the slab waveguide and being diffracted by the concave grating. . . . .	19
3-3	Cross-sectional views of the input and output channel waveguides. . . . .	20
3-4	Side view of the slab waveguide. . . . .	20
3-5	Propagation loss versus the thickness of the lower cladding layer. . . . .	21
3-6	E-field distribution for the TE mode within the slab waveguide as shown in Fig. 3-4. . . . .	22
3-7	Cross-sectional power distribution of the fundamental TE mode for the input and output waveguides. . . . .	23
3-8	Cross-sectional power distribution of the fundamental TM mode for the input and output waveguides. . . . .	23
3-9	$E_2/E_1$ versus the optimal half-separation $a$ as $w_{\text{image}} = 1.19w_{\text{outwg}}$ . . . . .	25
3-10	Flattened spectral responses of the design channel for the two cases of the Gaussian approximation and the numerical model as $E_2/E_1 = 0.7$ , $a = 1.52w_{\text{outwg}}$ , and $w_{\text{image}} = 1.19w_{\text{outwg}}$ . . . . .	25

3-11	Total field distribution $E_{\text{image}}$ of the image and the field profile $E_{\text{outwg}}$ of the output fundamental mode at the ending facet of the output waveguide.	27
3-12	−3-dB passband width and the crosstalk versus the ratio $E_2/E_1$ with the channel spacing of 50 GHz for the central channel as $w_{\text{image}} = 1.19w_{\text{outwg}}$ .	27
3-13	Ripple versus the ratio $E_2/E_1$ as $w_{\text{image}} = 1.19w_{\text{outwg}}$ .	28
3-14	Excess loss versus the ratio $E_2/E_1$ as $w_{\text{image}} = 1.19w_{\text{outwg}}$ .	28
3-15	Flattened spectral responses of central five channels with and without the flat-top design for the channel spacing of 50 GHz as $w_{\text{image}} = 1.19w_{\text{outwg}}$ .	29
3-16	$E_2/E_1$ versus the optimal half-separation $a$ as $w_{\text{image}} = w_{\text{outwg}}$ .	30
3-17	$E_2/E_1$ versus the optimal half-separation $a$ as $w_{\text{image}} = 0.88w_{\text{outwg}}$ .	30
3-18	Spectral responses and the chromatic dispersion characteristics with and without the flat-top design as $w_{\text{image}} = 1.19w_{\text{outwg}}$ .	31
3-19	Schematic figure of the light propagating in the slab waveguide and being diffracted by the concave grating.	33
3-20	Field distribution of three subimages at the ending facet of the output waveguide.	35
3-21	Crosstalks of the central channel versus various standard deviations $\sigma_p$ for 50 samples when the channel spacing $\Delta\lambda_{\text{channel}}$ is 0.4 nm (50 GHz).	36
3-22	−1-dB passband widths of the central channel versus various standard deviations $\sigma_p$ for 50 samples when the channel spacing $\Delta\lambda_{\text{channel}}$ is 0.4 nm (50 GHz).	36
3-23	Loss versus the width reduction $\Delta D$ .	37
3-24	Reflectance $R$ versus the side-wall angle offset $\theta$ from the vertical.	37
3-25	Field distribution of the five subimages at the ending facet of the output waveguide.	42
3-26	Maximal fitness in the individual generation.	44
3-27	Spectral responses and the chromatic dispersion characteristics for the three cases.	45
4-1	Side view of the etched trenches for a dielectric mirror.	49
4-2	Top view of a planar waveguide concave grating with dielectric mirrors.	50
4-3	Bandwidth of the high-reflectance region versus $N_{\text{slot}}$ in a Littrow mount with $m_{\text{quar}}$ of 11 at a design wavelength $\lambda_0$ of 1544.69 nm.	50

4-4	Reflectances $R$ for the TE and TM modes versus the corresponding wavelength in a Littrow mount with $m_{\text{quar}}$ of 11 and $N_{\text{slot}}$ of 15 for the transfer-matrix analysis. . . . .	51
4-5	The software layout of the waveguide structure of the etched trenches for one stack. . . . .	53
4-6	Reflectance $R$ versus $D_{\text{etch}}$ in a Littrow mount with $m_{\text{quar}}$ of 11 and $N_{\text{slot}}$ of 15 at a design wavelength $\lambda_0$ of 1544.69 nm. . . . .	53
4-7	Reflectance $R$ versus $m_{\text{quar}}$ in a Littrow mount with $N_{\text{slot}}$ of 15 and $D_{\text{etch}}$ of 15 $\mu\text{m}$ at a design wavelength $\lambda_0$ of 1544.69 nm. . . . .	54
4-8	Reflectance $R$ versus the corresponding wavelength in a Littrow mount with $m_{\text{quar}}$ of 11, $N_{\text{slot}}$ of 15, and $D_{\text{etch}}$ of 15 $\mu\text{m}$ for the 2D waveguide analysis. . . . .	54
4-9	Loss due to the width variation $\Delta w$ in a Littrow mount with $m_{\text{quar}}$ of 11, $N_{\text{slot}}$ of 15, and $D_{\text{etch}}$ of 15 $\mu\text{m}$ at a design wavelength $\lambda_0$ of 1544.69 nm. . . . .	56
5-1	Schematic configuration of the 16-channel optical add-drop multiplexer system. . . . .	58
5-2	Side views of the single-mode channel waveguide (left) and the slab waveguide (right). . . . .	59
5-3	Schematic figure of the light propagating in the slab waveguide and being diffracted by the concave grating. . . . .	59
5-4	Bending loss versus the radius of the curvature in a $90^\circ$ arc channel waveguide for the fundamental TE mode ( $\text{TE}_0$ ) at a design wavelength of 1550.12 nm. . . . .	64
5-5	16-channel spectral responses for the waves from input port 1 and port 2 coupled to the corresponding $j$ th coupled waveguides. . . . .	64
5-6	16-channel spectral responses for the waves from the corresponding $j$ th coupled waveguides coupled to output port 1 and port 2. . . . .	65
5-7	Transmission characteristics $T_{1'}(f)$ and $T_{2'}(f)$ at output port 1 and port 2. . . . .	66

# Chapter 1

## Introduction

Nowadays, with the explosive growth of Internet the demand for optical bandwidths in the optical telecommunication network is increasing. Wavelength division multiplexing (WDM) systems use each wavelength as a separate channel. With the progress of the laser and the opto-electronic device technology, it is possible to have a high density of wavelengths in a single fiber and it is known as dense wavelength division multiplexing (DWDM). DWDM systems increase the transmission capacity of a fiber by increasing the wavelength channel numbers rather than increasing the data bit rate. International Telecommunications Union Telecommunications standardization Sector (ITU-T) recommends 81 channels (wavelengths) in the C-band starting from 1528.77 nm (196.10 THz) to 1560.61 nm (192.10 THz) with the increment of multiples of 0.39 nm (50 GHz) [1].

Integrated planar waveguide components, such as arrayed waveguide gratings (AWGs) [2–4] and planar waveguide concave (etched) gratings [5–9], are widely used for the demultiplexers/multiplexers in WDM systems due to their advantages of low insertion loss, low crosstalk, high possibilities of mass production, and high spectral resolution. However, arrayed waveguide gratings encounter the inherent limits due to the larger die sizes, the lower free spectral range (FSR), and the higher sensitivity to environment perturbations. In contrast, the sizes of planar waveguide concave gratings can be smaller than those of AWGs because of the geometry of folded beams [10]. Concave gratings have been widely used in spectrographs [5, 8, 10–15] and narrow bandwidth lasers [16].

A conventional planar waveguide demultiplexer gives a sharp spectral response and is temperature sensitive due to the temperature dependence of refractive indices of waveguide materials, which needs the strict temperature control and thus limits the appli-

cations in the WDM system. The athermal design by using a silicone adhesive has been demonstrated [17, 18] but with the complicated fabrication process. Many techniques [3, 7–9, 14, 19–23] have been proposed to simplify the fabrication process by flattening the spectral response of the devices. The temperature tolerance can be improved and the devices with the temperature independent operation can be achieved. For the design of a flat-top planar waveguide demultiplexer, the three-focal-point and five-focal-point methods are introduced and analyzed with a design example. The spectral performance of a demultiplexer is significantly affected by the phase and amplitude errors due to fabrication errors. The impact of fabrication errors on a flat-top grating based planar waveguide demultiplexer is estimated.

The diffraction efficiency of a conventional metalized grating is polarization dependent due to the induced surface current of the metal. The metal coating on the shaded facet is the main source of the PDL while it does not contribute to the improvement of the diffraction efficiency especially in a Littrow mount [24]. However, the induced surface current does not exist in a dielectric-air interface. To yield a high-reflectance and low polarization-dependent loss (PDL), a planar waveguide concave grating employing dielectric mirrors is proposed.

An optical add-drop multiplexer (OADM) is capable of transmitting and dropping the wavelength signals selectively and is a key component in fiber-to-the-home (FTTH) systems. In a conventional design, an OADM employs arrayed-waveguide gratings [2, 25]. A novel 16-channel OADM employing a planar waveguide concave grating is proposed for the higher FSR and smaller die size.

In Chapter 2, analytical theories for planar waveguide concave gratings are briefly reviewed. The multilayer stack theory for solving the dispersion relation of a multilayer slab waveguide is introduced. The effective indices of the TE and TM modes can be obtained from the solution of the root for the dispersion relation of a multilayer slab waveguide. Three-type designs of the concave gratings including Rowland-circle type, Taylor-expansion type, and recursive-definition type are also introduced.

In Chapter 3, a three-focal-point method is introduced for a flat-top planar waveguide demultiplexer. With the Gaussian approximation, a modified formula with respect to [7] is proposed and is compared with the numerical model of the scalar diffraction theory by using a design example. We also estimate the impact of fabrication errors on a flat-

top grating-based planar waveguide demultiplexer [26]. For the further improvement of the  $-1$ -dB-passband width and ripple, a five-focal-point method is also introduced for a flat-top planar waveguide demultiplexer and is optimized by the genetic algorithm [9,27].

In Chapter 4, a planar waveguide concave grating employing dielectric mirrors is proposed to yield a high-reflectance and low polarization-dependent loss (PDL) [28]. The transfer-matrix method is used to derive an expression for the reflectance  $R$  of a series of air slots and high-index stacks. The FullWAVE software, a finite difference time-domain EM Solver from R-Soft, is used to evaluate the loss of the resulting 2D waveguide grating.

In Chapter 5, a novel optical add-drop multiplexer (OADM) employing a planar waveguide concave grating is proposed. The arrangements of the components and the design considerations of the concave grating is discussed in detail and the bending loss is also taken into consideration. The proposed scheme is illustrated with a design example and the transmission characteristics of the light detected at the output port are analyzed.

In Chapter 6, we give some discussions and conclusions of the study as well as the suggestions for future work.



# Chapter 2

## Analytic Theories for Planar Waveguide Concave Gratings

In this chapter, analytic theories for the planar waveguide concave gratings are briefly reviewed. Planar waveguide concave (etched) gratings are widely used for the planar waveguide demultiplexers/multiplexers. The slab waveguide structure consists of the high-index core layer with the upper and lower low-index cladding layers. The theory of the multilayer stacks for solving the dispersion relation of a multilayer slab waveguide is introduced [29]. The effective indices of the TE and TM modes can be obtained from the solution of the root for the dispersion relation of a multilayer slab waveguide. Three-type designs of the concave gratings, including Rowland-circle type [30], Taylor-expansion type [31], and recursive-definition type [32], are also introduced.

### 2.1 Transfer-Matrix Method

In source-free, homogeneous, and isotropic media, the wave equations for the time-harmonic electric field  $\mathbf{E}$  and magnetic field  $\mathbf{H}$  can be expressed as:

$$\nabla^2 \mathbf{E} + \omega^2 \mu \epsilon \mathbf{E} = 0, \quad (2.1)$$

$$\nabla^2 \mathbf{H} + \omega^2 \mu \epsilon \mathbf{H} = 0, \quad (2.2)$$

where  $\omega = 2\pi c/\lambda_0$  is the angular frequency,  $c$  is the velocity of the light in vacuum, and  $\lambda_0$  is the wavelength.  $\mu$  and  $\epsilon$  are the magnetic permeability and the dielectric permittivity,

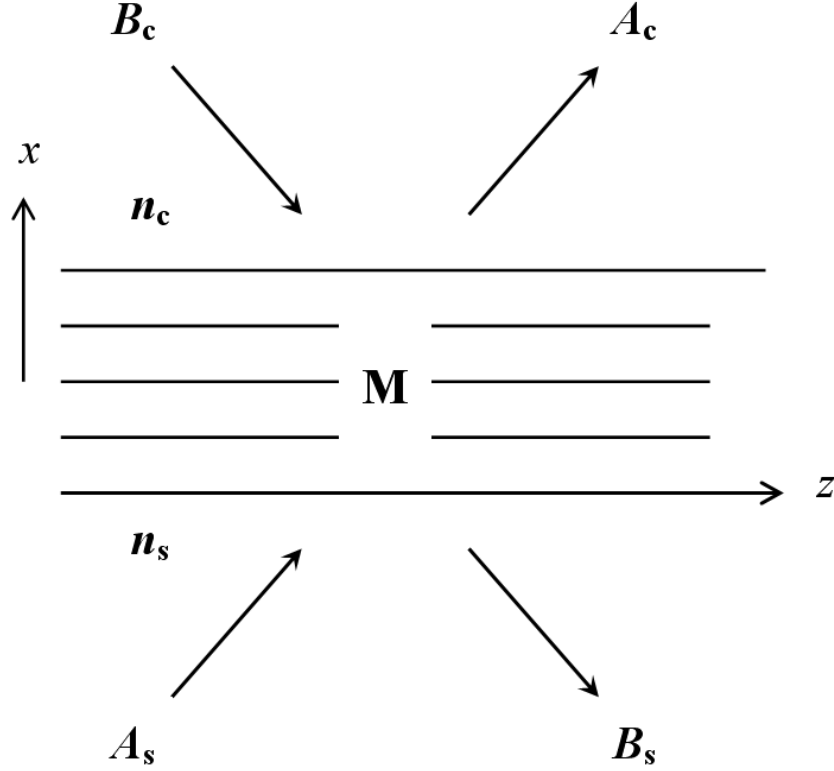


Figure 2-1: Schematic figure of the multilayer stack waveguide with the substrate index of  $n_s$  and cover index of  $n_c$ .

respectively. In the Cartesian coordinate system, suppose that the plane wave propagates along the  $z$ -direction with the propagation constant  $\beta$ . The time-harmonic fields varies as [33]

$$\mathbf{E}(x, y, z) = \mathbf{E}(x, y) \cdot e^{-i\beta z}, \quad (2.3)$$

$$\mathbf{H}(x, y, z) = \mathbf{H}(x, y) \cdot e^{-i\beta z}. \quad (2.4)$$

Inserting Eqs. (2.3) and (2.4) into Eqs. (2.1) and (2.2), the wave equations become

$$\frac{\partial^2 \Psi}{\partial x^2} + \frac{\partial^2 \Psi}{\partial y^2} + [k_0^2 n^2(x, y) - \beta^2] \Psi = 0, \quad (2.5)$$

where  $\Psi$  represents the transverse components  $\mathbf{E}(x, y)$  or  $\mathbf{H}(x, y)$ , and  $k_0 = \omega/c$  is the free space wave number.

In a two-dimensional multilayer slab waveguide as shown in Fig. 2-1, the electromagnetic fields are independent of the  $y$ -axis and the solutions of the wave equations can be classified into two types of modes with mutually orthogonal polarization states. One is the transverse electric (TE) mode with zero longitudinal electric field ( $E_z = 0$ ), and



the other is the transverse magnetic (TM) mode with zero longitudinal magnetic field ( $H_z = 0$ ). In the following subsection, we will introduce the transfer-matrix method, the multilayer stack theory [29], for the TE and TM modes in a multilayer slab waveguide.

### 2.1.1 TE Mode of Multilayer Stack

The theory of the multilayer stacks for the TE mode starts with the following equations:

$$H_x = -\frac{\beta}{\omega\mu} E_y, \quad (2.6)$$

$$H_z = -\frac{1}{i\omega\mu} \frac{\partial E_y}{\partial x}, \quad (2.7)$$

$$-\frac{\partial H_z}{\partial x} - i\beta H_x = i\omega\epsilon E_y, \quad (2.8)$$

$$E_x = E_z = H_y = 0, \quad (2.9)$$

and we define two field variables  $U$  and  $V$  as [29]

$$U \equiv E_y, \quad (2.10)$$

$$V \equiv \omega\mu H_z, \quad (2.11)$$

which describe the transverse variation of the optical field.  $U(x)$  and  $V(x)$  are continuous at the layer boundaries. From Eqs. (2.6)–(2.9), the following relations can be obtained:

$$U' \equiv \frac{\partial U}{\partial x} = -iV, \quad (2.12)$$

$$V' \equiv \frac{\partial V}{\partial x} = i(\beta^2 - k_0^2 n^2)U, \quad (2.13)$$

and

$$U'' \equiv \frac{\partial^2 U}{\partial x^2} = (\beta^2 - k_0^2 n^2)U, \quad (2.14)$$

$$V'' \equiv \frac{\partial^2 V}{\partial x^2} = (\beta^2 - k_0^2 n^2)V, \quad (2.15)$$

where  $n = c\sqrt{\frac{\epsilon}{\epsilon_0}}$  denotes the refractive index. The general solution of the wave equations for the TE mode can be obtained as

$$U = A \exp(-i\kappa x) + B \exp(+i\kappa x), \quad (2.16)$$

$$V = iU' = \kappa[A \exp(-i\kappa x) - B \exp(+i\kappa x)], \quad (2.17)$$

where  $\kappa$  is the transverse propagation constant and is defined as

$$\kappa^2 = k_0^2 n^2 - \beta^2. \quad (2.18)$$

The values of  $U_0 = U(0)$  and  $V_0 = V(0)$  at the input plane  $x = 0$  of the layer can be obtained as

$$U_0 = A + B, \quad (2.19)$$

$$V_0 = \kappa(A - B). \quad (2.20)$$

The constants  $A$  and  $B$  can be replaced by the input quantities,  $U_0$  and  $V_0$ , ie.,

$$A = \frac{1}{2}(U_0 + V_0/\kappa), \quad (2.21)$$

$$B = \frac{1}{2}(U_0 - V_0/\kappa). \quad (2.22)$$

A rearrangement of Eqs. (2.16), (2.17), (2.21), and (2.22) leads to a simple matrix relation between the input variables,  $U_0$  and  $V_0$ , and the output variables,  $U$  and  $V$ , (see Appendix A):

$$\begin{bmatrix} U_0 \\ V_0 \end{bmatrix} = \mathbf{M} \begin{bmatrix} U \\ V \end{bmatrix}, \quad (2.23)$$

where  $\mathbf{M}$  is the transfer matrix of the layer with the form:

$$\mathbf{M} = \begin{bmatrix} \cos(\kappa x) & (i/\kappa) \sin(\kappa x) \\ i\kappa \sin(\kappa x) & \cos(\kappa x) \end{bmatrix}, \quad (2.24)$$

and  $\det \mathbf{M} = 1$ .

We consider a stack of  $n$  layers sandwiched between the substrate and cover, as shown in Fig. 2-1. The layer thickness and index of the  $j$ th layer are  $t_j$  and  $n_j$ , respectively.

The output field variables of the  $j$ th layer are  $U_j$  and  $V_j$ , and the transfer matrix of the  $j$ th layer for the TE mode can be obtained as

$$\mathbf{M}_j = \begin{bmatrix} \cos(\kappa_j t_j) & (i/\kappa_j) \sin(\kappa_j t_j) \\ i\kappa_j \sin(\kappa_j t_j) & \cos(\kappa_j t_j) \end{bmatrix}, \quad (2.25)$$

where  $\kappa_j^2 = k_0^2 n_j^2 - \beta^2$ . The corresponding field variables are related by

$$\begin{bmatrix} U_{j-1} \\ V_{j-1} \end{bmatrix} = \mathbf{M}_j \begin{bmatrix} U_j \\ V_j \end{bmatrix}. \quad (2.26)$$

Using matrix multiplication, we obtain a matrix relation between the input variables,  $U_0$  and  $V_0$ , at the substrate and the output variables,  $U_n$  and  $V_n$ , at the cover:

$$\begin{bmatrix} U_0 \\ V_0 \end{bmatrix} = \mathbf{M} \begin{bmatrix} U_n \\ V_n \end{bmatrix}, \quad (2.27)$$

where  $\mathbf{M}$  is the transfer matrix of the stack, which is obtained from the product of the individual layer matrices and can be expressed as

$$\mathbf{M} \equiv \begin{bmatrix} m_{11} & m_{12} \\ m_{21} & m_{22} \end{bmatrix} = \prod_j \mathbf{M}_j = \mathbf{M}_1 \cdot \mathbf{M}_2 \cdot \mathbf{M}_3 \cdots \mathbf{M}_{n-1}, \quad (2.28)$$

where  $m_{11}$ ,  $m_{12}$ ,  $m_{21}$ , and  $m_{22}$  are the matrix elements which will be used below.

The general solution of the wave equation has been given in Eqs. (2.16) and (2.17). Since there is no light incident from the substrate and cover layers, the fields in the substrate and cover layers can be written as

$$U_0 = B_s, \quad (2.29)$$

$$V_0 = -\kappa_s B_s, \quad (2.30)$$

$$U_n = A_c, \quad (2.31)$$

$$V_n = \kappa_c A_c, \quad (2.32)$$

where the subscripts, s and c, denote the substrate and cover layers. From Eq. (2.27),

the following equations can be obtained:

$$U_0 = m_{11}U_n + m_{12}V_n, \quad (2.33)$$

$$V_0 = m_{21}U_n + m_{22}V_n. \quad (2.34)$$

Inserting Eqs. (2.29)–(2.32) into Eqs. (2.33)–(2.34), the following equations can be obtained:

$$B_s = (m_{11} + \kappa_c m_{12})A_c, \quad (2.35)$$

$$-\kappa_s B_s = (m_{21} + \kappa_c m_{22})A_c. \quad (2.36)$$

Comparing these two relations, the desired dispersion relation for a multilayer slab waveguide can be obtained as

$$\kappa_s (m_{11} + \kappa_c m_{12}) + (m_{21} + \kappa_c m_{22}) = 0. \quad (2.37)$$

This relation establishes the connection between the frequency  $\omega = \kappa c$  of the light and the propagation constant  $\beta$  of the mode guided by the multilayer structure and is valid for any number of layers. The effective index  $n_{\text{eff}}$  of the TE mode can be obtained from the propagation constant  $\beta$  ( $= k_0^2 n_{\text{eff}}^2$ ). In the case where the optical fields in the substrate and cover layers consist of evanescent waves, i.e., guided modes, we have

$$\kappa_s = -i\gamma_s, \quad (2.38)$$

$$\kappa_c = -i\gamma_c, \quad (2.39)$$

and

$$-i\gamma_s (m_{11} - i\kappa_c m_{12}) + (m_{21} - i\gamma_c m_{22}) = 0. \quad (2.40)$$

## 2.1.2 TM Mode of Multilayer Stack

The theory of the multilayer stacks for the TM mode starts with the following equations:

$$E_x = \frac{\beta}{\omega\epsilon} H_y, \quad (2.41)$$

$$E_z = \frac{1}{i\omega\epsilon} \frac{\partial H_y}{\partial x}, \quad (2.42)$$

$$-\frac{\partial E_z}{\partial x} - i\beta E_x = -i\omega\mu H_y, \quad (2.43)$$

$$H_x = H_z = E_y = 0. \quad (2.44)$$

By defining the field variables  $U = H_y$  and  $V = \omega\epsilon_0 E_z$ , the following relations can be obtained as

$$U' = in^2 V, \quad (2.45)$$

$$V' = -i(\beta^2/n^2 - k_0^2)U, \quad (2.46)$$

and

$$U'' = in^2 V' = (\beta^2 - k_0^2 n^2)U, \quad (2.47)$$

$$V'' = -i(\beta^2/n^2 - k_0^2)U' = (\beta^2 - k_0^2 n^2)V. \quad (2.48)$$

The general solution of the wave equation for the TM mode can be obtained as

$$U = A \exp(-i\kappa x) + B \exp(+i\kappa x), \quad (2.49)$$

$$V = -iU'/n^2 = -(\kappa/n^2)[A \exp(-i\kappa x) - B \exp(+i\kappa x)]. \quad (2.50)$$

The comparison between Eqs. (2.16), (2.17), (2.49) and (2.50) shows that the general TM solution is the same as the general TE solution if we substitute  $-(\kappa/n^2)$  for  $\kappa$  and  $-(\gamma/n^2)$  for  $\gamma$  in the TM mode analysis. The dispersion relation for the TM mode then becomes:

$$-(\kappa_s/n_s^2)[m_{11} - (\kappa_c/n_c^2)m_{12}] + [m_{21} - (\kappa_c/n_c^2)m_{22}] = 0. \quad (2.51)$$

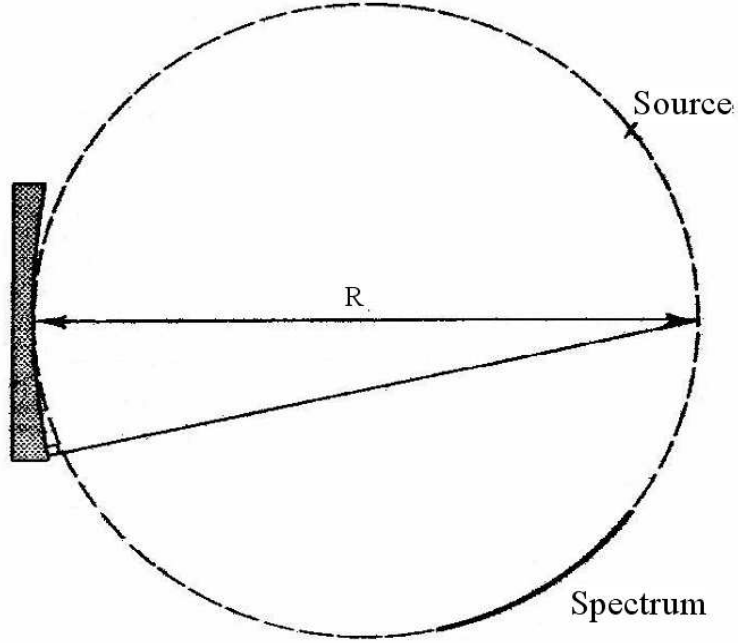


Figure 2-2: Schematic figure of the Rowland circle.

The transfer matrix  $\mathbf{M}_j$  of the  $j$ th layer for the TM mode can be obtained as

$$\mathbf{M}_j = \begin{bmatrix} \cos(\kappa_j t_j) & -i(n_j^2/\kappa_j) \sin(\kappa_j t_j) \\ -i(\kappa_j/n_j^2) \sin(\kappa_j t_j) & \cos(\kappa_j t_j) \end{bmatrix}. \quad (2.52)$$

## 2.2 Three-type Designs of Concave Gratings

In this section, three-type designs of the concave gratings, including Rowland-circle type [30], Taylor-expansion type [31], and recursive-definition type [32], are introduced.

### 2.2.1 Rowland-Circle Type

The first type, the Rowland-circle type, was presented by H. A. Rowland in 1882 [30]. Rowland showed that by forming a grating on a spherical concave substrate, the grating itself could perform the task of both dispersing the light and bringing it to a focus. If a point source is located on a circle which touches the pole of the grating, but which has half the radius of curvature of the concave grating, then to a first approximation the diffraction image will also be on that circle. The circle is known as the Rowland circle and is shown in Fig. 2-2 [30].

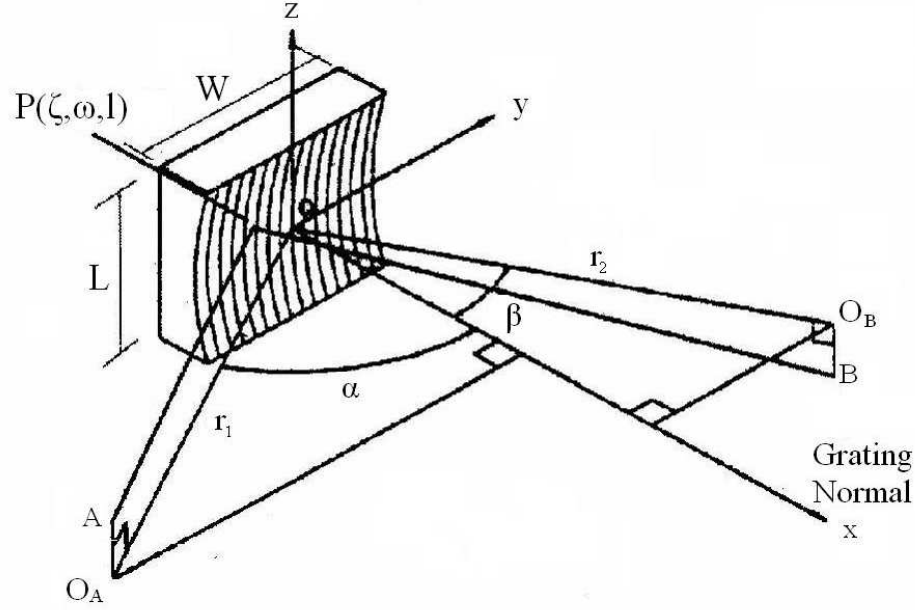


Figure 2-3: Schematic figure of the light diffracted by the concave grating for the Taylor-expansion type.

## 2.2.2 Taylor-Expansion Type

Fig. 2-3 shows the schematic figure of the light diffracted by the concave grating for the Taylor-expansion type [31]. The point source is located at point A and the diffraction image is located at point B. For the ray APB, the optical-path function  $F$  is expressed as

$$F = \overline{AP} + \overline{PB} + im\lambda_0/n_{\text{eff}}, \quad (2.53)$$

where  $i$  denotes the index of the facet,  $m$  denotes the diffraction order,  $\lambda_0$  denotes the design wavelength, and  $n_{\text{eff}}$  denotes the effective index. The  $x$ -axis coordinate position of each groove of the grating can be expressed as

$$\xi = \sum_{i=0}^{\infty} \sum_{j=0}^{\infty} a_{ij} \omega^i \ell^j. \quad (2.54)$$

The grating pole is located at the origin of the coordinates and  $a_{00}$  and  $a_{10}$  are chosen as 0. For the design of the planar waveguide structure, the function  $F$  is designed to be independent of the  $z$ -axis. Taking Eq. (2.54) into Eq. (2.53), the function  $F$  can be expanded by a Taylor series as [31]

$$F = F_{000} + \omega F_{100} + \frac{1}{2} \omega^2 F_{200} + \frac{1}{2} \omega^3 F_{300} + \frac{1}{8} \omega^4 F_{400}. \quad (2.55)$$

Each term in Eq. (2.55) has its representation [31]. The constants  $a_{ij}$  can be resolved by setting higher order terms of the function  $F$  equal to zero but the zeroth order term  $F_{000}$  ( $= r_1 + r_2$ ). Then the free-aberration concave grating, aspheric concave grating, can be achieved and the relation between the  $x$ -axis and  $y$ -axis coordinate positions of the grating groove can be obtained as

$$\xi = a_{20} \omega^2 + a_{30} \omega^3 + a_{40} \omega^4. \quad (2.56)$$

### 2.2.3 Recursive-Definition Type

The third type, the recursive-definition type, was proposed by K. A. McGreer in 1996 [32] and is more potential and predominate than the other types. One least constraint function must be defined at first. The free-aberration position of the  $i$ th grating groove for a design wavelength of  $\lambda_0$  can be obtained by finding out the solution of the root for the function, i.e.,

$$F(x_i, y_i) = r_{1,i} + r_{2,i} + im\lambda_0/n_{\text{eff}} - r_{1,0} - r_{2,0}, \quad (2.57)$$

where  $r_i$  denotes the distance between  $(a_i, b_i)$  and  $(x, y)$ ,  $r_{j,0}$  denotes the distance between  $(a_j, b_j)$  and  $(x_0, y_0)$  as shown in Fig. 2-4,  $m$  denotes the diffraction order,  $\lambda_0$  denotes the design wavelength, and  $n_{\text{eff}}$  denotes the effective index.



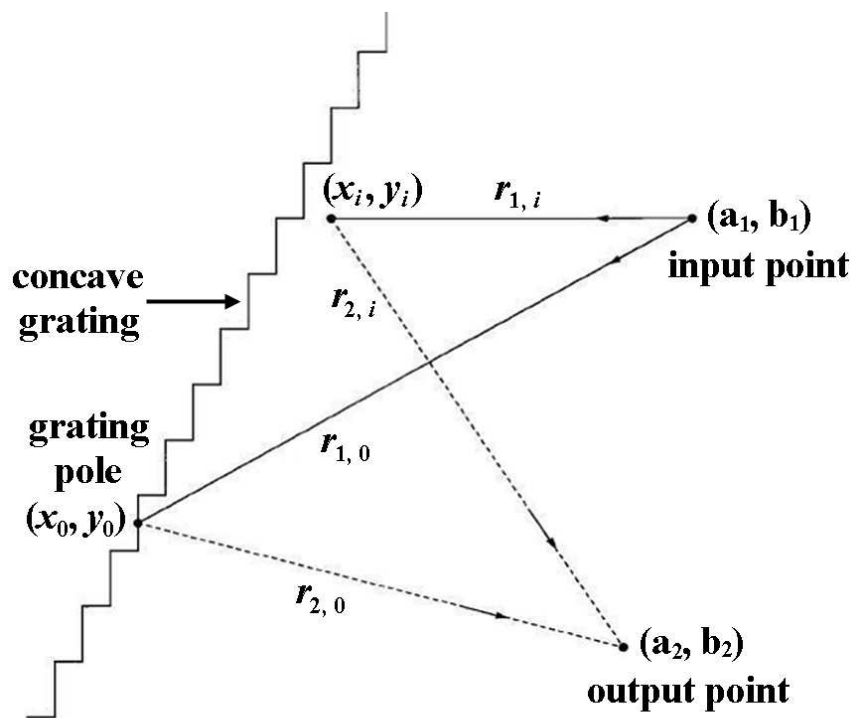


Figure 2-4: Schematic figure of the light diffracted by the concave grating for the recursive-definition type.

# Chapter 3

## Flat-Top Planar Waveguide Demultiplexer

A conventional planar waveguide demultiplexer gives a sharp spectral response and is temperature sensitive due to the temperature dependence of refractive indices of waveguide materials, which limits the applications in the WDM system. Many techniques [3, 7–9, 14, 19–23] have been proposed to overcome the problem by flattening the spectral response of the devices. In this chapter, a three-focal-point method is introduced and analyzed for the design of a flat-top grating based planar waveguide demultiplexer. The impact of the fabrication errors on a flat-top grating based planar waveguide demultiplexer is also estimated. For the further improvement of the  $-1$ -dB passband width and ripple, a five-focal-point method is introduced and the parameters are optimized by the multiobjective genetic algorithm.

### 3.1 Three-Focal-Point Method

A three-focal-point method, which was proposed for a flat-top planar waveguide demultiplexer [7], is used to obtain the flat-top spectral response. With the Gaussian approximation, the formula derived from the reference paper is modified to obtain the optimal half-separation  $a$  when the spot size of each Gaussian subimaging field is different from the effective half width of the output waveguide mode field. The grating is divided into three interleaved subgratings with different focal points and each focal point lies on the cross-sectional line of the ending facet for the output waveguide. Each subgrating forms

subimage with approximately the same spot size and each subimage overlaps with each other.

To obtain a flattened spectral response, the central subimage focuses on the center of the ending facet for the output waveguide and the two outmost subimages are separated from each other with the distance of  $2a$ . For a symmetric spectral response, the peak amplitudes of the field for the two outmost subimages are designed to be identical. With the Gaussian field approximation, the value of the half-separation  $a$  determines the optimal ratio of the peak amplitude for the central subimage and the outmost subimage according to the modified formula. Moreover, a numerical model of the scalar diffraction theory [32] is introduced and used to verify the modified formula with a numerical example. The sources of loss and dispersion characteristics are considered in the numerical calculation.

### 3.1.1 Modified Formula Based on Gaussian Approximation

The grating is composed of three interleaved subgratings with different focal points and each focal point lies on the cross-sectional line of the ending facet for the output waveguide as shown in Fig. 3-1 [7]. Each subimage formed by the corresponding subgrating overlaps with each other. With the Gaussian field approximation, the total field distribution with respect to the center of the ending facet for the output waveguide can be expressed as

$$\begin{aligned}
 E_{\text{image}}(f, x'') = & E_1 \exp \left[ -\frac{(x'' + a - D_s (f - f_0))^2}{w_{\text{image}}^2} \right] \\
 & + E_2 \exp \left[ -\frac{(x'' - D_s (f - f_0))^2}{w_{\text{image}}^2} \right] \\
 & + E_3 \exp \left[ -\frac{(x'' - a - D_s (f - f_0))^2}{w_{\text{image}}^2} \right], \quad (3.1)
 \end{aligned}$$

where  $E_1$ ,  $E_2$ , and  $E_3$  denote the peak amplitudes of the three subimages, respectively,  $a$  denotes the half-separation between the two outmost subimages,  $D_s$  denotes the spatial dispersion coefficient of the grating along the  $x''$ -axis,  $f$  denotes the frequency of the light,  $f_0$  denotes the central frequency, and  $w_{\text{image}}$  denotes the spot size (the effective half-width at  $1/e$  amplitude) of each Gaussian subimage (the spot sizes for three subimages are supposed to be identical if the subgratings are interleaved). To obtain a symmetric

spectral response,  $E_1$  and  $E_3$  are designed to be identical. The effective half widths of the input and output waveguides for the fundamental modes are  $w_{\text{inwg}}$  and  $w_{\text{outwg}}$ , respectively. The spectral response of one channel can be obtained from the following overlap integral over the whole cross section of the ending facet for the output waveguide [7]:

$$I(f) = \left| \int E_{\text{image}}(f, x'') \cdot E_{\text{outwg}}^*(f, x'') dx'' \right|^2, \quad (3.2)$$

where  $E_{\text{outwg}}(f, x'')$  denotes the Gaussian mode field distribution of the output waveguide and has the form:

$$E_{\text{outwg}}(f, x'') = \exp \left[ - \left( \frac{x''}{w_{\text{outwg}}} \right)^2 \right]. \quad (3.3)$$

After the operation of convolution, the spectral response can be expressed as (see Appendix B)

$$I(f) = \left\{ 2E_1 \exp \left[ - \frac{a^2 + D_s^2 (f - f_0)^2}{w_{\text{image}}^2 + w_{\text{outwg}}^2} \right] \cdot \cosh \left[ \frac{2aD_s (f - f_0)}{w_{\text{image}}^2 + w_{\text{outwg}}^2} \right] + E_2 \exp \left[ - \frac{D_s^2 (f - f_0)^2}{w_{\text{image}}^2 + w_{\text{outwg}}^2} \right] \right\}^2. \quad (3.4)$$

To obtain a flat spectral response, the curvature of the spectral response in Eq. (3.2) at the central frequency  $f_0$  should be zero, and the ratio  $E_2/E_1$  can be obtained as (see Appendix B)

$$\frac{E_2}{E_1} = 2 \exp \left( - \frac{a^2}{w_{\text{image}}^2 + w_{\text{outwg}}^2} \right) \cdot \left( \frac{2a^2}{w_{\text{image}}^2 + w_{\text{outwg}}^2} - 1 \right). \quad (3.5)$$

This formula shows that the ratio  $E_2/E_1$  is a function of the half-separation  $a$  when the spot size of each subimage and the effective half width of the output mode field are determined.

### 3.1.2 Design Example and Numerical Analysis

A planar waveguide concave grating based on the recursive definition of facet positions is introduced [32] and it was first proposed by McGreer in 1996. Simulation results show that a concave grating of the classical Rowland circle design suffers from the spherical aberration more seriously than that for the recursive-definition design [34]. The

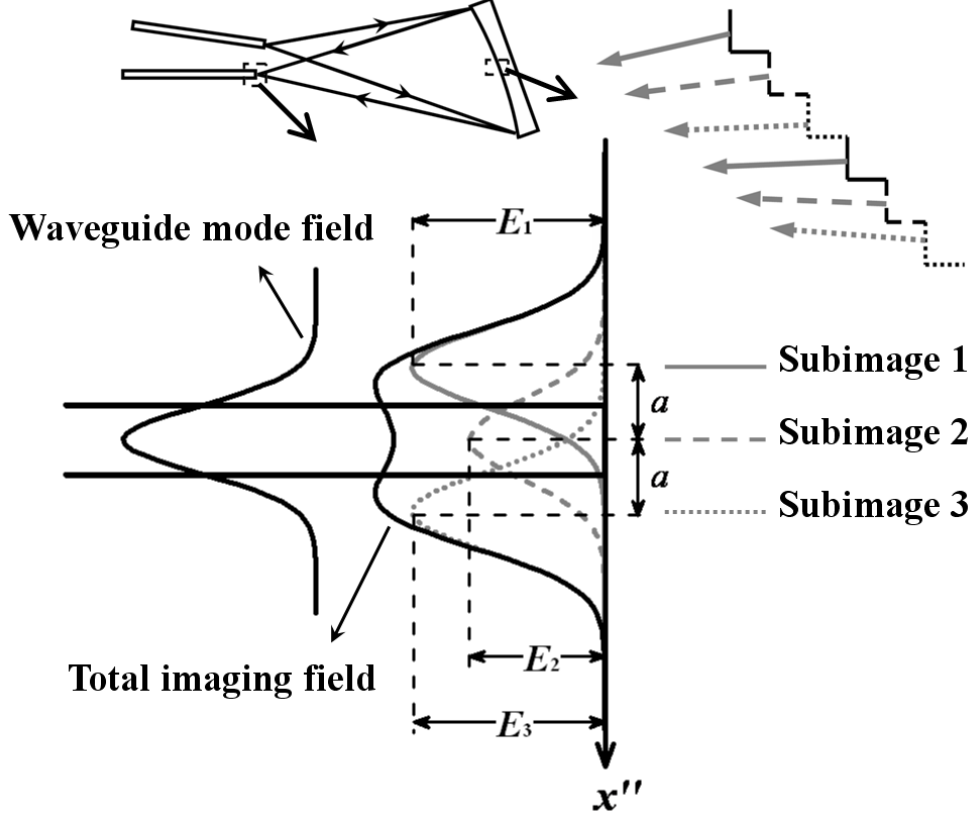


Figure 3-1: Schematic figure for the three-focal-point method based on the Gaussian approximation.

recursive-definition design is more potential and predominate than other designs. One least constraint function must be first defined. The free-aberration position of each groove is determined by the solution of the root for the constraint function as [32]

$$F(x_i, y_i) = r_{1,i} + r_{2,i} + im\lambda_0/n_{\text{eff}} - r_{1,0} - r_{2,0} = 0, \quad (3.6)$$

where  $(x_i, y_i)$  denotes the location of the vertex for the  $i$ th groove,  $r_{j,i}$  denotes the distance between  $(a_j, b_j)$  and  $(x_i, y_i)$  as shown in Fig. 3-2,  $m$  denotes the diffraction order,  $\lambda_0$  denotes the design wavelength, and  $n_{\text{eff}}$  denotes the effective index of the wave propagating in the slab waveguide.

The tilt angle  $\theta_i$  of the  $i$ th facet with respect to the  $x$ -axis is determined by the following equation [32]:

$$\frac{\partial F(x_i, y_i)}{\partial x} \cos \theta_i + \frac{\partial F(x_i, y_i)}{\partial y} \sin \theta_i = 0. \quad (3.7)$$

Light launched from the input waveguide is diffracted by the grating, focused to the

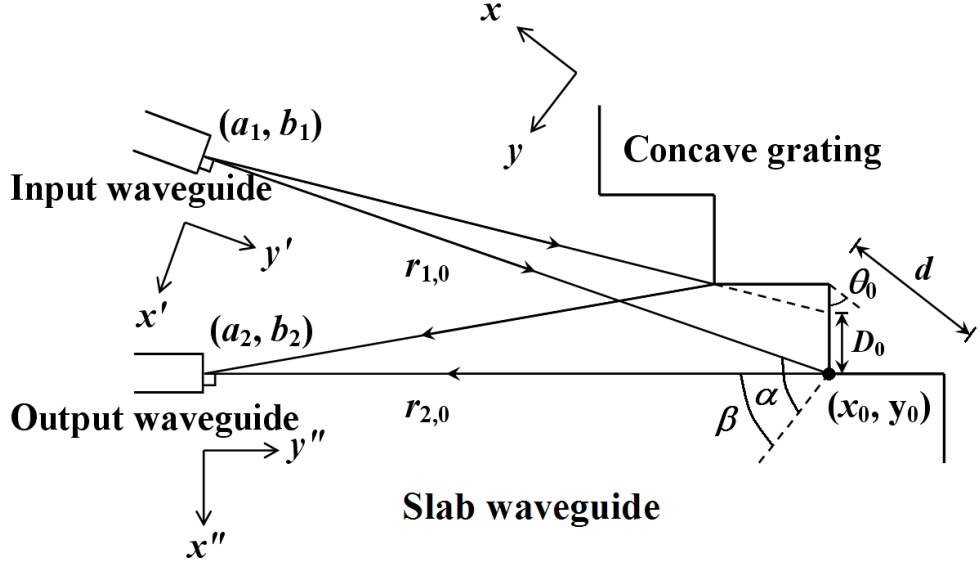


Figure 3-2: Schematic figure of the light propagating in the slab waveguide and being diffracted by the concave grating.

position along the imaging curve, and guided into different output waveguides according to the corresponding wavelengths. The focal equation for the concave grating has the following form [30]:

$$\frac{\cos \alpha}{R} - \frac{\cos^2 \alpha}{r_{1,0}} + \frac{\cos \beta(f)}{R} - \frac{\cos^2 \beta(f)}{r_{2,0}(f)} = 0, \quad (3.8)$$

where  $\alpha$  and  $\beta$  denote the incident angle and the diffraction angle of the input Gaussian beam at the grating pole, respectively,  $R$  is the effective radius of the grating curvature. The numerical model of the scalar diffraction theory for the concave grating in the planar waveguide was first proposed in 1995 [35], and the field formula is used in our analysis:

$$E_{\text{image}}(f, x'') = E_0 \sum_i \frac{D_i n_{\text{eff}} f w_{\text{inwg}} \sqrt{\pi}}{c \sqrt{r_{1,i} \cdot r_{2,i}}} \cdot \exp[-(\gamma/\sigma)^2] \cdot \sin c[kD_i/2 \cdot (\sin \alpha_i + \sin \beta_i)] \cdot \exp[ik(r_{1,i} + r_{2,i}(f))], \quad (3.9)$$

where  $D_i$  denotes the effective facet width of the  $i$ th grating facet,  $w_{\text{inwg}}$  denotes the effective half width of the input waveguide,  $\gamma$  ( $-\sigma \leq \gamma \leq \sigma$ ) denotes the angle from the facet normal of the input waveguide to the  $i$ th grating facet,  $\sigma$  ( $= \lambda_0/\pi n_{\text{eff}} w_{\text{inwg}}$ ) denotes the half angle for the Gaussian beam divergence at  $1/e$  amplitude,  $k$  denotes the propagation constant in the slab waveguide,  $\alpha_i$  and  $\beta_i$  denote the incident angle and the diffraction angle with respect to the  $i$ th grating facet normal, respectively.

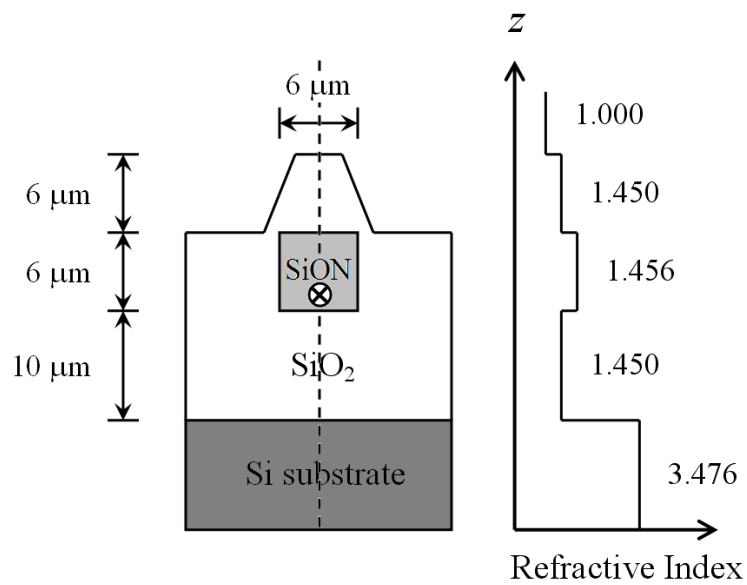


Figure 3-3: Cross-sectional views of the input and output channel waveguides.

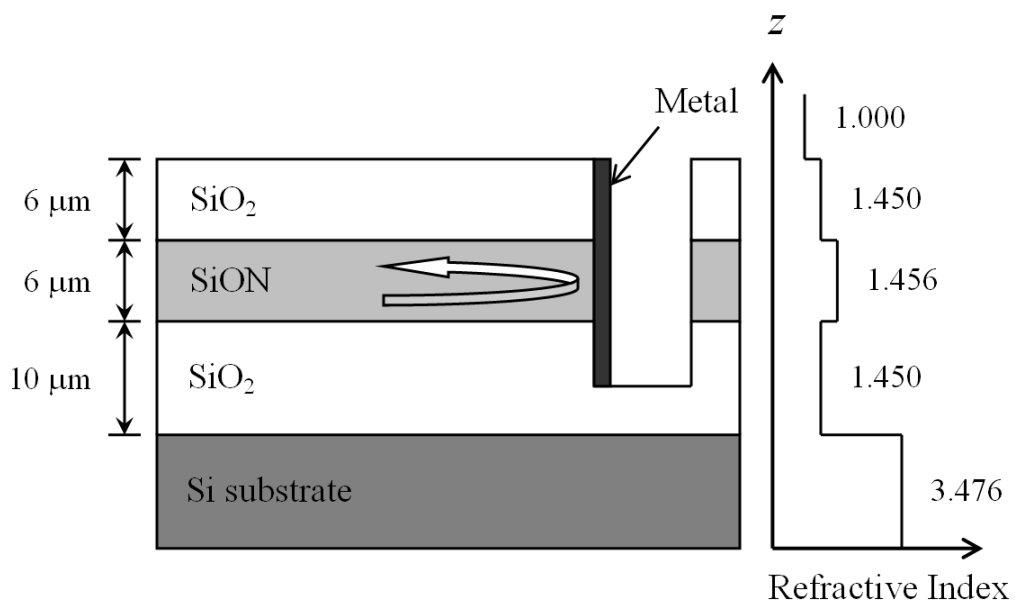


Figure 3-4: Side view of the slab waveguide.

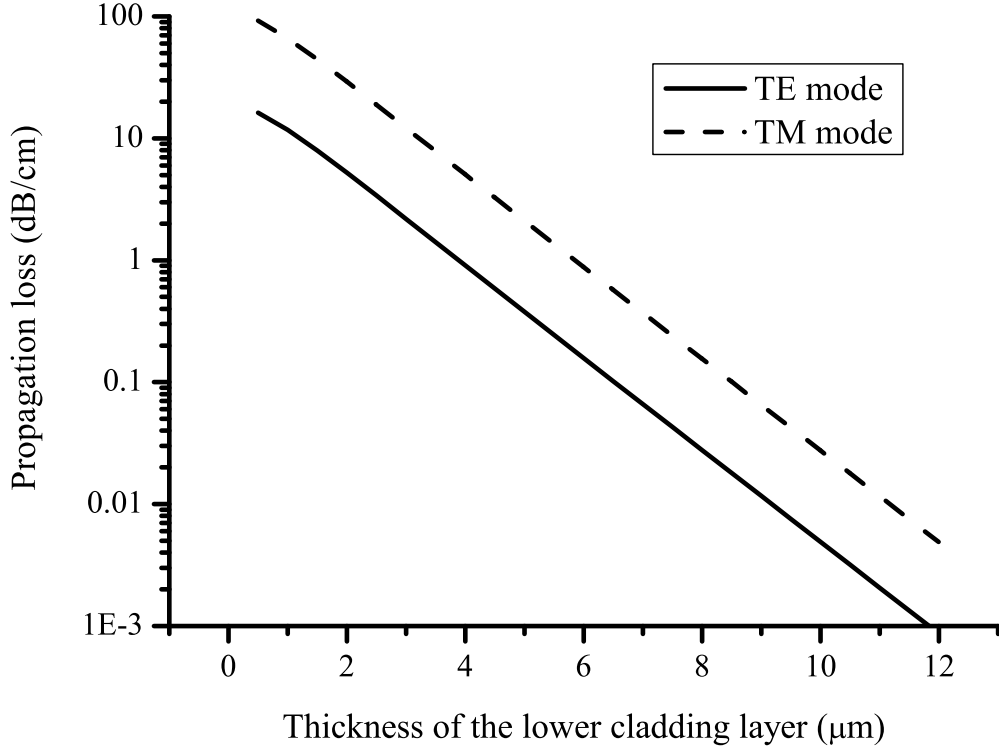


Figure 3-5: Propagation loss versus the thickness of the lower cladding layer.

A design example of the concave grating in silica-on-silicon is used to illustrate the three-focal-point method. The input and output channel waveguides consist of the SiON core layer with a  $6 \times 6\text{-}\mu\text{m}^2$  cross-sectional area surrounded by the SiO<sub>2</sub> cladding layer as shown in Fig. 3-3. The slab waveguide consists of a 6- $\mu\text{m}$ -thick SiON core layer with the upper 6- $\mu\text{m}$ -thick and lower 10- $\mu\text{m}$ -thick SiO<sub>2</sub> cladding layers as shown in Fig. 3-4. The grating is achieved by etching a trench to the lower cladding layer and then coated with metal at the back wall. Therefore, light is reflected, diffracted, and focused by the metalized concave grating.

The following parameters are chosen:  $n_{\text{core}} = 1.456$  for the refractive index of the core layer,  $n_{\text{cladding}} = 1.450$  for the refractive index of the cladding layer,  $n_{\text{si}} = 3.476$  for the refractive index of the silicon substrate at an operating wavelength of 1550.12 nm, the effective numerical aperture NA of 0.13 for the input waveguide which is the same as that for the commercial single-mode fiber, 81 channels in the C-band with the channel spacing  $\Delta\lambda_{\text{channel}} = 0.4$  nm (50 GHz) from 1528.77 nm to 1560.61 nm according to ITU grids [1],  $\alpha = 60^\circ$  for the incident angle at the grating pole, the diffraction order  $m = 16$ ,  $d = 10$   $\mu\text{m}$  for the period of the grating facet blazed at an angle obtained from Eq. (3.7),  $N = 968$  for the total number of periods,  $r_{1,0} = r_{2,0}(f_0) = 35000$   $\mu\text{m}$  for the distances



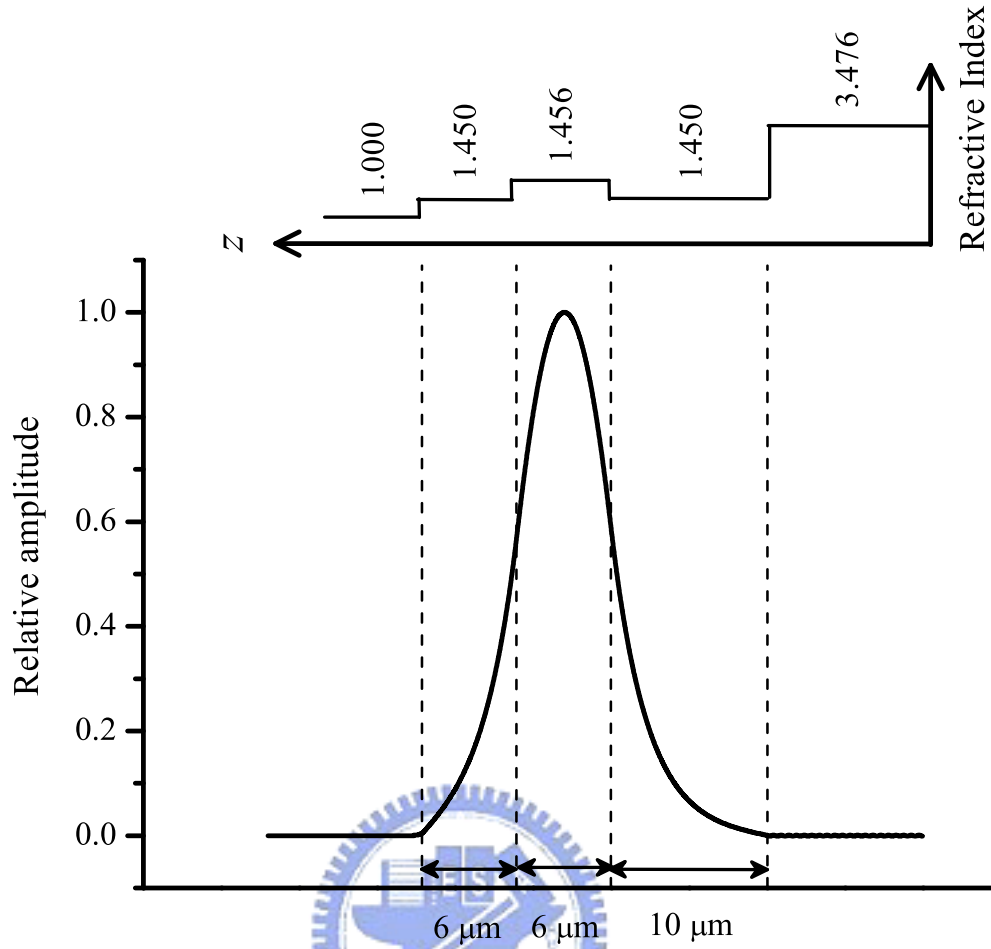


Figure 3-6: E-field distribution for the TE mode within the slab waveguide as shown in Fig. 3-4.

form the end of the input waveguide and the end of the output waveguide of the design wavelength to the grating pole, and  $R = 67011 \mu\text{m}$  for the effective radius of the grating. By using the transfer-matrix method [29], the effective indices of TE and TM modes are obtained as 1.45393 and 1.45392, respectively. The propagation losses due to the leakages to the silicon substrate for both modes are less than 0.03 dB/cm when the thickness of the lower cladding layer is higher than  $10 \mu\text{m}$  as shown in Fig. 3-5.

The E-field distribution for the TE mode within the slab waveguide in Fig. 3-4 is shown in Fig. 3-6. The effective half widths,  $w_{\text{inwg}}$  and  $w_{\text{outwg}}$ , of the input and output waveguides for the fundamental modes along the  $x'$ -axis and the  $x''$ -axis are  $4.91 \mu\text{m}$  obtained with BeamPROP software from R-Soft and the half angle  $\sigma$  for the beam divergence can be obtained as  $3.96^\circ$ . The cross-sectional power distributions of the fundamental TE and TM modes for the input and output waveguides are shown in Figs. 3-7 and 3-8. The spot size  $w_{\text{image}}$  of each subimage along the  $x''$ -axis is  $5.85 \mu\text{m}$ .

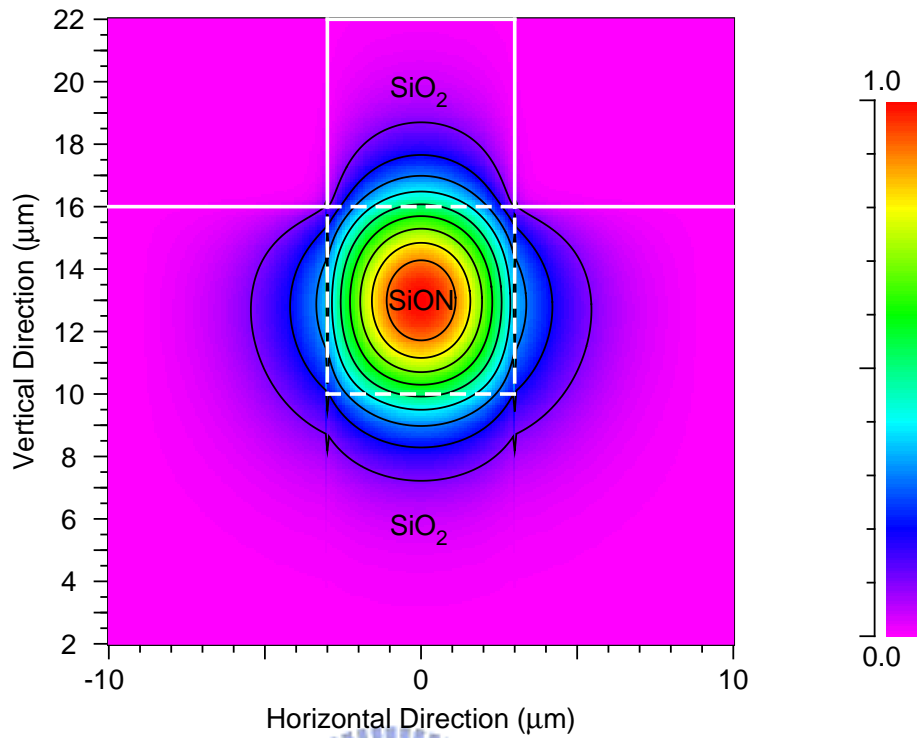


Figure 3-7: Cross-sectional power distribution of the fundamental TE mode for the input and output waveguides.

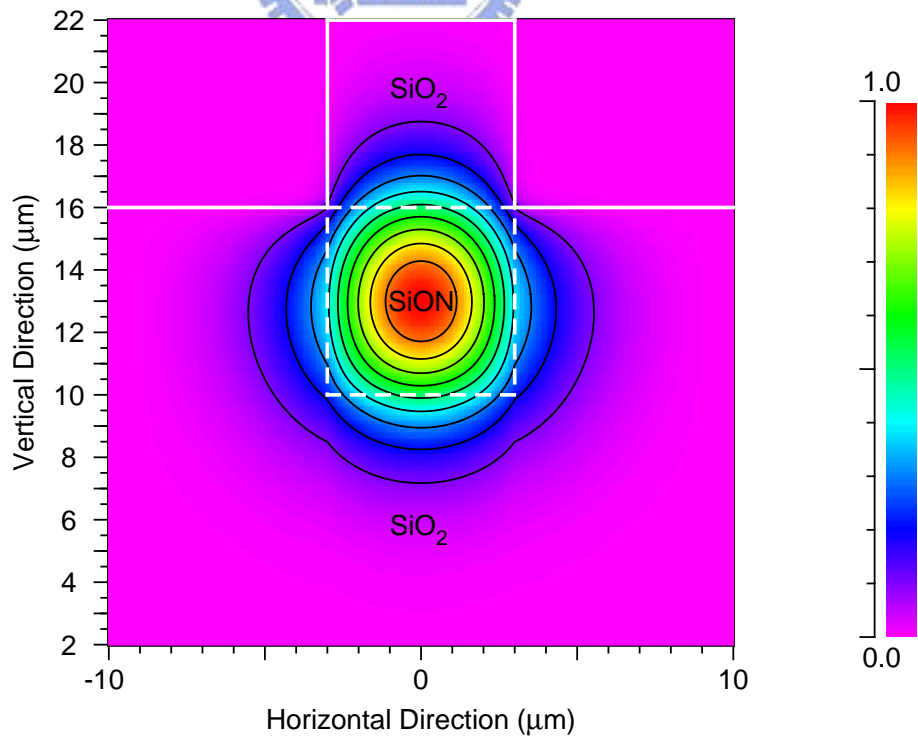


Figure 3-8: Cross-sectional power distribution of the fundamental TM mode for the input and output waveguides.

The spectral response of each channel can be obtained from the overlap integral over the whole cross section of the ending facet for the output waveguide:

$$I(f) = \frac{|\int E_{\text{image}}(f, x'') \cdot E_{\text{outwg}}^*(f, x'') dx''|^2}{\int |E_{\text{image}}(f_0, x'')|^2 dx'' \cdot \int |E_{\text{outwg}}(f_0, x'')|^2 dx''} \cdot \Gamma, \quad (3.10)$$

where  $\Gamma$  denotes the loss attributed to the grating or the waveguide including the undesired-order loss and the propagation loss. Here, the fiber coupling loss is not considered. The undesired-order loss, which comes from the diffraction of light into undesired adjacent orders, is one of the main sources of loss.

To make a comparison between the modified formula derived in Eq. (3.5) and the numerical modeling of the scalar diffraction theory for the three-focal-point method, we take the TE mode for example. All computer program codes for the simulation are written in Fortran 90. If the subgratings are interleaved, the ratio of the peak amplitudes of the subimages is approximately equal to the ratio of the facet numbers of the corresponding subgratings [7]. So we can adjust the ratio of the facet numbers of subgrating 2 and subgrating 1 to adjust the ratio  $E_2/E_1$ . If the grating pole is located at the origin of the coordinates, after determining the arrayed sequence of the facets of the subgratings the  $x$ -axis coordinate position of the vertex of the  $i$ th groove can be obtained as

$$x_i = id_k = \frac{im\lambda_k}{n_{\text{eff}} \cdot (\sin \alpha + \sin \beta)}, \quad (3.11)$$

where  $d_k$  denotes the grating period of subgrating  $k$ ,  $m$  denotes the diffraction order,  $\lambda_k$  denotes the central wavelength of subgrating  $k$ ,  $n_{\text{eff}}$  denotes the effective index in the slab waveguide,  $\alpha$  denotes the incident angle at the grating pole, and  $\beta$  denotes the design diffraction angle at the grating pole. The order  $m$  for each subgrating is identical but with the different grating period and central wavelength to obtain a flat-top spectral response. Then the  $y$ -axis coordinate position  $y_i$  can be obtained from the solution of the root for Eq. (3.6). This multigrating method in which each subgrating has its own path-length increment and central wavelength has also been used in the AWG device design [3].

The optimal half-separation  $a$  can be obtained when the spectral response with a minimum ripple is achieved. The ripple is defined as the maximum difference among three extremum points within  $-3$ -dB passband of one channel. Fig. 3-9 shows the

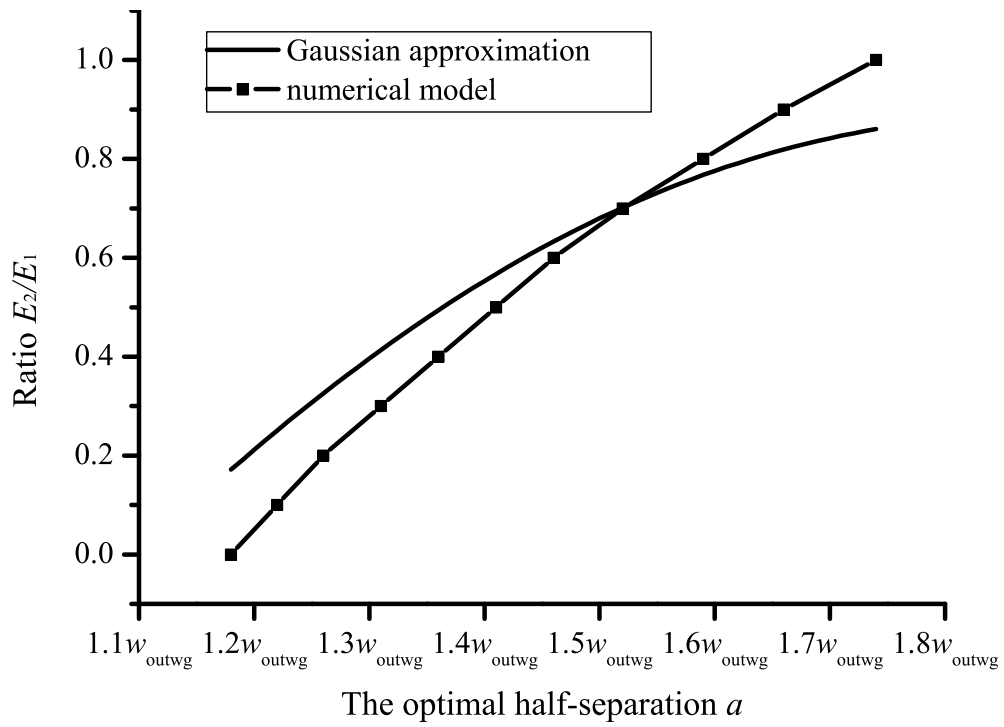


Figure 3-9:  $E_2/E_1$  versus the optimal half-separation  $a$  as  $w_{\text{image}} = 1.19w_{\text{outwg}}$ .

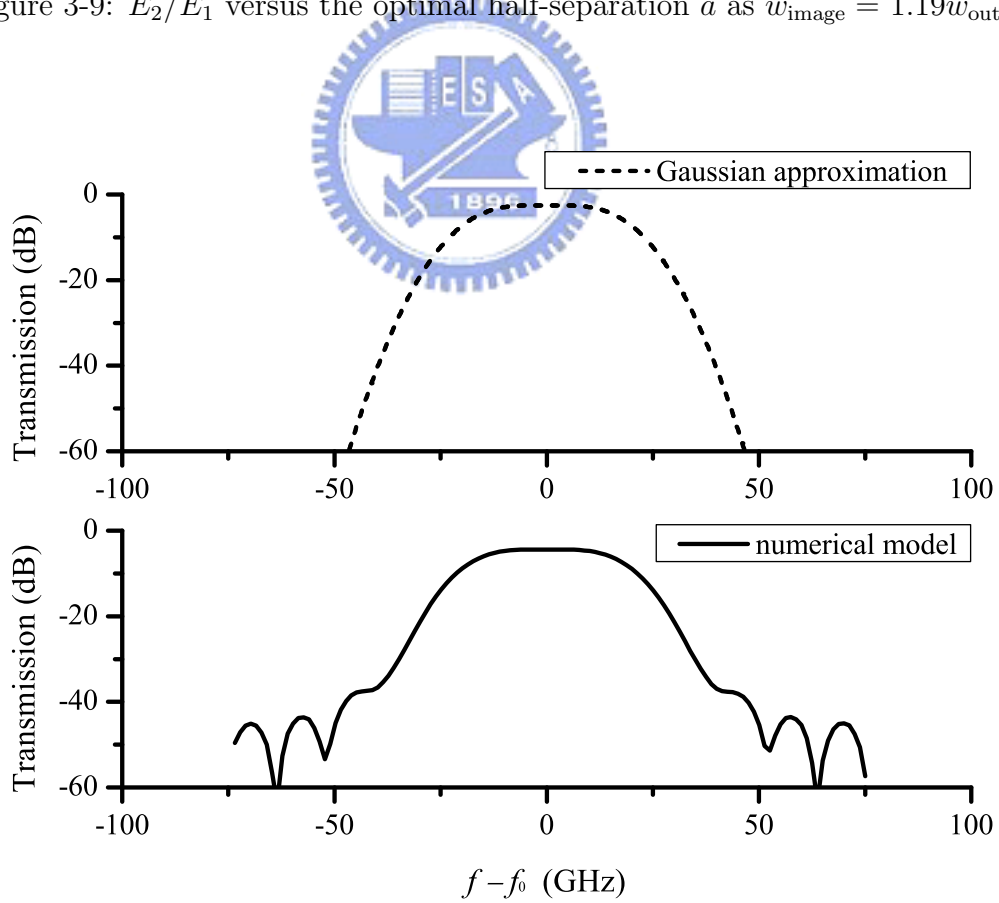


Figure 3-10: Flattened spectral responses of the design channel for the two cases of the Gaussian approximation and the numerical model as  $E_2/E_1 = 0.7$ ,  $a = 1.52w_{\text{outwg}}$ , and  $w_{\text{image}} = 1.19w_{\text{outwg}}$ .

ratio  $E_2/E_1$  as a function of  $a$  for the cases of our numerical model and the Gaussian approximation where the  $x$ -axis is calibrated in  $w_{\text{outwg}}$ . It shows that the deviation between the two curves becomes serious as the ratio  $E_2/E_1$  is close to unity and the two curves have the same  $E_2/E_1$  value of 0.7 when the optimal half-separation  $a$  is  $1.52w_{\text{outwg}}$ . For the case of the Gaussian approximation, only the amplitude term of the imaging field is taken into consideration as shown in Eq. (3.1). For the case of our numerical model, both the amplitude and phase terms of the imaging field are taken into consideration as shown in Eq. (3.9). So there exists the difference between the the two curves for the cases of the Gaussian approximation and the numerical model in Fig. (3-9). Without considering the scattering loss and side-wall tilt loss at the grating facet, the spectral responses of the central channel for the two cases are shown in Fig. 3-10 with the spatial dispersion coefficient  $D_s = 0.569 \mu\text{m}/\text{GHz}$  in our case. The insertion loss for the case of our numerical model is 4.40 dB, where 2.19 dB comes from the excess loss for the flat-top design and 2.21 dB comes from the loss  $\Gamma$  in Eq. (3.10) which is predominated by the undesired-order term. The  $-1$ -dB passband width for the case of the Gaussian approximation is larger than that for the case of our numerical model due to no phase term of the imaging field being taken into consideration. As mentioned in Section 3.1, for a symmetric spectral response the peak amplitudes  $E_1$  and  $E_3$  are designed as identical with identical facet numbers. However,  $E_1$  and  $E_3$  are slightly different due to the different effective widths of adjacent facets and therefore it increases the ripple in the spectral response.

The total field distribution  $E_{\text{image}}$  of the image and the field profile  $E_{\text{outwg}}$  of the output fundamental mode at the ending facet of the output waveguide are shown in Fig. 3-11. To obtain a flat-top spectral response, the imaging field distribution is just like camelback. For the case of our numerical model, the  $-1$ -dB passband width and the crosstalk versus the ratio  $E_2/E_1$  with the channel spacing of 50 GHz for the central channel are shown in Fig. 3-12. It shows that the  $-1$ -dB passband width increases as the ratio  $E_2/E_1$  increases, while the decreased (better) crosstalk is obtained. The  $-1$ -dB passband widths for the ratios  $E_2/E_1$  of 0.0 and 1.0 are 25.80 and 27.19 GHz, respectively. With the temperature coefficient of the refractive index for the silica being  $1 \times 10^{-5} (1/^\circ\text{C})$  [17], the corresponding temperature tolerances for the intensity fluctuation of the central channel below  $-1$  dB can be obtained as  $\pm 9.7$  and  $\pm 10.3$   $^\circ\text{C}$ , respectively.

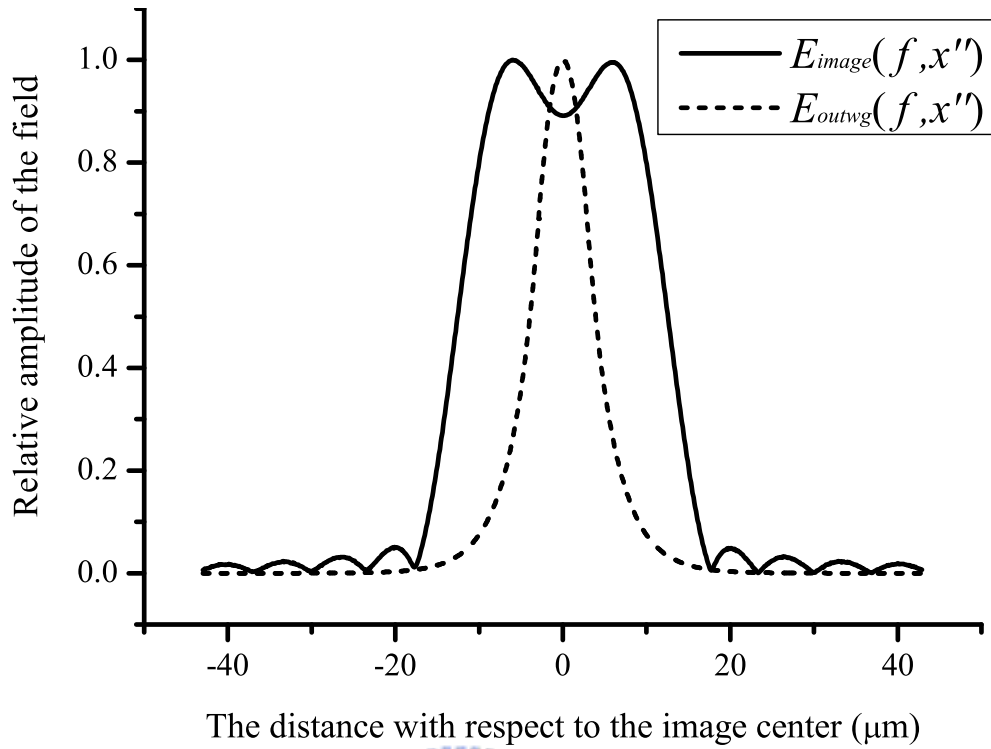


Figure 3-11: Total field distribution  $E_{\text{image}}$  of the image and the field profile  $E_{\text{outwgc}}$  of the output fundamental mode at the ending facet of the output waveguide.

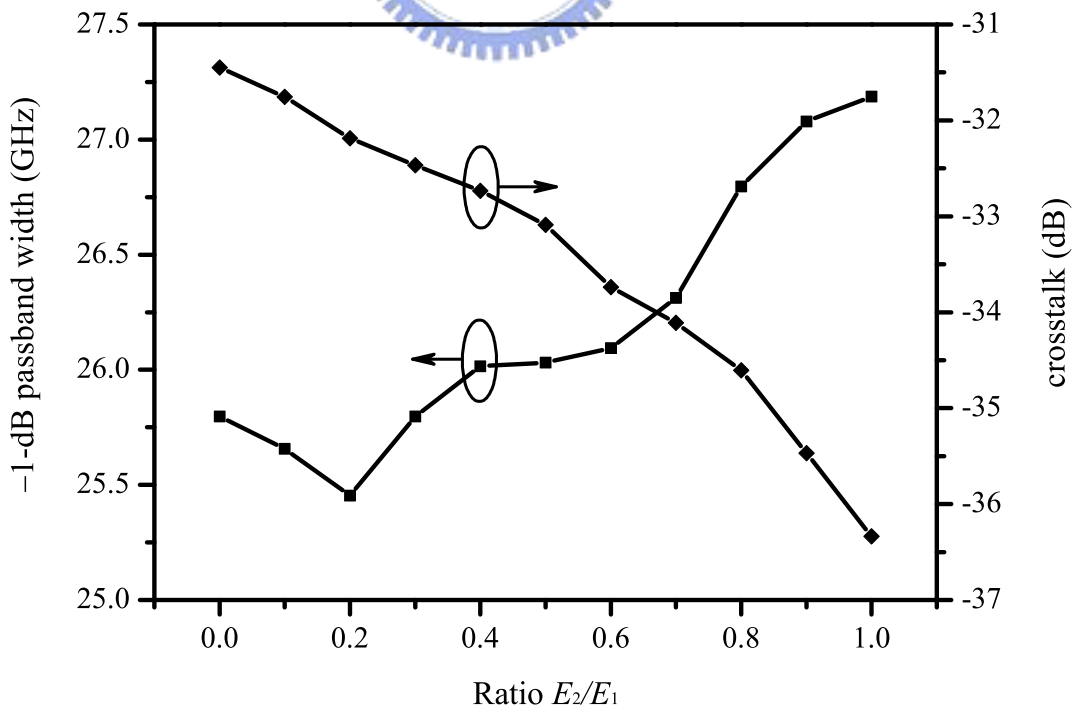


Figure 3-12:  $-3$ -dB passband width and the crosstalk versus the ratio  $E_2/E_1$  with the channel spacing of 50 GHz for the central channel as  $w_{\text{image}} = 1.19w_{\text{outwgc}}$ .

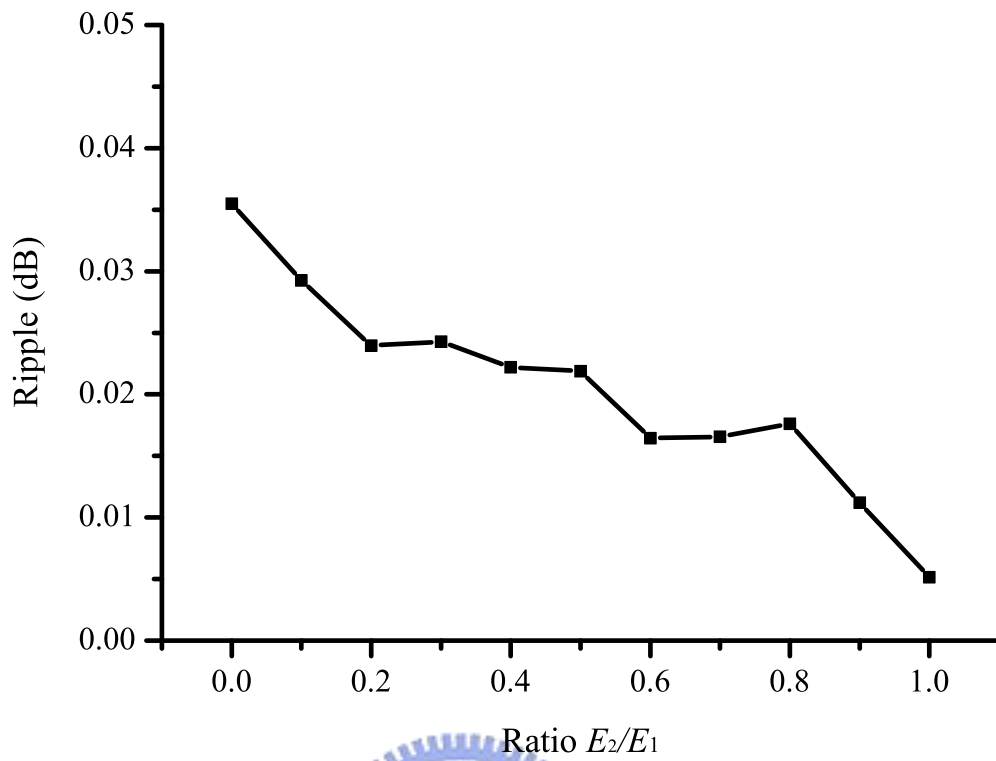


Figure 3-13: Ripple versus the ratio  $E_2/E_1$  as  $w_{\text{image}} = 1.19w_{\text{outwg}}$ .

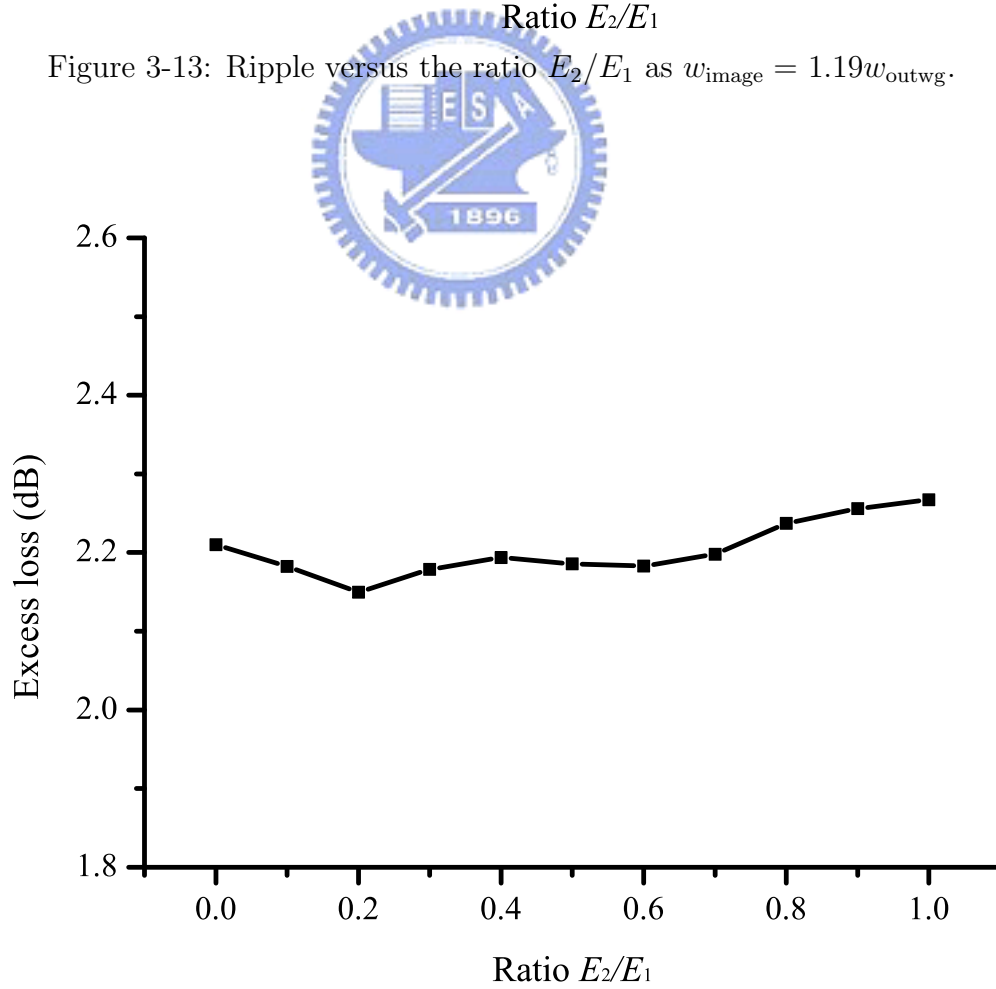


Figure 3-14: Excess loss versus the ratio  $E_2/E_1$  as  $w_{\text{image}} = 1.19w_{\text{outwg}}$ .

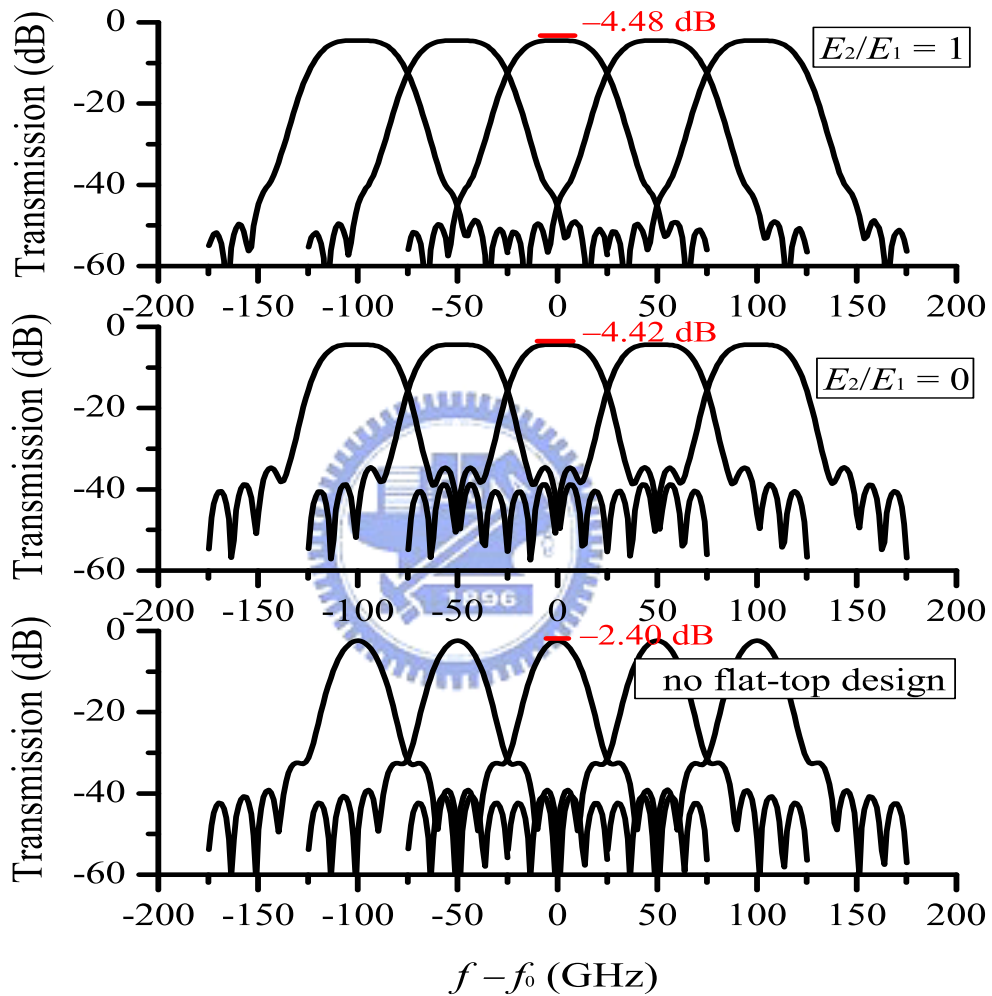


Figure 3-15: Flattened spectral responses of central five channels with and without the flat-top design for the channel spacing of 50 GHz as  $w_{\text{image}} = 1.19w_{\text{outwg}}$ .



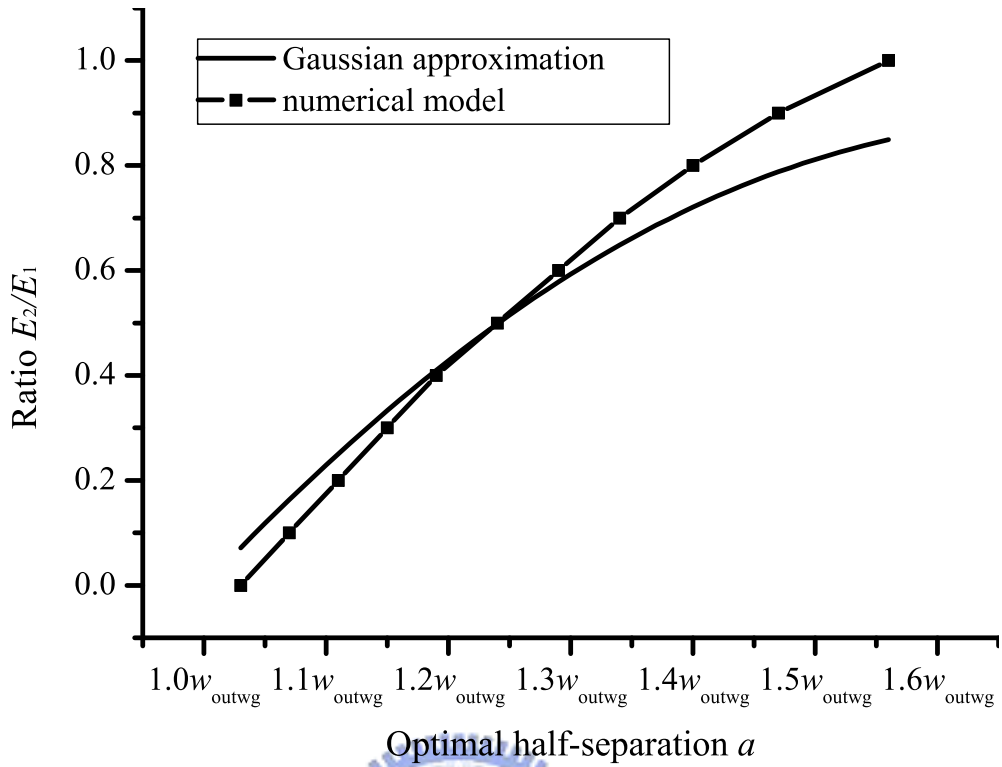


Figure 3-16:  $E_2/E_1$  versus the optimal half-separation  $a$  as  $w_{\text{image}} = w_{\text{outwg}}$ .

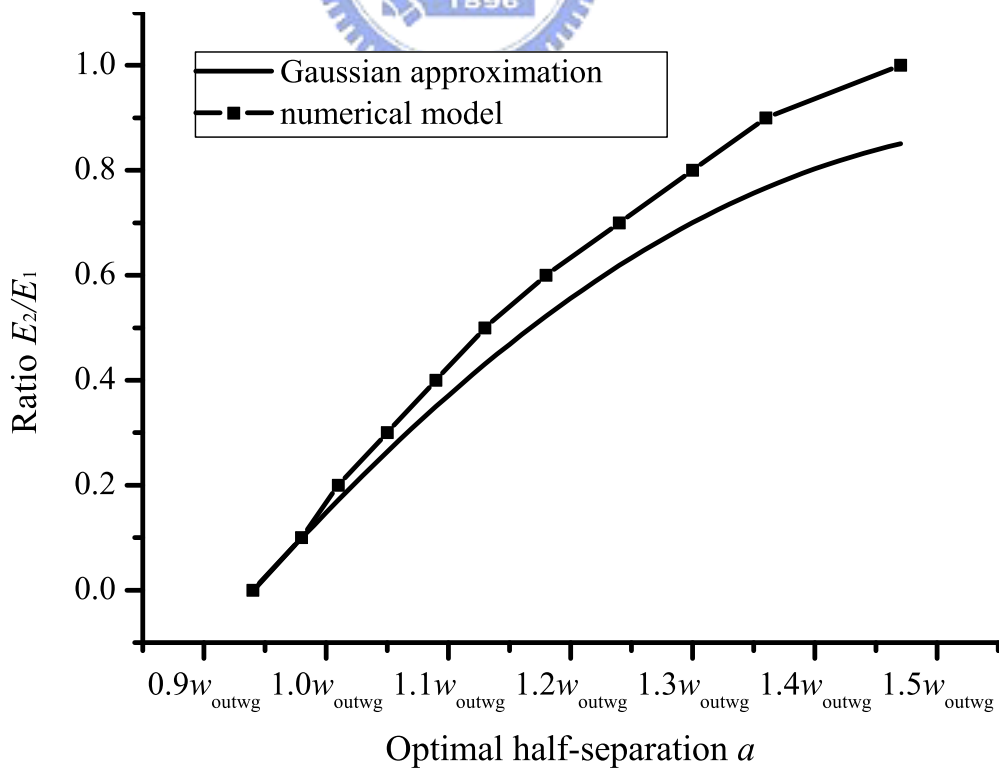


Figure 3-17:  $E_2/E_1$  versus the optimal half-separation  $a$  as  $w_{\text{image}} = 0.88w_{\text{outwg}}$ .

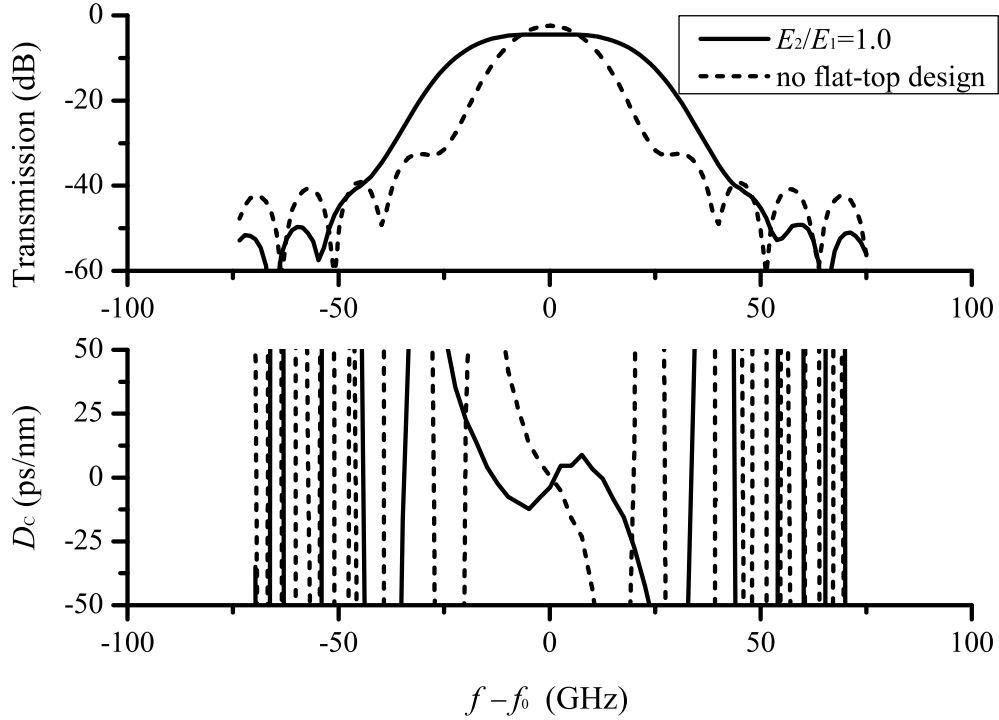


Figure 3-18: Spectral responses and the chromatic dispersion characteristics with and without the flat-top design as  $w_{\text{image}} = 1.19w_{\text{outwg}}$ .

The optimal half-separation  $a$  is obtained with a minimum ripple, and the ripple is below 0.04 dB which is shown in Fig. 3-13. The excess loss, the coupling loss from the slab waveguide to the output channel waveguide, versus the ratio  $E_2/E_1$  is shown in Fig. 3-14. Fig. 3-15 shows the spectral responses of central five channels with and without the flat-top designs for the undesired-order loss of 2.21 dB. It is shown that the flattened spectral responses can be obtained but the insertion loss will be sacrificed. The above simulation results show that the passband width for the flat-top design can be changed by changing the ratio  $E_2/E_1$ , which then determines the optimal half-separation  $a$  as shown in Fig. 3-9. More numerical examples in Figs. 3-16 and 3-17 show that the value of the intersection point of the two cases decreases as the spot size of the subimage decreases and the intersection point falls on a point with a ratio  $E_2/E_1$  of 0.5 and an optimal half-separation  $a$  of  $1.24w_{\text{outwg}}$  as  $w_{\text{image}} = w_{\text{outwg}}$ . At the intersection point, the optimal half-separation  $a$  obtained from Eq. (3.5) has the same value with that obtained from the computer simulation by using our numerical model. When  $a$  changes as  $w_{\text{image}}$  changes for the assigned values of  $E_2/E_1$  and  $w_{\text{outwg}}$  in Eq. (3.5), the intersection points of the two curves in Figs. 3-16 and 3-17 also change as  $w_{\text{image}}$  changes due to the different changes of  $E_{\text{image}}$  for the two cases.

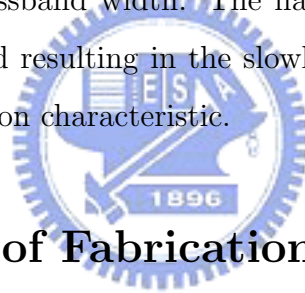
The chromatic dispersion characteristic  $D_C$  is expressed as [7]

$$D_C(\lambda) = \frac{d\tau_d}{d\lambda}, \quad (3.12)$$

where  $\tau_d$  is the group delay given by [7]

$$\tau_d \approx \frac{\lambda_0^2}{2\pi c} \frac{d\Phi(\lambda)}{d\lambda}, \quad (3.13)$$

and where  $c$  is the velocity of the light in vacuum and  $\Phi(\lambda)$  is the phase response obtained from the integral  $\int E_{\text{image}}(f, x'') \cdot E_{\text{outwg}}^*(f, x'') dx''$ . The spectral responses and chromatic dispersion characteristics for the central channel are shown in Fig. 3-18 for the cases with and without the flat-top designs. It shows that the flat-top design has the better chromatic dispersion characteristic than that without the flat-top design. The chromatic dispersion characteristic for the case of the flat-top design ranges from  $-12.35$  to  $8.91$  ps/nm within the  $-1$ -dB passband width. The flat-top design has the flatter spectral response within the passband resulting in the slowly-changing phase response so it has the better chromatic dispersion characteristic.



## 3.2 The Impact of Fabrication Errors

A design example of a flat-top demultiplexer based on a planar waveguide concave grating is used to quantitatively estimate the impact of fabrication errors on the crosstalk and insertion loss of a flat-top demultiplexer based on a planar waveguide concave grating. Fabrication errors, which come from nonidealities during the fabrication process, result in random phase and amplitude errors in the analysis using the diffraction theory [10, 36–39]. The phase errors mainly come from the deviations of the positions for the vertices of the grating facets due to discrete multiples of an address unit defined by the electron beam mask generation system [39]. The amplitude errors mainly come from the roundings of the grating corners [39] and the grating side-wall angle offset from the vertical [10].

In our analysis, these parameters caused by fabrication errors are all taken into consideration. A flat-top design of a planar waveguide concave grating based on the recursive definition of facet positions, which was first proposed by McGreer in 1996 [32], is achieved when the three-focal-point method is used [7]. Using the Kirchoff-Huygens' diffraction

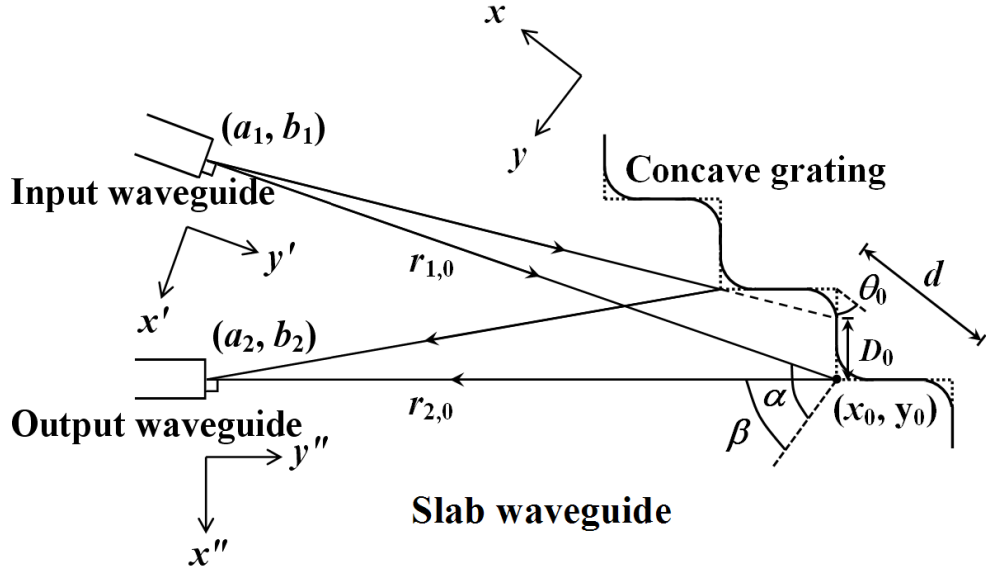


Figure 3-19: Schematic figure of the light propagating in the slab waveguide and being diffracted by the concave grating.

integral formula, the spectral response of one channel at the design wavelength  $\lambda_0$  of 1550.12 nm can be obtained. According to the corresponding phase and amplitude errors, the spectral characteristics of the demultiplexer are analyzed.

A planar waveguide concave grating as a flat-top demultiplexer based on the recursive definition of facet positions [32] shown in Fig. 3-19 is investigated, and this recursive definition design can have free-aberration characteristics. The device design is based on a silica-on-silicon waveguide structure, which is composed of a lower 10- $\mu\text{m}$ -thick  $\text{SiO}_2$  cladding layer, a 6- $\mu\text{m}$ -thick  $\text{SiON}$  core layer, and an upper 6- $\mu\text{m}$ -thick  $\text{SiO}_2$  cladding layer with the refractive indices of 1.450, 1.456, and 1.450 at the design wavelength of 1550.12 nm, respectively. By using the transfer-matrix method, the effective indices of the TE and TM modes are obtained as 1.45393 and 1.45392 with the negligible propagation losses due to the leakages to the silicon substrate as mentioned in Section 3.1.

The grating formed by etching a trench to the lower cladding layer is coated with aluminum at the back wall. Without considering the scattering loss at the grating facet, the reflection coefficient is assumed to be unity. The input and output waveguides are formed by a  $\text{SiON}$  core channel with a  $6 \times 6 \mu\text{m}^2$  cross-sectional area surrounded by the  $\text{SiO}_2$  cladding layer. The effective half widths,  $w_{\text{inwg}}$  and  $w_{\text{outwg}}$ , of the fundamental mode for the input and output waveguides along the  $x'$ -axis and  $x''$ -axis, as shown in Fig. 3-19, are 4.91  $\mu\text{m}$  obtained with BeamPROP software from R-Soft. The Gaussian field [35] launched from the input waveguide is diffracted by the grating, focused at the focal

curve, and then guided into different output waveguides according to the corresponding wavelengths.  $\alpha = 60^\circ$  is the incident angle at the grating pole,  $\beta = 57.12^\circ$  is the  $m$ th-order diffraction angle of the design wavelength at the grating pole,  $m = 16$  is the diffraction order,  $d = 10 \mu\text{m}$  is the grating period along the grating chord, and  $\lambda_0 = 1550.12 \text{ nm}$  is the design wavelength. The half angle  $\sigma (= \lambda_0/\pi n_{\text{eff}} w_{\text{inwg}})$  for the Gaussian beam divergence at  $1/e$  amplitude is obtained as  $3.96^\circ$  for the TE mode. The distances from the end of the input waveguide and the end of the output waveguide of the design wavelength to the grating pole are  $r_{1,0} = 35000$  and  $r_{2,0}(f_0) = 35000 \mu\text{m}$ , respectively. The number of grating periods is  $N = 968$  and the effective radius of the grating curvature  $R = 67011 \mu\text{m}$ .

To obtain a flattened spectral response, the grating is composed of three interleaved subgratings [7] and each forms a subimage with a different focal point lying on the cross-sectional line of the ending facet for the output waveguide, as shown in Fig. 3-20, where  $E_1$ ,  $E_2$ , and  $E_3$  denote the peak amplitudes of three subimages and  $2a$  denotes the separation between the two outmost subimages (subimage 1 and subimage 3). To obtain a symmetric spectral response,  $E_1$  and  $E_3$  are chosen to be identical and the ratio of the peak amplitudes for the subimages is approximately equal to the ratio of the facet numbers for the corresponding subgratings. Because three subgratings are interleaved, the spot size  $w_{\text{image}}$  of each subimage along the  $x''$ -axis is identical and is obtained as  $5.85 \mu\text{m}$ . Simulation results in Section 3.1 show that when the ratio  $E_2/E_1$  is chosen as 1, the optimal half-separation  $a$  between the two outmost subimages is obtained as  $1.74w_{\text{outwg}}$  with a minimum ripple. The ripple is defined as the maximum difference among three extremum points within the  $-3\text{-dB}$  passband of one channel. The  $-1\text{-dB}$  passband width is  $27.19 \text{ GHz}$  with a crosstalk of  $-36.34 \text{ dB}$ . The insertion loss in our case is  $4.48 \text{ dB}$ , where  $2.27 \text{ dB}$  comes from the excess loss, obtained from the overlap integral of the imaging field with the output waveguide mode field, and  $2.21 \text{ dB}$  comes from the undesired-order loss, resulting from the diffraction of light into undesired adjacent orders.

The phase errors, which are mainly caused by the deviations of the positions for the vertices of the grating facets, lead to the deterioration in the spectral response. The standard deviation  $\sigma_p$  of the position errors, i.e., the resolution of the photomask, is defined as

$$\sigma_p = \sqrt{\sigma_{\text{px}}^2 + \sigma_{\text{py}}^2} = \sqrt{\frac{1}{(N-1)} \sum_i (\Delta x_i^2 + \Delta y_i^2)}, \quad (3.14)$$

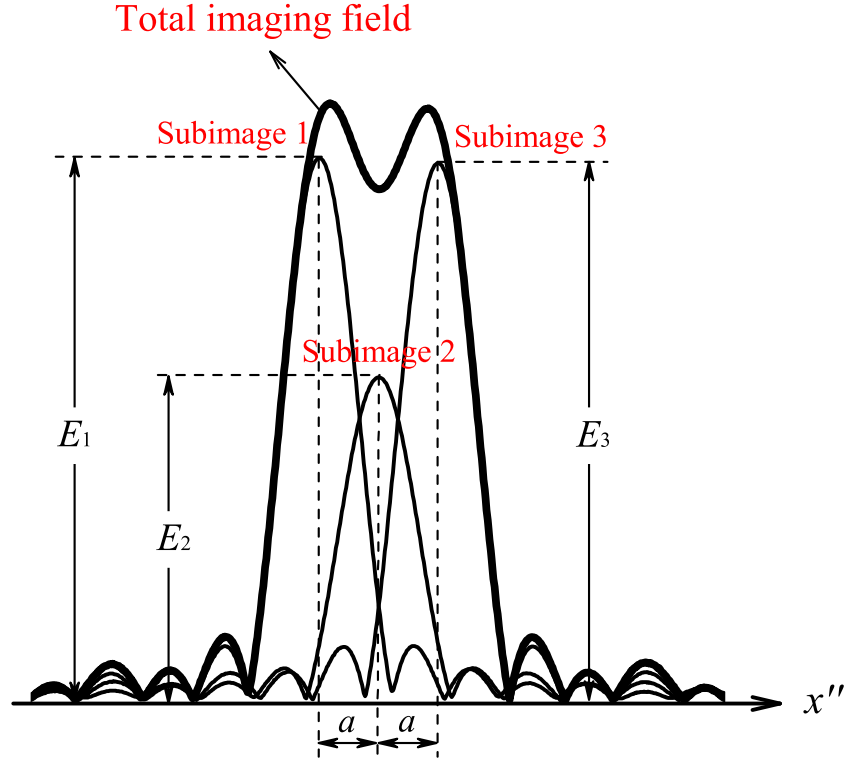


Figure 3-20: Field distribution of three subimages at the ending facet of the output waveguide.

where  $\Delta x_i$  and  $\Delta y_i$  are the deviations of the positions for the vertices of the  $i$ th grating facet along the  $x$ -axis and  $y$ -axis, respectively.  $\Delta x_i$  and  $\Delta y_i$  are randomly generated by a computer and they are normalized with an assigned value  $\sigma_p$ . The crosstalks of the central channel versus various standard deviations  $\sigma_p$  for 50 samples are shown in Fig. 3-21 when the channel spacing  $\Delta\lambda_{\text{channel}}$  is 0.4 nm (50 GHz). It shows that when  $\sigma_p$  increases from 0 to 100 nm, the mean value of the crosstalks increases from  $-36.34$  to  $-29.78$  dB. It also shows that when the crosstalk criterion of  $-30$  dB in our case is given, a photomask resolution lower than 40 nm is required. The phase errors are the main sources of the crosstalk. The corresponding  $-1$ -dB passband widths of the central channel for 50 samples are shown in Fig. 3-22. It shows that the fluctuation of the  $-1$ -dB passband width increases as the standard deviation  $\sigma_p$  of the position errors increases.

The corner roundings of the grating facets reduce the effective facet widths  $D_i$ , as shown in Fig. 3-19, and then increase the insertion loss when the light reflected from the rounding facets is lost. In our design, the facet widths  $D_i$  range from 5.00 to 5.12  $\mu\text{m}$ . It is assumed that all grating facets have the same width reduction  $\Delta D$  due to the corner roundings to evaluate the additional loss caused by the corner roundings and Fig. 3-23

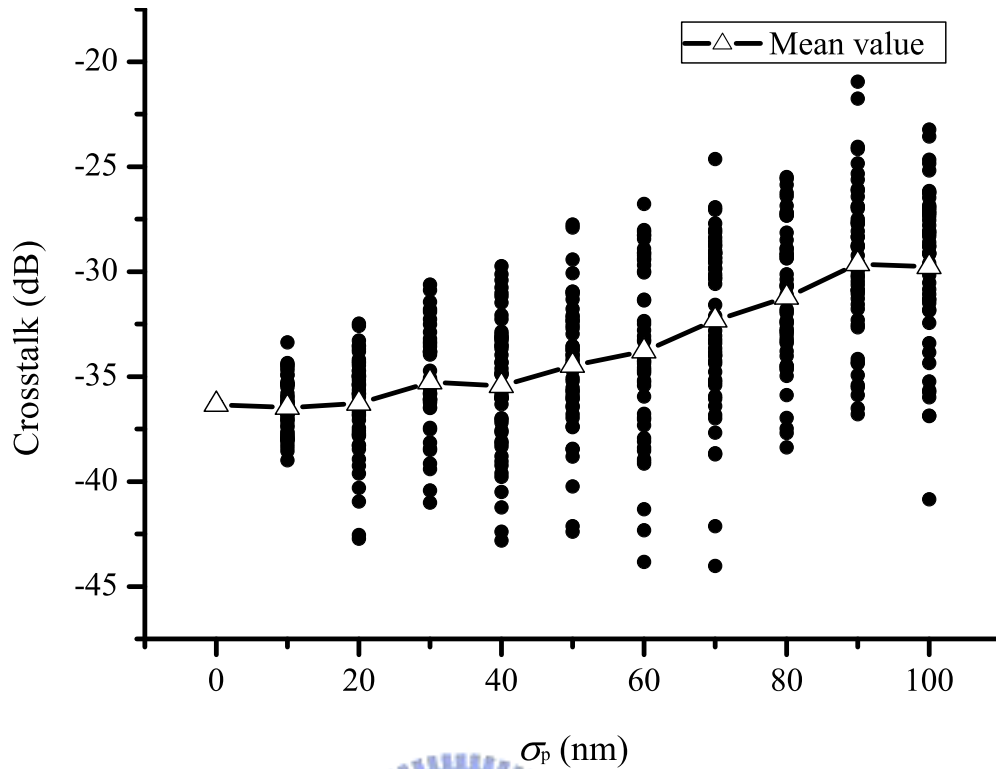


Figure 3-21: Crosstalks of the central channel versus various standard deviations  $\sigma_p$  for 50 samples when the channel spacing  $\Delta\lambda_{\text{channel}}$  is 0.4 nm (50 GHz).

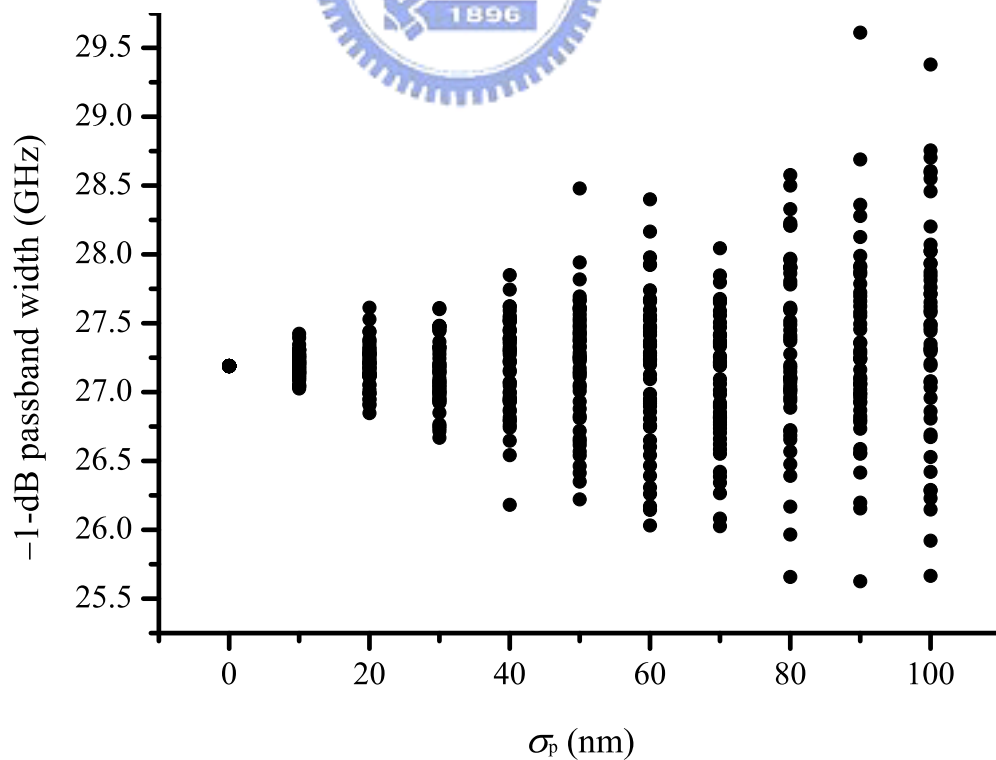


Figure 3-22: -1-dB passband widths of the central channel versus various standard deviations  $\sigma_p$  for 50 samples when the channel spacing  $\Delta\lambda_{\text{channel}}$  is 0.4 nm (50 GHz).

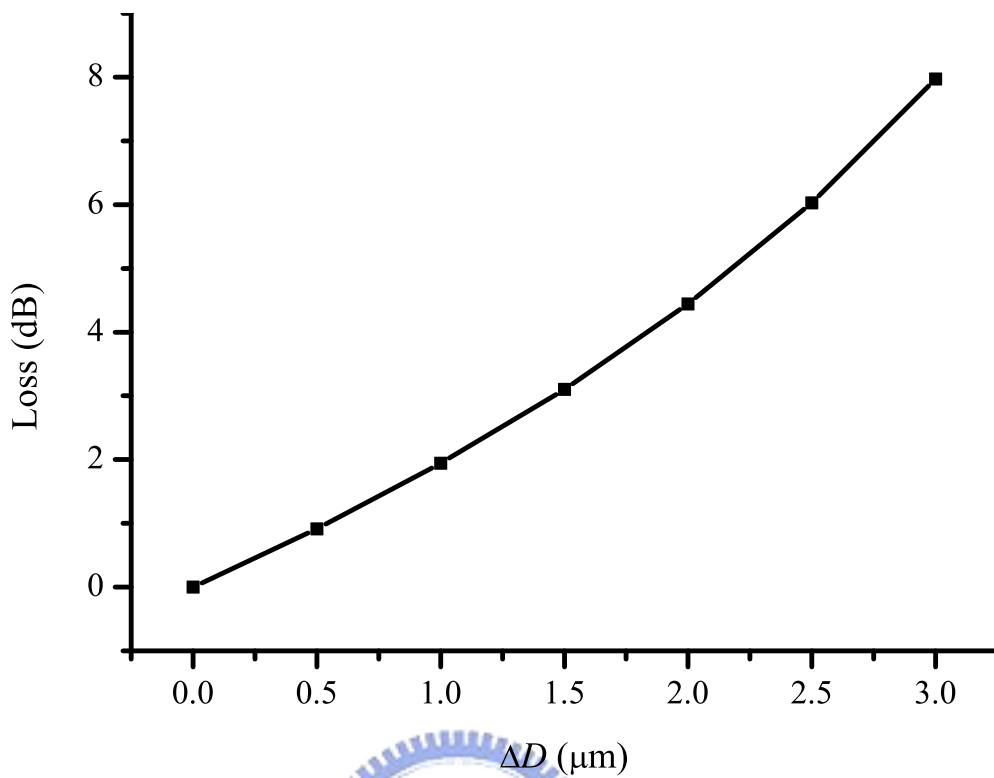


Figure 3-23: Loss versus the width reduction  $\Delta D$ .

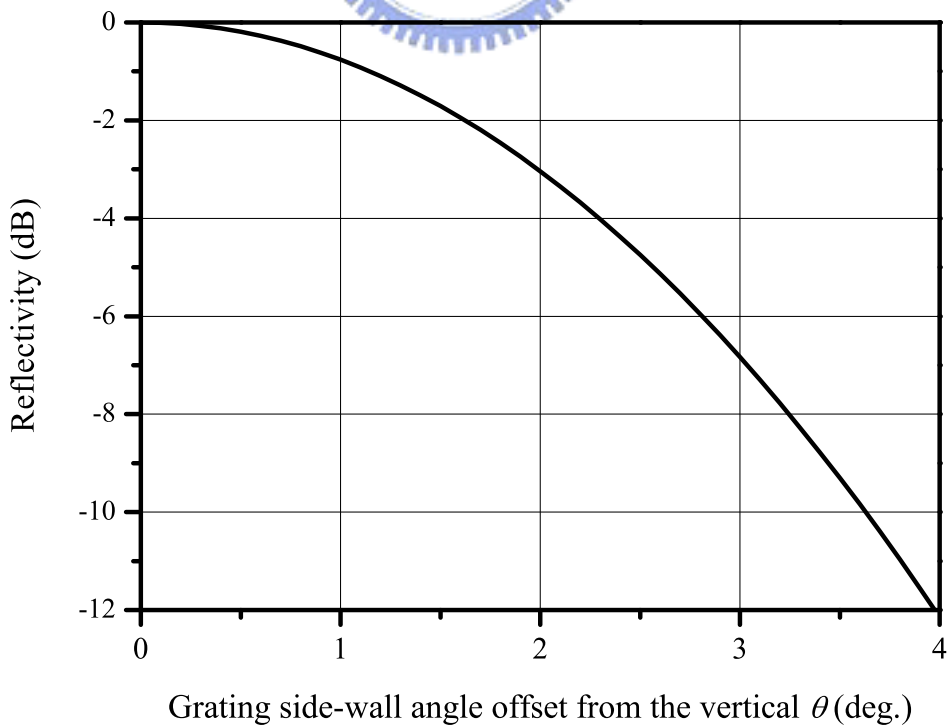


Figure 3-24: Reflectance  $R$  versus the side-wall angle offset  $\theta$  from the vertical.



shows the results. The additional loss increases as the width reduction  $\Delta D$  increases as expected, and this additional loss is 0.92 dB when the width reduction  $\Delta D$  is 0.5  $\mu\text{m}$ . The other challenge of fabricating the etched diffraction grating (EDG) is to achieve a nearly vertical grating side wall. The reflectance  $R$  affected by the side-wall angle offset from the vertical with a small tilt angle  $\theta$  can be expressed as [40]

$$R = 10 \log e^{-(2\theta/\theta_d)^2}, \quad (3.15)$$

$$\theta_d = \frac{\lambda_0}{\pi n_{\text{eff}} \omega_0}, \quad (3.16)$$

where  $\omega_0 = 4.07 \mu\text{m}$  is the effective half width of the slab waveguide mode along the  $z$ -axis as shown in Fig. 3-6. The simulation results, as shown in Fig. 3-24, predict that a side-wall angle offset of  $1^\circ$  from the vertical will lead to an additional loss of more than 0.76 dB. When the width reduction and grating side-wall angle offset are 0.5  $\mu\text{m}$  and  $\pm 1^\circ$ , the additional losses are 0.92 and 0.76 dB, respectively, which contribute to an acceptable additional loss below 2.00 dB.

### 3.3 Five-Focal-Point Method

A five-focal-point method is introduced for the design of a flat-top planar waveguide demultiplexer and is optimized by a commonly used optimization method, which is called the genetic algorithm (GA). The genetic algorithm based on Darwin's principle of "survival of the fittest" [9, 27] is used to optimize the parameters used in a five-focal-point method. The design formulas for the concave grating are discussed in detail and a design example is given to analyze the spectral characteristics of the design. The parameters are encoded into the chromosome strings used for the genetic algorithm and optimized by using the multiobjective fitness function. The grating is divided into five interleaved subgratings with the different focal points lying on the cross-sectional line of the ending facet for the output waveguide. Each subimage has approximately the same spot size since the subgratings are interleaved, and overlaps with each other. There are four parameters needed for the optimization in our design. The optimized parameters are obtained by choosing the chromosome string with the maximal fitness in the population of the last generation. The larger  $-1$ -dB passband width and the lower ripple are achieved. Moreover, the spectral responses and the chromatic dispersion characteristics

of the multiplexer are also analyzed.

### 3.3.1 Design Formulas and Design Example

The structures of the channel waveguide and slab waveguide are shown in Figs. 3-3 and 3-4. By using the transfer-matrix method [29], the effective index  $n_{\text{eff}}$  in the slab waveguide can be solved. The diffraction formula of the plane grating is given as [30]:

$$n_{\text{eff}}d(\sin \alpha + \sin \beta) = m\lambda, \quad (3.17)$$

where  $d$  is the grating period along the grating chord,  $\alpha$  is the incident angle for the input waveguide with respect to the  $y$ -axis at the grating pole,  $\beta$  is the diffraction angle for the output waveguide with respect to the  $y$ -axis at the grating pole,  $m$  is the diffraction order, and  $\lambda$  is the operating wavelength. In the design,  $d$ ,  $\alpha$ , and  $m$  are chosen. For a wavelength  $\lambda$  with a corresponding frequency of  $f$ ,  $\beta(f)$  can be solved from Eq. (3.17). For a design wavelength  $\lambda_0$  with a corresponding frequency of  $f_0$ ,  $\beta(f_0)$  can be obtained. The distance  $r_{1,0}$  from the end of the input waveguide to the grating pole and the distance  $r_{2,0}(f_0)$  from the grating pole to the end of the design output waveguide corresponding to a design frequency of  $f_0$  are chosen as shown in Fig. 3-2. If the grating pole is located at the origin of the coordinates, the positions of the input waveguide and design output waveguide can be obtained as  $(a_1, b_1) = (r_{1,0} \cdot \sin \alpha, r_{1,0} \cdot \cos \alpha)$  and  $(a_2, b_2) = (r_{2,0}(f_0) \cdot \sin \beta(f_0), r_{2,0}(f_0) \cdot \cos \beta(f_0))$ , respectively. The design of a planar waveguide concave grating here is based on the recursive definition of facet positions due to the superior diffraction characteristics [32,34]. After determining the  $x$ -axis coordinate position of the vertex of the  $i$ th groove as  $x_i = i \cdot d$ , the free-aberration  $y$ -axis coordinate position  $y_i$  of the vertex of the  $i$ th groove can be obtained from the solution of the root for Eq. (3.6).

The focal equation for the concave grating can be obtained from Eq. (3.8). With  $\alpha$ ,  $\beta(f_0)$ ,  $r_{1,0}$ , and  $r_{2,0}(f_0)$  at a design frequency of  $f_0$  being determined,  $R$  can be obtained from Eq. (3.8). For the specific channel at a frequency of  $f$ ,  $\beta(f)$  can be obtained from Eq. (3.17) and then  $r_{2,0}(f)$  can be obtained from Eq. (3.8). The numerical model of the scalar diffraction theory for the concave grating in the planar waveguide can be obtained from Eq. (3.9).

For a design example, the waveguide structure is composed of a lower 10- $\mu\text{m}$ -thick

SiO<sub>2</sub> cladding layer, a 6- $\mu\text{m}$ -thick SiON core layer, and an upper 6- $\mu\text{m}$ -thick SiO<sub>2</sub> cladding layer with the refractive indices of 1.450, 1.456, and 1.450, respectively, at an operating wavelength of 1550.12 nm. The single-mode channel waveguide, such as the input waveguide or the output waveguide, has the SiON core layer with a cross-sectional area of  $6 \times 6 \mu\text{m}^2$  and is surrounded by the SiO<sub>2</sub> cladding layer as shown in Fig. 3-3. The grating has been achieved by etching a trench to the lower cladding layer and then coated with metal at the back wall to enhance the reflectivity [10].

By using the transfer-matrix method [29], there exist single TE and TM modes in the slab waveguide region and the effective indices for the fundamental TE and TM modes are 1.45393 and 1.45392, respectively. According to ITU grids [1], there are 81 channels in the C-band with a channel spacing  $\Delta\lambda_{\text{channel}}$  of 0.4 nm (50 GHz) from 1528.77 to 1560.61 nm. we choose a design wavelength  $\lambda_0$  of 1550.12 nm, a grating period  $d$  of 10  $\mu\text{m}$ , and incident angle  $\alpha$  for the input waveguide with the respect to the  $y$ -axis at the grating pole of  $60.00^\circ$ , and a diffraction order  $m$  of 16. We take the TE mode for example and the effective index of the fundamental TE mode in the slab waveguide region is 1.45393. The diffraction angle  $\beta(f_0)$  for the design output waveguide with respect to the  $y$ -axis at the grating pole can be obtained as  $57.12^\circ$  from Eq. (3.17).

The distance from the end of the input waveguide to the grating pole is  $r_{1,0} = 35000 \mu\text{m}$  and the distance from the grating pole to the end of the design output waveguide is  $r_{2,0}(f_0) = 35000 \mu\text{m}$  as shown in Fig. 3-2. Then the positions of the input waveguide and output waveguide can be obtained. The effective half widths,  $w_{\text{inwg}}$  and  $w_{\text{outwg}}$  of the input and output waveguides for the fundamental modes are 4.91  $\mu\text{m}$  obtained with BeamPROP software from R-Soft and the half angle  $\sigma$  of the beam divergence is  $3.96^\circ$ . The number of grating periods is calculated as  $N = 968$ . After the  $x$ -axis coordinate position of the vertex of each groove is determined, the free-aberration  $y$ -axis coordinate position of the vertex of each groove can be obtained from Eq. (3.6). The spot size of each subimage is  $w_{\text{image}} = 5.85 \mu\text{m}$  obtained from Eq. (3.9). The effective radius of the grating curvature is  $R = 67011 \mu\text{m}$  obtained from Eq. (3.8). The spatial dispersion coefficient is  $D_s = 0.569 \mu\text{m}/\text{GHz}$  in our case. The spectral response of each channel can be obtained from Eq. (3.10). Assuming the little side-wall irregularity and almost vertical side-wall angle of the grating facet, no scattering loss is considered.

### 3.3.2 Numerical Analysis

The grating is composed of five interleaved subgratings with the different focal points and each focal point lies on the cross-sectional line of the ending facet for the output waveguide. Each subimage formed by the corresponding subgrating overlaps with each other as shown in Fig. 3-25, where  $E_1, E_2, E_3, E_4,$  and  $E_5$  denote the peak amplitudes of five subimages,  $a$  denotes the separation between subimage 1 (subimage 5) and subimage 3, and  $b$  denotes the separation between subimage 2 (subimage 4) and subimage 3. To obtain a symmetric spectral response,  $E_1$  and  $E_5$  ( $E_2$  and  $E_4$ ) are designed to be identical. The spot sizes of all subimages are approximately the same when the subgratings are interleaved well [7].

If the subgratings are interleaved, the ratio of the peak amplitudes of the subimages is approximately equal to the ratio of the facet numbers of the corresponding subgratings [7]. We can adjust the ratio of the facet numbers of subimage 3 and subimage 1 (subimage 2 and subimage 1) to adjust the ratio  $E_3/E_1$  ( $E_2/E_1$ ). If the grating pole is located at the origin of the coordinates, after determining the arrayed sequence of the facets of the subgratings the  $x$ -axis coordinate position  $x_i$  of the vertex for the  $i$ th groove can be obtained from Eq. (3.11). The order  $m$  for each subgrating is identical while the grating period  $d_k$  and the central wavelength  $\lambda_k$  for each subgrating are different as the multigrating method [3]. The  $y$ -axis coordinate position  $y_i$  of the vertex of the  $i$ th groove can then be obtained from the solution of the root for Eq. (3.6).

The genetic algorithm is used to optimize the parameters in the five-focal-point method for a flat-top planar waveguide demultiplexer, and the parameters will be defined below. The genetic algorithm based on Darwin's principle of "survival of the fittest" was invented by Holland in the 1960s [27]. By using operators of selection, crossover, and mutation, one population of "chromosomes", strings of ones and zeros, can generate a new population. The fitter the chromosome, the more times it is likely to be selected to reproduce.

In our case, the parameters  $(E_3/E_1, E_2/E_1, a/w_{\text{outwg}}, b/w_{\text{outwg}})$  need to be optimized and are encoded into the chromosome strings of the genetic algorithm for the fittest

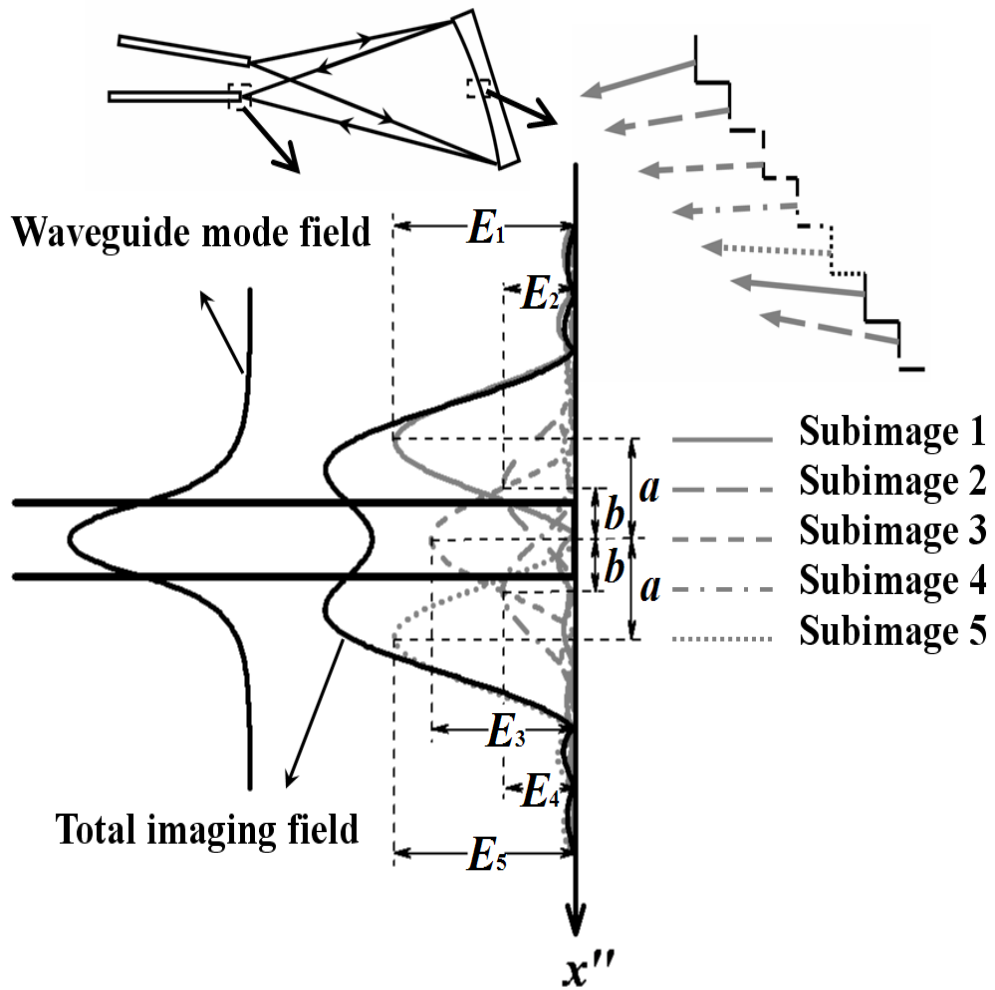


Figure 3-25: Field distribution of the five subimages at the ending facet of the output waveguide.

solution. The problem involves two objectives,  $F_1$  and  $F_2$ ,

$$F_1 = \frac{W_{-1\text{dB}}}{W_{-3\text{dB}}}, \quad (3.18)$$

$$F_2 = \frac{1}{R_{\text{ripple}}}, \quad (3.19)$$

where  $W_{-1\text{dB}}$  and  $W_{-3\text{dB}}$  denote the  $-1\text{-dB}$  and  $-3\text{-dB}$  passband widths of the central channel, respectively, and  $R_{\text{ripple}}$  denotes the ripple, which is defined as the maximum difference among extremum points within  $-3\text{-dB}$  passband of the central channel. For the fittest solution, a higher value of  $W_{-1\text{dB}}/W_{-3\text{dB}}$  is obtained for a lower adjacent channel crosstalk and a higher value of  $1/R_{\text{ripple}}$  is obtained for the lower ripple. So the multiobjective fitness function is required:

$$F_{\text{obj.}} = \max(F_1, F_2). \quad (3.20)$$

The multiobjective problem can be solved by combining all objectives into a single objective:

$$F_{\text{obj.}} = w_1 F_1 + w_2 F_2, \quad (3.21)$$

where  $w_1$  and  $w_2$  denote the weighting factors of the objectives and are chosen as  $1/0.9$  and  $1/1000$ , respectively, in our case. The problem also involves some constraints. The values of  $E_3/E_1$  and  $E_2/E_1$  range between 0.0 and 1.0. The value of  $a/w_{\text{outwg}}$  is higher than the value of  $b/w_{\text{outwg}}$ .

The number  $n$  of the population for each generation is 100 and the total number of generations is 100. The crossover probability  $p_c$  is chosen as 0.8 with a mutation probability  $p_m$  of 0.1. At first,  $n$  chromosomes are randomly generated and the fitness  $F_{\text{obj.}}$  of each chromosome is calculated. By using a method of “roulette-wheel sampling”, the operator of selection selects two chromosomes in proportion to the fitness for two parents. With the crossover probability  $p_c$ , the operator of crossover randomly chooses a locus and exchanges the subsequences before and after that locus between two chromosomes (parents) to create two offspring [27]. And each bit (gene) in the chromosome will be mutated according to the mutation probability  $p_m$ , i.e., 0 to 1 and 1 to 0. The operator of mutation provides an efficient way to escape from a local maximum to a global maximum if the number of generations is big enough in a run. Until  $n$  chromosomes (offspring)

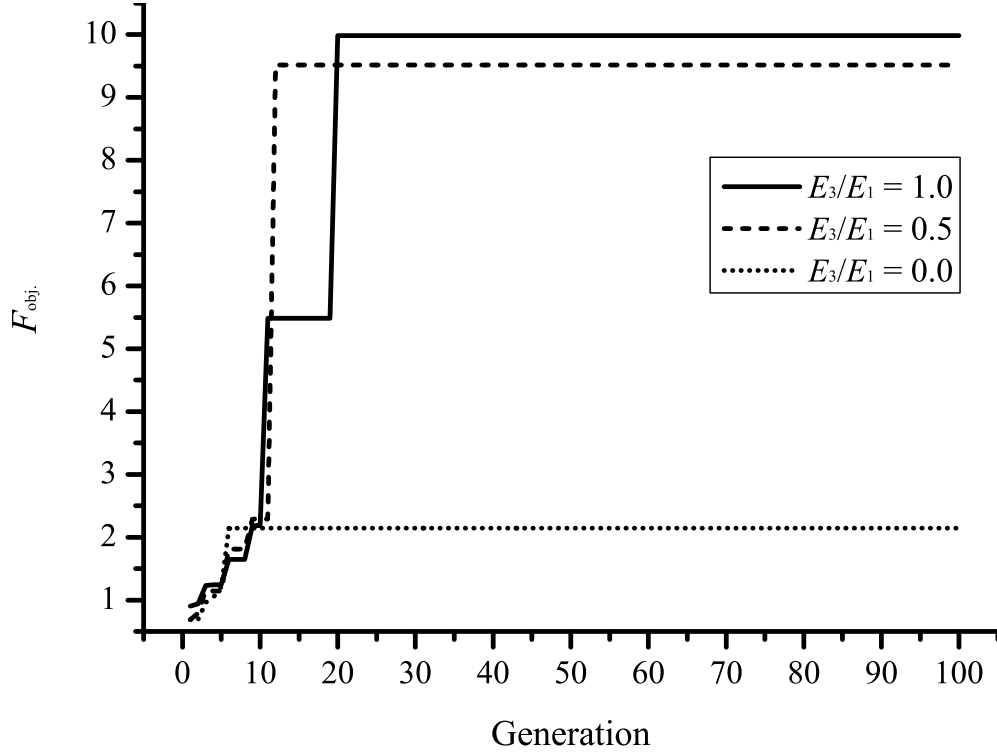


Figure 3-26: Maximal fitness in the individual generation.

are created, it is called one generation (iteration). Eventually, all the parameters will converge to the fittest results after a number of generations. All computer program codes for the simulation are written in Fortran 90.

It takes about 78 hours to finish a run with a CPU processor of Intel Core 2 Duo E6300 (1.87 GHz) and the 2-Gb DDR ram. Fig. 3-26 shows the maximal fitness in the population as the generation increases. It also shows that when the ratio  $E_3/E_1$  is assigned with the different values, the genetic algorithm will converge to the different results. A number of trials with the different initial populations have been carried out and give the similar results. When the ratio  $E_3/E_1$  increases from 0 to 1, the genetic algorithm will converge to the result with higher fitness but it needs more generations for a steady state. The optimal parameters ( $E_3/E_1, E_2/E_1, a/w_{outwg}, b/w_{outwg}$ ) for the three cases are (1.0, 0.1, 2.11, 0.37), (0.5, 0.8, 2.11, 0.82), and (0.0, 0.9, 2.05, 0.61) with the values of fitness of 9.99, 9.52, and 2.14, respectively. The values of  $W_{-1dB}/W_{-3dB}$  for the three cases are all 0.72 and the values of  $1/R_{ripple}$  are 9191, 8716, and 1342, respectively. The  $-1$ -dB passband widths for the three cases are 30.53, 28.10, and 27.92 GHz, respectively, with the ripples of  $1.09 \times 10^{-4}$ ,  $1.15 \times 10^{-4}$ , and  $7.45 \times 10^{-4}$  dB, respectively. With the temperature coefficient of the refractive index for the silica being 1



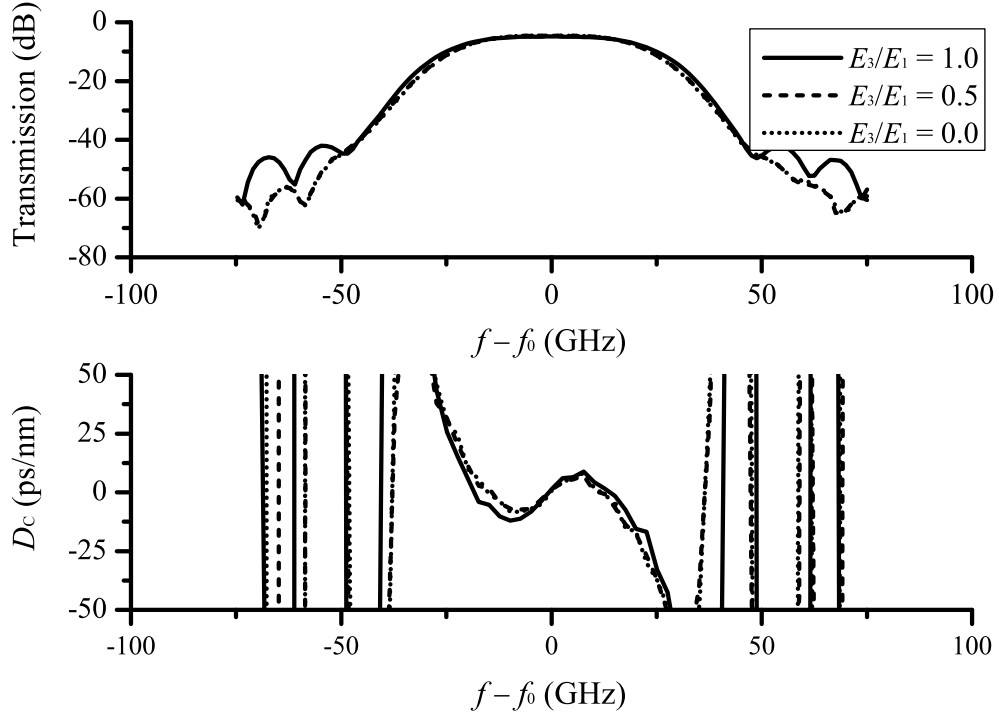


Figure 3-27: Spectral responses and the chromatic dispersion characteristics for the three cases.

$\times 10^{-5}$  ( $1/^\circ\text{C}$ ) [17], the temperature tolerances for the intensity fluctuation of the central channel below  $-1$  dB can be obtained as  $\pm 13.4$ ,  $\pm 13.5$ , and  $\pm 13.7$   $^\circ\text{C}$ , respectively. It shows that the case of  $E_3/E_1 = 1.0$  gives a larger  $-1$ -dB passband width and a lower ripple [7].

With the Gaussian approximation, the three-focal-point method [7] is illustrated and verified with a design example in Section 3.1. With the numerical model of the scalar diffraction theory [35], the five-focal-point method is illustrated with the design example and optimized by using the genetic algorithm. The genetic algorithm is a search technique used in the computer science to find the optimal solution even in a multiobjective problem. The  $-1$ -dB passband width and ripple for the three-focal-point method based on the Gaussian approximation are 62 GHz (62% of the channel spacing) and 0.013 dB [7]. Simulation results show that the five-focal-point method gives a near-equivalent ratio (61%) of the  $-1$ -dB passband width to the channel spacing and a lower ripple  $R_{\text{ripple}}$  ( $1.09 \times 10^{-4}$  GHz) compared with the three-focal-point method based on the Gaussian approximation [7].

The chromatic dispersion characteristic  $D_C$  can be obtained from Eq. (3.12). Fig. 3-27 shows the spectral responses and the chromatic dispersion characteristics  $D_C$  of the central channel for the three cases. It shows that the case of  $E_3/E_1 = 0.0$  has the lower



crosstalk and insertion loss, while the case of  $E_3/E_1 = 0.5$  has the better chromatic dispersion characteristics. The crosstalks for the three cases are  $-35.74$ ,  $-35.78$ , and  $-36.31$  dB, respectively, with the insertion losses of  $4.87$ ,  $4.59$ , and  $4.57$  dB, respectively.

### 3.4 Summary

In summary, a modified formula for the three-focal-point method is proposed and compared with a numerical model of the scalar diffraction theory by a design example in Section 3.1. Simulation results show that the deviation between the two cases becomes serious as the ration  $E_2/E_1$  approaches unity and the optimal half-separation  $a$  can be approximately obtained using the modified formula. The changed passband width can be achieved by changing the ratio  $E_2/E_1$ . The chromatic dispersion characteristic is also considered.

In Section 3.2, the impact of fabrication errors relevant to the phase and amplitude errors on a flat-top planar waveguide demultiplexer is evaluated. Simulation results show that the phase errors caused by the deviations of the positions for the vertices of the grating facets are the main sources of the crosstalk, and the amplitude errors caused by the roundings of the grating corners and the grating side-wall angle offset from the vertical cause additional losses. When the standard deviation of the position errors increases from 0 to 100 nm, the mean value of the crosstalks for 50 samples increases from  $-36.34$  to  $-29.78$  dB. With a crosstalk criterion of  $-30$  dB in our case, a photomask resolution lower than 40 nm is required.

In Section 3.3, a five-focal-point method is introduced for the optimal design of a flat-top planar waveguide demultiplexer. The multiobjective genetic algorithm is used to optimize the parameters. A larger  $-1$ -dB passband width of 30.53 GHz and a lower ripple of  $1.09 \times 10^{-4}$  dB for the case of  $E_3/E_1 = 1.0$  with a channel spacing of 50 GHz are achieved. It shows that the five-focal-point method gives a near-equivalent ratio of the  $-1$ -dB passband width to the channel spacing and a lower ripple  $R_{\text{ripple}}$  compared with the three-focal-point method based on the Gaussian approximation.

# Chapter 4

## Planar Waveguide Concave Grating Employing Dielectric Mirrors

In this chapter, a planar waveguide concave grating with dielectric mirrors is proposed to yield a high reflectance and low polarization-dependent loss (PDL). Although metalization [24, 41–43] can also be used to increase the reflectance of the grating, a metalized grating usually yields a higher PDL. This is particularly true in a Littrow mount [24]. To solve the problem, we show that a grating with facets employing dielectric mirrors can produce a high reflectance bandwidth covering the entire C-band.

### 4.1 Transfer-Matrix Analysis

We used the transfer matrix method [44] to design a high-reflectance multi-slot stack. The fields are continuous across the interfaces of the films. For the dielectric mirror design, a series of the air slots and the high-index stacks with the quarter-wave widths yield a desired high reflectance. The fields at two outmost boundaries can be expressed in matrix form as

$$\begin{bmatrix} E_a \\ B_a \end{bmatrix} = \mathbf{M} \begin{bmatrix} E_b \\ B_b \end{bmatrix}, \quad (4.1)$$

$$\mathbf{M} = \begin{bmatrix} m_{11} & m_{12} \\ m_{21} & m_{22} \end{bmatrix} = \mathbf{M}_1 \cdot \mathbf{M}_2 \cdot \mathbf{M}_3 \cdots \mathbf{M}_n, \quad (4.2)$$

where  $E_a$  and  $B_a$  denote the E- and B-fields at the input boundary,  $E_b$  and  $B_b$  denote the E- and B-fields at the output boundary. The overall transfer matrix  $\mathbf{M}$  is the product

of all individual  $2 \times 2$  transfer matrices. The individual  $2 \times 2$  transfer matrix  $\mathbf{M}_j$  of the  $j$ th air slot or high-index stack can be expressed as [44]

$$\mathbf{M}_j = \begin{bmatrix} \cos \delta_j & (i/\gamma_j) \sin \delta_j \\ i\gamma_j \sin \delta_j & \cos \delta_j \end{bmatrix}, \quad (4.3)$$

where  $\delta_j$  denotes the phase difference due to one travel of the  $j$ th air slot or high-index stack and can be expressed as

$$\delta_j = k_0 \Delta_j = \left( \frac{2\pi}{\lambda_0} \right) n_j w_j \cos \theta_j. \quad (4.4)$$

For TE modes, the propagation constant  $\kappa_j$  can be expressed as

$$\kappa_j = n_j \sqrt{\epsilon_0 \mu_0} \cos \theta_j; \quad (4.5)$$

for TM modes, the propagation constant  $\kappa_j$  can be expressed as

$$\kappa_j = n_j \sqrt{\epsilon_0 \mu_0} / \cos \theta_j, \quad (4.6)$$

where  $k_0$  denotes the free space wave number,  $n_j$ ,  $w_j$ , and  $\theta_j$  denote the refractive index, width, and refractive angle of the  $j$ th air slot or high-index stack, respectively. The transmittance  $T$  and reflectance  $R$  can be obtained as

$$T = \left| \frac{2\kappa_a}{\kappa_a m_{11} + \kappa_a \kappa_b m_{12} + m_{21} + \kappa_b m_{22}} \right|^2, \quad (4.7)$$

$$R = \left| \frac{\kappa_a m_{11} + \kappa_a \kappa_b m_{12} - m_{21} - \kappa_b m_{22}}{\kappa_a m_{11} + \kappa_a \kappa_b m_{12} + m_{21} + \kappa_b m_{22}} \right|^2, \quad (4.8)$$

where  $\kappa_a$  and  $\kappa_b$  denote the propagation constants for the input and output mediums. The width of the  $j$ th air slot or high-index stack, needed for the odd multiple  $m_{\text{quar}}$  of quarter-wavelength, can be derived from Eq. (4.4) as

$$w_j = \frac{\Delta_j}{n_j \cos \theta_j} = \frac{m_{\text{quar}} \cdot \frac{\lambda_0}{4}}{n_j \cos \theta_j}. \quad (4.9)$$

The side view of the slab waveguide structure with the proposed planar waveguide concave grating is shown in Fig. 4-1. The etched trenches form the air slots and the

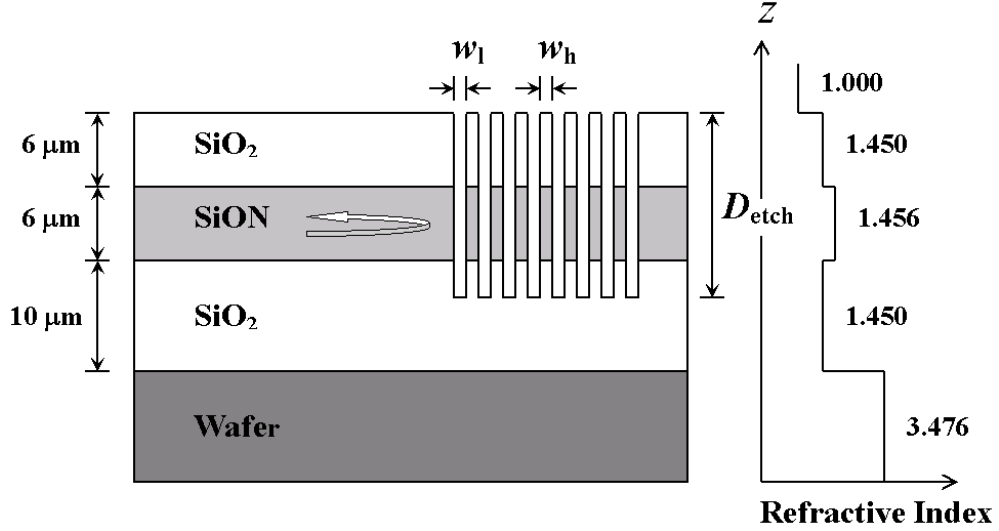


Figure 4-1: Side view of the etched trenches for a dielectric mirror.

non-etched parts form the high-index stack for the dielectric mirror design. The slab waveguide consists of a 6- $\mu\text{m}$  SiON core layer with the upper 6- $\mu\text{m}$  and the lower 10- $\mu\text{m}$  SiO<sub>2</sub> cladding layers grown on the silicon substrate. The refractive indices for the core layer, cladding layer, and the silicon substrate are 1.456, 1.450, and 3.476, respectively. The effective indices of TE<sub>0</sub> and TM<sub>0</sub> modes are 1.45393 and 1.45392 with the negligible propagation losses, which is due to the leakages to the silicon substrate. The slab waveguide supports the fundamental mode for both polarizations. Fig. 4-2 shows the top view of a planar waveguide concave grating with dielectric mirrors. The entire C-band, ranging from 1528.77 to 1560.61 nm, includes 81 wavelength channels with a channel spacing of 0.4 nm according to ITU grids [1]. The design wavelength is chosen as 1544.69 nm. In the planar waveguide concave grating design, the blaze angle of the grating facet is chosen to make the incident angle of the light to be equal to the reflective angle of the light relative to the facet normal. In a Littrow mount, this leads to the light incident upon the grating facet at a normal angle. From Eqs. (4.5) and (4.6), the reflectances  $R$  for the TE and TM modes are the same at normal incidence while they behave differently for oblique incidence.

In a Littrow mount with the air and high effective indices of 1 and 1.456, respectively, and  $m_{\text{quar}}$  of 11, the widths  $w_1$  and  $w_h$  of the air slot and high-index stack can be obtained from Eq. (4.9) to be 4.25  $\mu\text{m}$  and 2.92  $\mu\text{m}$ , respectively. Simulation results show that the bandwidth of the high-reflectance region increases with the number  $N_{\text{slot}}$  of the air slots increases as shown in Fig. 4-3. Here, the high-reflectance region is defined as the region

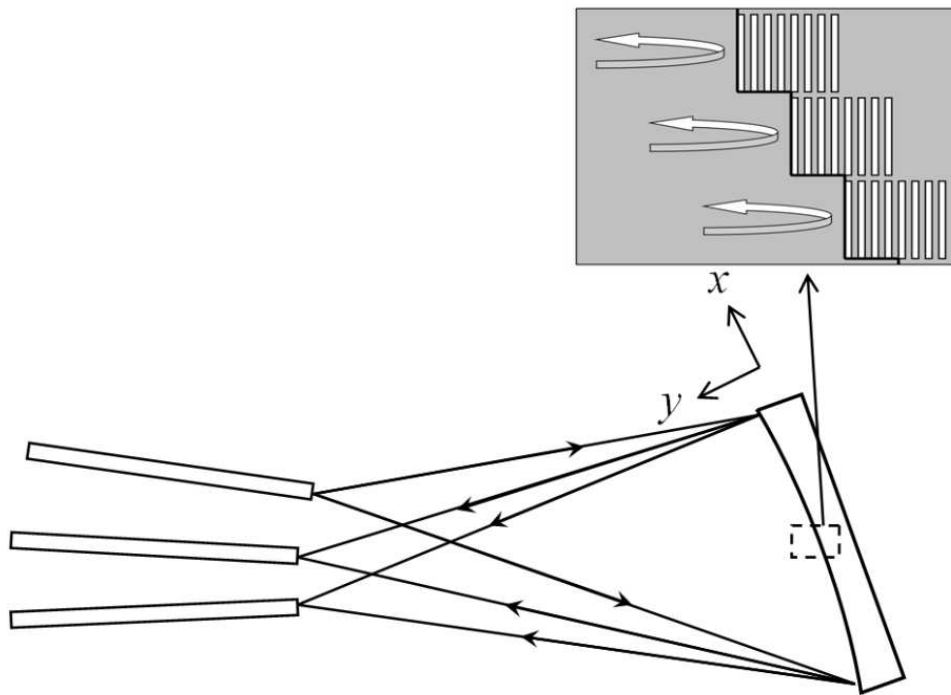


Figure 4-2: Top view of a planar waveguide concave grating with dielectric mirrors.

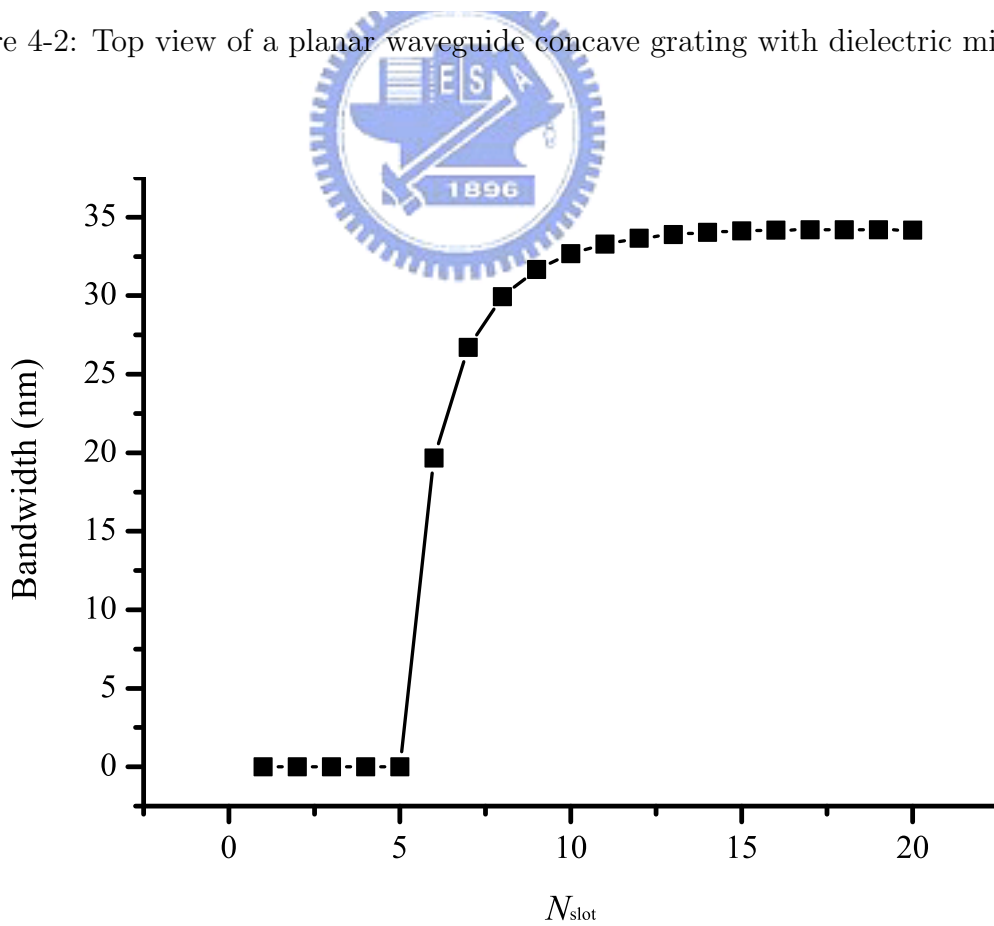


Figure 4-3: Bandwidth of the high-reflectance region versus  $N_{\text{slot}}$  in a Littrow mount with  $m_{\text{quar}}$  of 11 at a design wavelength  $\lambda_0$  of 1544.69 nm.

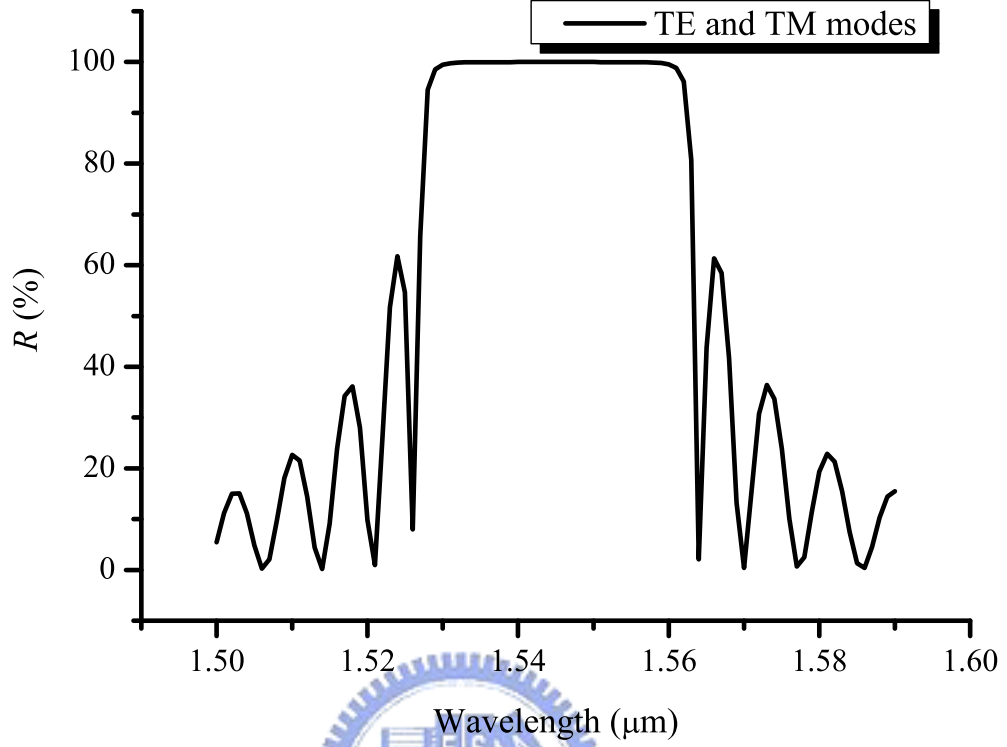


Figure 4-4: Reflectances  $R$  for the TE and TM modes versus the corresponding wavelength in a Littrow mount with  $m_{\text{quar}}$  of 11 and  $N_{\text{slot}}$  of 15 for the transfer-matrix analysis.

Table 4.1: Bandwidth results of the high-reflectance region in a Littrow mount with  $N_{\text{slot}}$  of 15 and  $\lambda_0$  of 1544.69 nm

$m_{\text{quar}}$	$w_l$ ( $\mu\text{m}$ )	$w_h$ ( $\mu\text{m}$ )	Range (nm)	Bandwidth (nm)
1	0.39	0.27	1377.26 – 1758.26	381.00
3	1.16	0.80	1484.79 – 1610.14	125.35
5	1.93	1.33	1508.28 – 1583.41	75.13
7	2.70	1.86	1518.58 – 1572.22	53.64
9	3.48	2.39	1524.36 – 1566.07	41.71
11	4.25	2.92	1528.06 – 1562.19	34.13
13	5.02	3.45	1530.63 – 1559.51	28.88
15	5.79	3.98	1532.52 – 1557.55	25.03
17	6.56	4.52	1533.97 – 1556.05	22.08
19	7.34	5.05	1535.12 – 1554.87	19.75

of which the reflectance is higher than 95 %. When the number  $N_{\text{slot}}$  of the air slots is below 5, the reflectances of the wavelengths in the C-band are all below 95 %, therefore the bandwidth of the high-reflectance region does not exist according to this definition. For further analysis, the number  $N_{\text{slot}}$  is chosen as 15 and the calculated bandwidth of the high-reflectance region versus  $m_{\text{quar}}$  in a Littrow mount are summarized in Table 4.1. By choosing  $m_{\text{quar}} = 11$  and  $N_{\text{slot}} = 15$ , the reflectances  $R$  for the TE and TM modes in a Littrow mount are shown in Fig. 4-4. Notice that the diffraction efficiency of a conventional metalized grating is polarization dependent, originating from the induced surface current of the metal. The proposed grating employing a dielectric mirror with a dielectric-air interface therefore would be able to mitigate this undesired loss.

## 4.2 2D Waveguide Analysis

In the slab waveguide region, the electromagnetic field are independent of the  $y$ -axis and only the transverse wave distributed along the  $z$ -axis is considered. To further evaluate the effect of etching depth on the reflectance and the bandwidth of the high-reflectance region, we further analyze the 2D waveguide with FullWAVE software from R-Soft. The waveguide structure of the etched trenches for one stack is coded into the software and the software layout is shown in Fig. 4-5. A Gaussian filed is chosen as the launch field at the input end. The light propagates through the slab waveguide to the dielectric mirror with a distance of  $100 \mu\text{m}$ , is partially reflected by the dielectric mirror, propagates through the slab waveguide to the time monitor, and is detected by the time monitor with a width of  $10 \mu\text{m}$ . For the accuracy of the simulation results, the grid size is chosen as  $0.06 \mu\text{m}$ . Fig. 4-6 shows the reflectances  $R$  for the TE and TM modes versus the etched depth  $D_{\text{etch}}$  in a Littrow mount with  $m_{\text{quar}} = 11$ . We can see that almost no light is reflected by the mirror until the trench is etched to the core layer. Then the reflectance increases sharply and then saturates when the trench reaches to the lower cladding layer. The reflectance maintain stable when the etched depth is higher than  $15 \mu\text{m}$ . Therefore, in our analysis the etched depth is chosen as  $15 \mu\text{m}$ . Most of light propagates in the core layer so the reflectance is low until the trench is etched through the core layer to reach the lower cladding layer.

Fig. 4-7 shows the reflectances  $R$  for the TE and TM modes versus  $m_{\text{quar}}$  in a Littrow

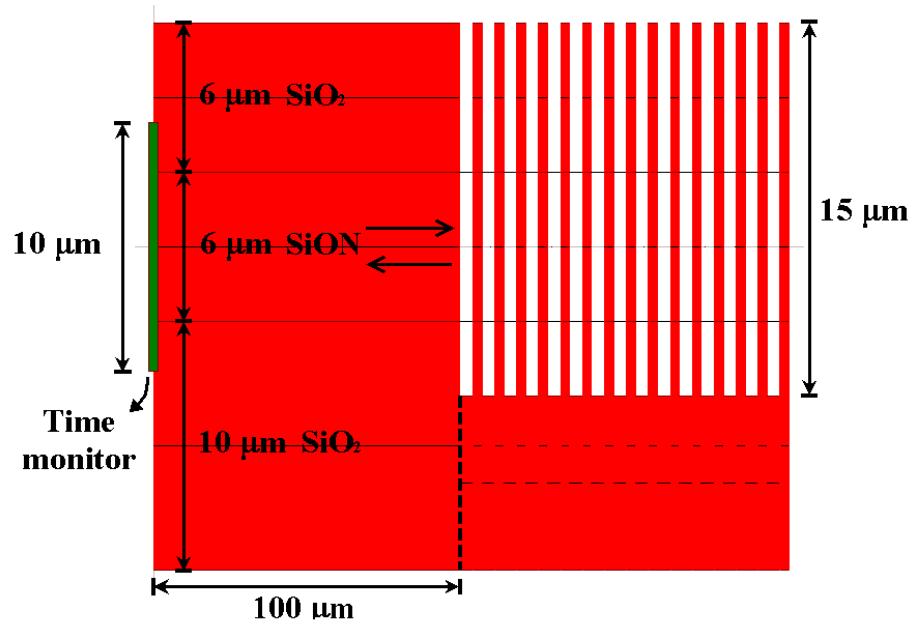


Figure 4-5: The software layout of the waveguide structure of the etched trenches for one stack.

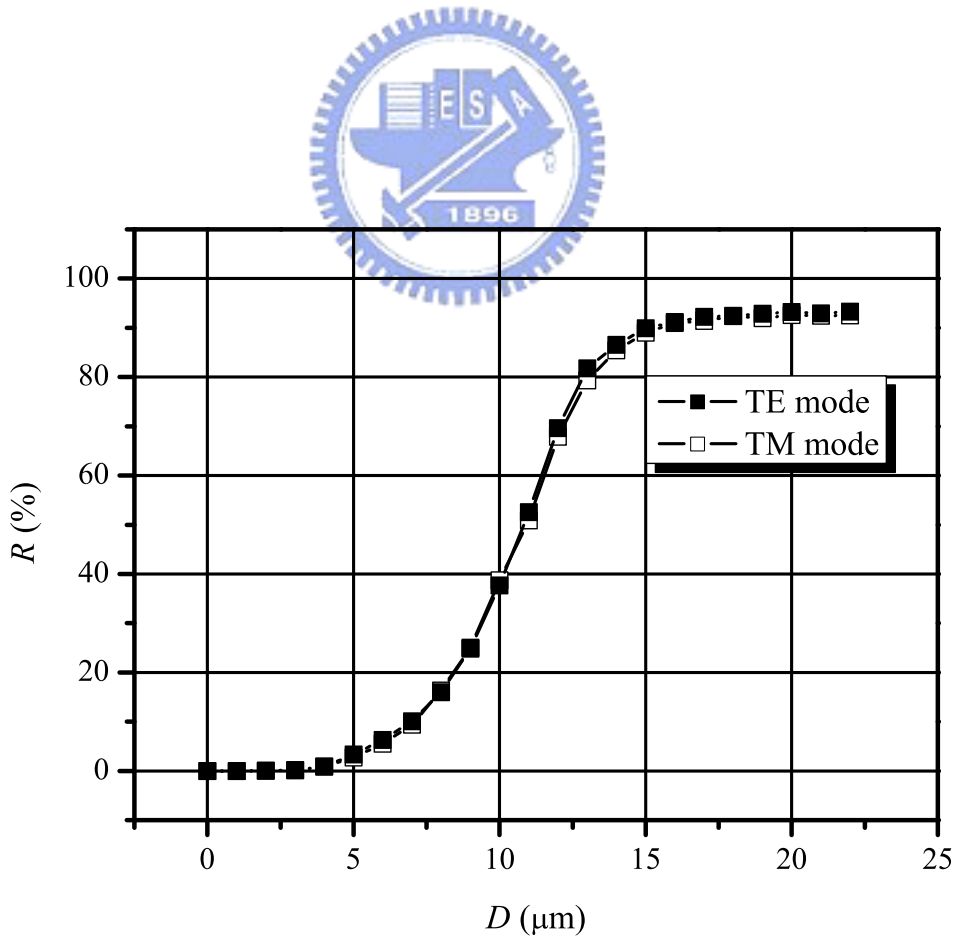


Figure 4-6: Reflectance  $R$  versus  $D_{\text{etch}}$  in a Littrow mount with  $m_{\text{quar}}$  of 11 and  $N_{\text{slot}}$  of 15 at a design wavelength  $\lambda_0$  of 1544.69 nm.



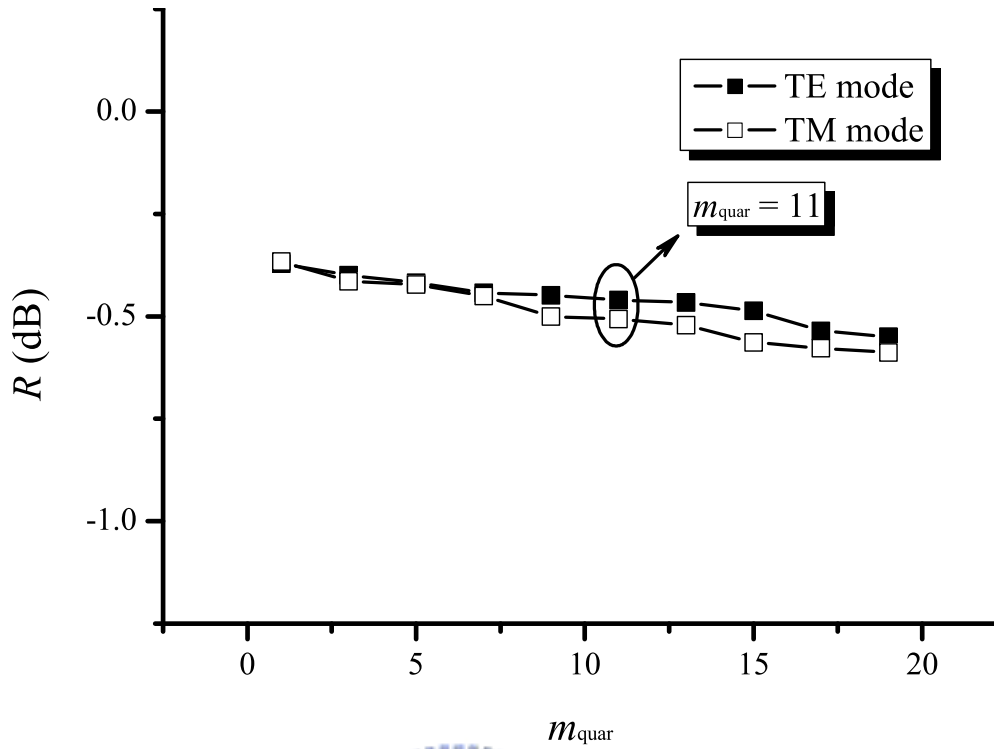


Figure 4-7: Reflectance  $R$  versus  $m_{\text{quar}}$  in a Littrow mount with  $N_{\text{slot}}$  of 15 and  $D_{\text{etch}}$  of  $15 \mu\text{m}$  at a design wavelength  $\lambda_0$  of  $1544.69 \text{ nm}$ .

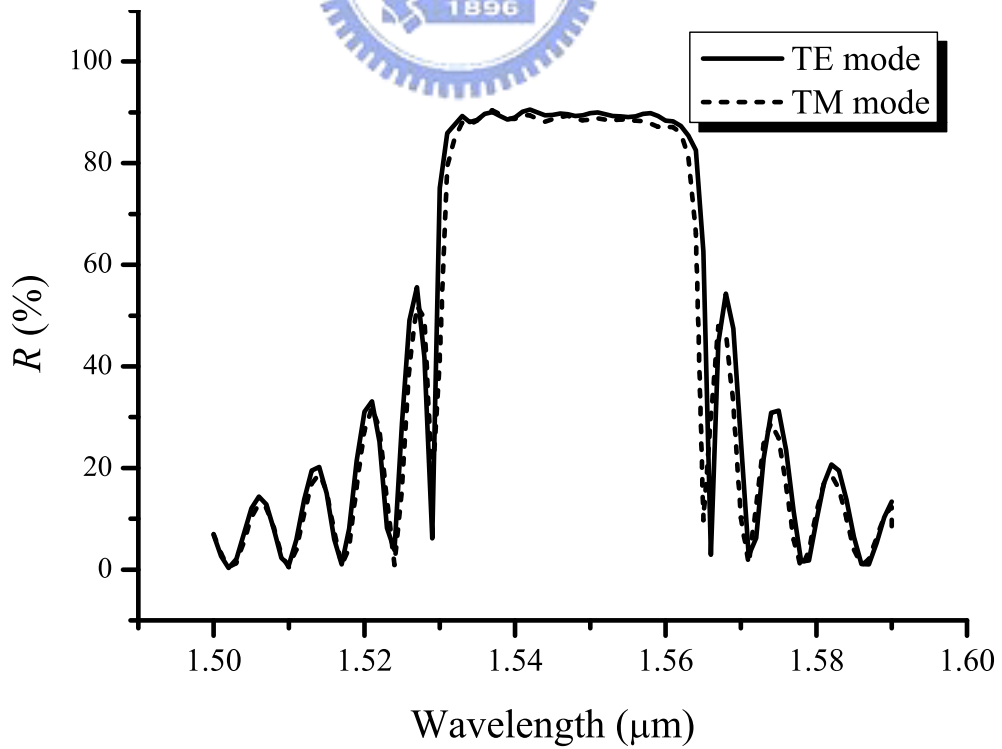


Figure 4-8: Reflectance  $R$  versus the corresponding wavelength in a Littrow mount with  $m_{\text{quar}}$  of 11,  $N_{\text{slot}}$  of 15, and  $D_{\text{etch}}$  of  $15 \mu\text{m}$  for the 2D waveguide analysis.

mount with  $N_{\text{slot}}$  of 15,  $D_{\text{etch}}$  of 15  $\mu\text{m}$ , and  $\lambda_0$  of 1544.69 nm. Simulation results show that the reflectances for both modes decrease as  $m_{\text{quar}}$  increases. The loss mainly comes from the scattering of light to the air when passing through the air slot. So when the width of the air slot increases with  $m_{\text{quar}}$ , it leads to a deterioration of the reflectance. The PDL, defined as the difference between the diffraction efficiencies for the TE and TM modes, is 0.05 dB with  $m_{\text{quar}}$  of 11,  $N_{\text{slot}}$  of 15, and  $D_{\text{etch}}$  of 15  $\mu\text{m}$ . Fig. 4-8 shows the reflectances  $R$  for the TE and TM modes versus the corresponding wavelength in a Littrow mount with  $m_{\text{quar}}$  of 11,  $N_{\text{slot}}$  of 15, and  $D_{\text{etch}}$  of 15  $\mu\text{m}$ . Compared with the results obtained from the transfer-matrix method, the reflectance and the bandwidth of the high-reflectance region both decrease and the reflectances for the TE and TM modes are slightly different in a Littrow mount. The reason is that the incident light used in the transfer matrix analysis is the plane wave while optical beam profile used in the 2D waveguide analysis has a finite beam waist, which turns out to have a large influence on the reflectance.

For a conventional design, the metal coating on the shaded facet is the main source of the PDL especially in a Littrow mount [24]. The induced surface current does not exist in a dielectric-air interface and the dielectric mirror mitigates the effect of the PDL. However, the grating nonideality due to the width variation  $\Delta w$  of the air slot and high-index stack during the fabrication process can significantly decrease the reflectance. The perturbed width  $w'_1$  and  $w'_h$  of the air slot and high-index stack can be expressed as

$$w'_1 = w_1 + \Delta w, \quad (4.10)$$

$$w'_h = w_h - \Delta w. \quad (4.11)$$

Fig. 4-9 shows that the additional loss increases as the width variation increases. Simulation results show that when the width variation  $\Delta w$  is below  $\pm 0.1 \mu\text{m}$  the losses can be kept below 0.04 dB for both modes so the width variation below 0.1  $\mu\text{m}$  is required to yield a dielectric mirror with high reflectance.

### 4.3 Summary

In summary, a planar waveguide concave grating employing dielectric mirrors is proposed to mitigate the PDL which comes from the induced surface current of the metal, especially

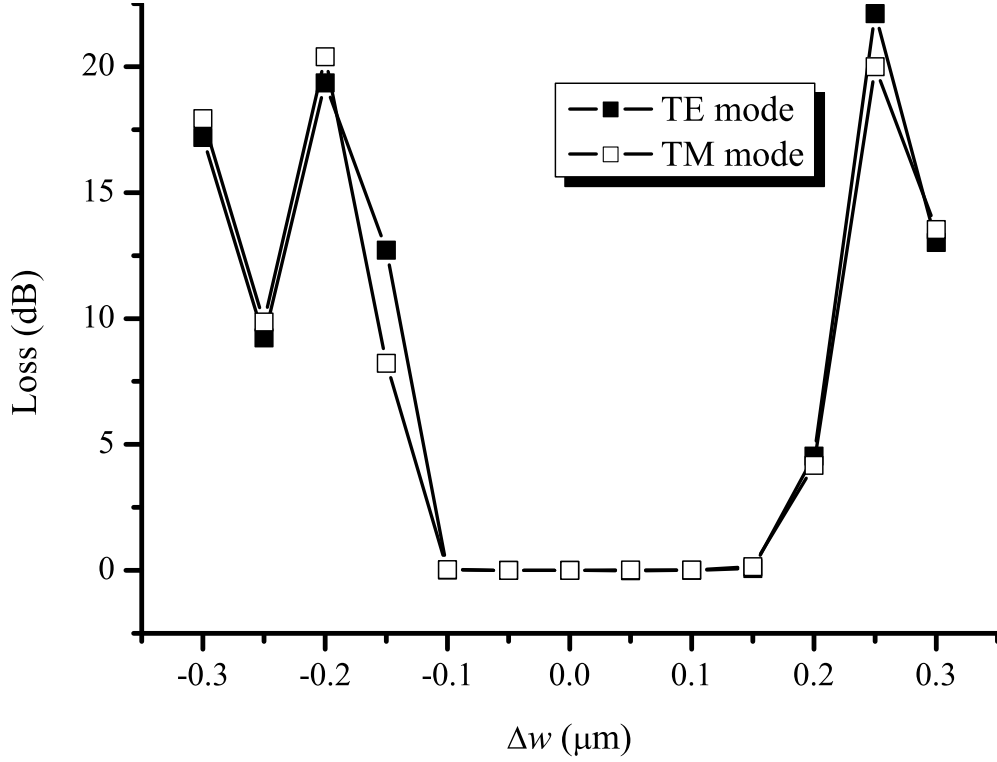


Figure 4-9: Loss due to the width variation  $\Delta w$  in a Littrow mount with  $m_{\text{quar}}$  of 11,  $N_{\text{slot}}$  of 15, and  $D_{\text{etch}}$  of  $15 \mu\text{m}$  at a design wavelength  $\lambda_0$  of  $1544.69 \text{ nm}$ .

in a Littrow mount. The transfer matrix method is used to obtain the reflectance  $R$  and the number  $N_{\text{slot}}$  of the air slots is chosen as 15. Simulation results show that the reflectance is high for a wide range of the wavelength. The FullWAVE software from R-Soft is used to analyze the reflectance  $R$  for the 2D waveguide with etched air slots. Simulation results show that a PDL of 0.05 dB can be achieved with  $m_{\text{quar}}$  of 11,  $N_{\text{slot}}$  of 15, and  $D_{\text{etch}}$  of  $15 \mu\text{m}$ . The impact of the fabrication error of etched air slots is also taken into account. To yield a proposed grating with high reflectance, the width variation  $\Delta w$  should be below  $\pm 0.1 \mu\text{m}$ .

# Chapter 5

## 16-Channel Optical Add-Drop Multiplexer

An optical add-drop multiplexer (OADM), which is capable of transmitting and dropping the wavelength signals selectively, play a crucial role in fiber-to-the-home (FTTH) systems. In a conventional design based on the planar waveguide devices, an OADM employs AWGs [2, 25]. However, AWGs encounter the inherent limits due to the lower free spectral range (FSR) and larger die size [10]. In this chapter, a novel OADM employing a planar waveguide concave grating is proposed. The arrangements of the components and the design considerations of the concave grating will be discussed in detail. The transmission characteristics are introduced for our analysis. A design example is used to analyze the spectral characteristics of the devices. The bending loss versus the radius of the curvature in a 90° arc channel waveguide for the fundamental TE mode ( $TE_0$ ) is also simulated.

### 5.1 Structure and Design Considerations

The schematic configuration of the 16-channel OADM, which consists of one planar waveguide concave grating, two input waveguides, two output waveguides, coupled waveguides, and sixteen sets of  $2 \times 2$  switches is shown in Fig. 5-1. 16 wavelength signals,  $\lambda_1, \lambda_2, \dots,$  and  $\lambda_{16}$ , are coupled out from the output end of input port 1 to the slab waveguide, while 16 waveguide signals,  $\lambda'_1, \lambda'_2, \dots,$  and  $\lambda'_{16}$ , with the same channel spacing are coupled out from the output end of input port 2 to the slab waveguide at the same time. The

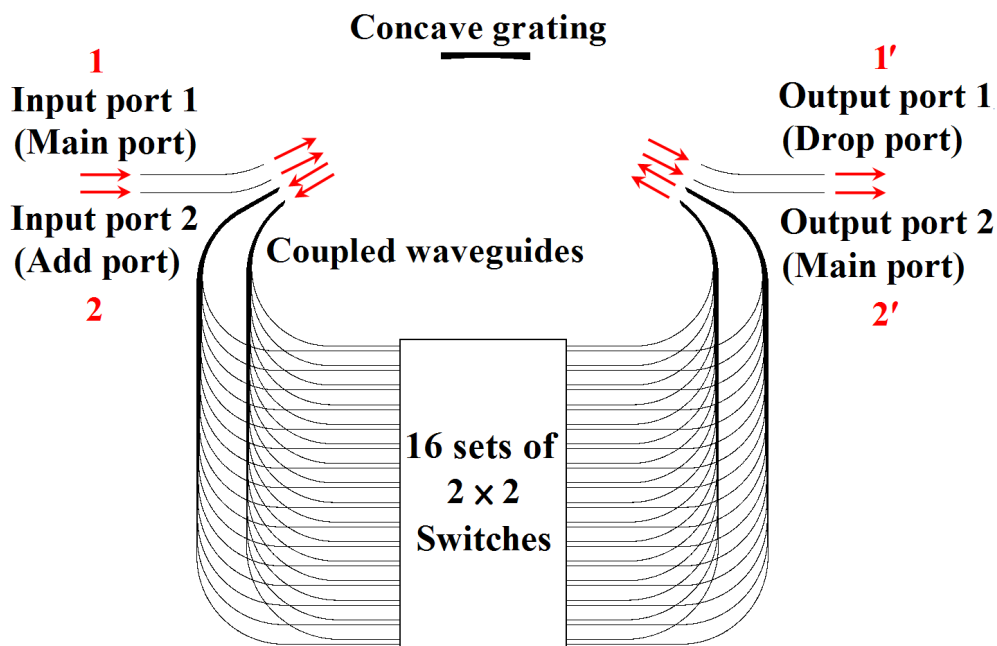


Figure 5-1: Schematic configuration of the 16-channel optical add-drop multiplexer system.

structures of the channel and slab waveguides are shown in Fig. 5-2. After propagating through the slab waveguide to the concave grating, they are diffracted by the concave grating, focused to the position along the imaging curve, and then coupled into the input ends of the different coupled waveguides according to the corresponding wavelengths as shown in Fig. 5-3. After transmitting and dropping the signals selectively by the  $2 \times 2$  switches [2, 25], the signals are coupled out from the output ends of the coupled waveguides to the slab waveguide. They are diffracted again by the concave grating, focused to the position along the imaging curve, and then coupled into the input ends of output port 1 and port 2. To perform the functions of the demultiplexing from the input port and the multiplexing to the output port, a concave grating with specifically designed tilt angles of two sides of the grating facets is proposed.

To design the concave grating, the structures of the channel and slab waveguides are chosen as shown in Fig. 5-2. By using the transfer-matrix method [29], the effective index  $n_{\text{eff}}$  in the slab waveguide can be solved. After the effective index  $n_{\text{eff}}$  in the slab waveguide is obtained, we choose the design wavelength  $\lambda_0$  in vacuum, the grating period  $d$  along the grating chord, the incident angle for the input port with respect to the  $y$ -axis at the grating pole, and the diffraction order  $m$ . Based on the diffraction formula of the plane grating from Eq. (3.17), the diffraction angle  $\beta(f_0)$  with respect to the  $y$ -axis at

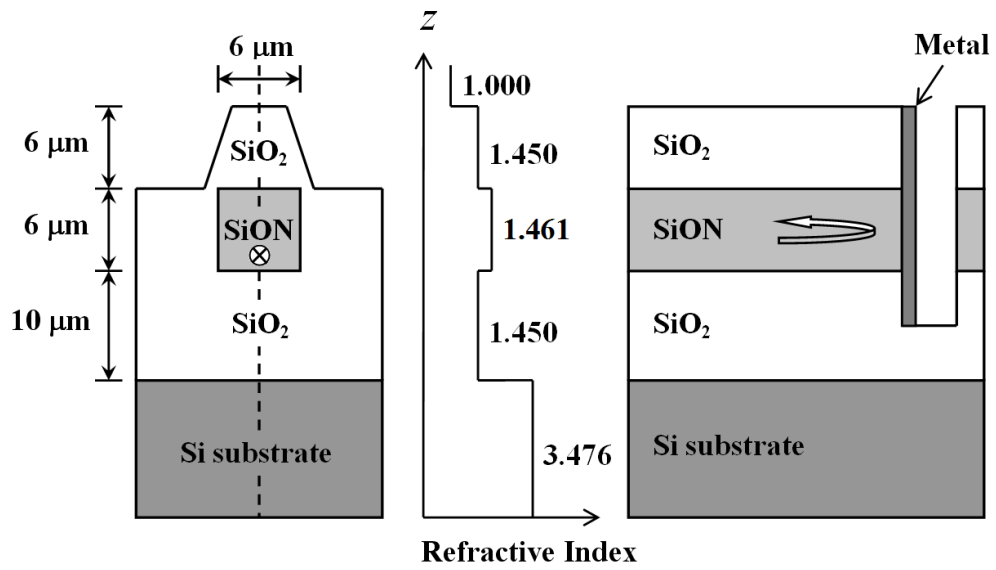


Figure 5-2: Side views of the single-mode channel waveguide (left) and the slab waveguide (right).

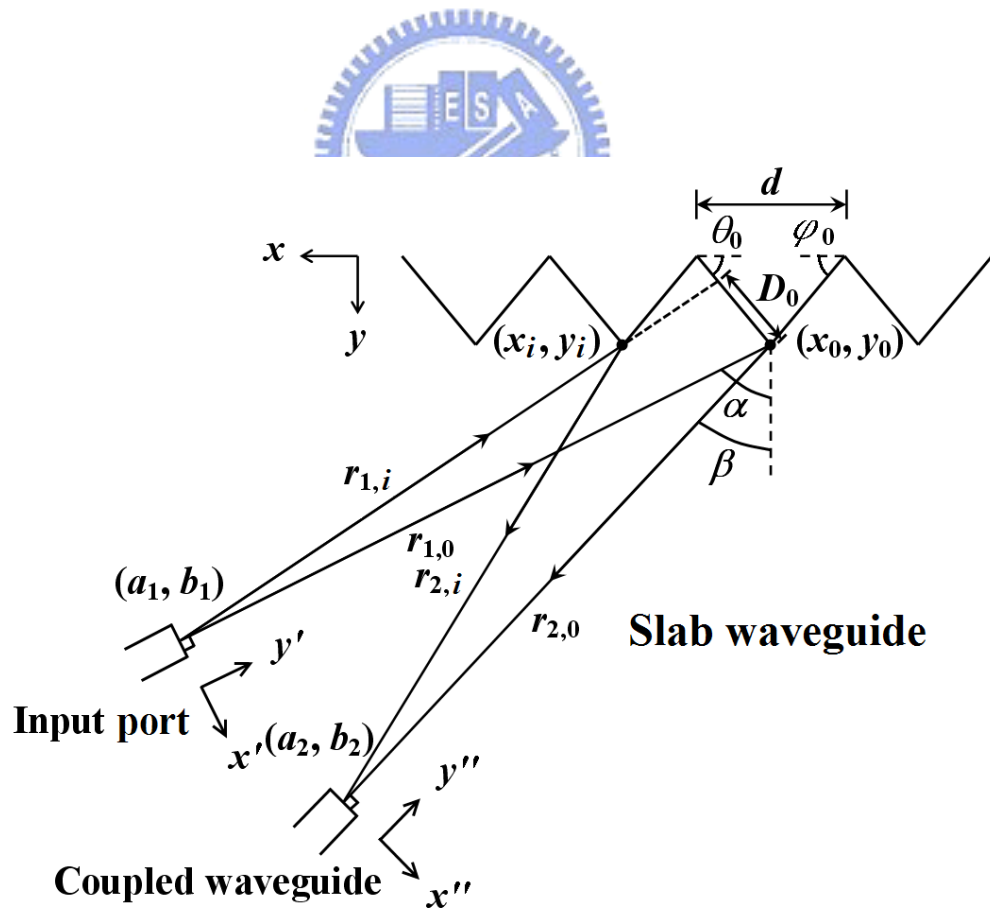


Figure 5-3: Schematic figure of the light propagating in the slab waveguide and being diffracted by the concave grating.

the grating pole can be obtained. As shown in Fig. 5-3, the distance  $r_{1,0}$  from the output end of the input port to the grating pole and the distance  $r_{2,0}(f_0)$  from the grating pole to the input end of the design coupled waveguide for the design wavelength  $\lambda_0$  with a corresponding frequency  $f_0$  are chosen. If the grating pole is chosen at the origin of the coordinates, the positions of the output end of the input port and the input end of the coupled waveguide can be obtained as  $(a_1, b_1) = (r_{1,0} \cdot \sin \alpha, r_{1,0} \cdot \cos \alpha)$  and  $(a_2, b_2) = (r_{2,0}(f_0) \cdot \sin \beta(f_0), r_{2,0}(f_0) \cdot \cos \beta(f_0))$ . The design of a planar waveguide concave grating here is based on the recursive definition of facet positions due to its superior spectral characteristics [32,34]. After determining the  $x$ -axis coordinate position of the vertex of the  $i$ th groove as  $x_i = i \cdot d$ , the free -aberration  $y$ -axis coordinate position  $y_i$  of the vertex of the  $i$ th groove for a design wavelength of  $\lambda_0$  can be obtained from the solution of the root for Eq.(3.6).

The optimum tilt angle  $\theta_i$  of the  $i$ th grating facet with respect to the  $x$ -axis is determined by Eq. (3.7). The optimum tilt angle  $\theta_i$  of the  $i$ th grating facet can be obtained as

$$\theta_i = \tan^{-1} \left( \frac{\frac{a_1 - x_i}{r_{1,i}} + \frac{a_2 - x_i}{r_{2,i}}}{\frac{b_1 - y_i}{r_{1,i}} + \frac{b_2 - y_i}{r_{2,i}}} \right). \quad (5.1)$$

The incident angle  $\alpha'$  ( $= -\alpha$ ) for the input end of the output port with respect to the  $y$ -axis at the grating pole, the diffraction order  $m'$  ( $= -m$ ), and the diffraction angle  $\beta'(f_0)$  ( $= -\beta(f_0)$ ) for the output end of the coupled waveguide with respect to the  $y$ -axis at the grating pole are determined. The distance  $r'_{1,0}$  ( $= r_{1,0}$ ) from the grating pole to the input end of the output port and the distance  $r'_{2,0}(f_0)$  ( $= r_{2,0}(f_0)$ ) from the output end of the coupled waveguide to the grating pole are chosen. The positions of the input end of the output port and the output end of the coupled waveguide can be obtained as  $(-a_1, b_1)$  and  $(-a_2, b_2)$ . The optimum tilt angle  $\varphi_i$  of the other side for the  $i$ th grating facet can be obtained as

$$\varphi_i = \tan^{-1} \left( -\frac{\frac{-a_1 - x_i}{r_{1,i}} + \frac{-a_2 - x_i}{r_{2,i}}}{\frac{b_1 - y_i}{r_{1,i}} + \frac{b_2 - y_i}{r_{2,i}}} \right). \quad (5.2)$$

The focal equation for the concave grating can be obtained from Eq. (3.8).  $\alpha$ ,  $\beta(f)$ ,  $r_{1,0}$ , and  $r_{2,0}(f)$  in Eq. (3.8) for the waves from the input port coupled to the corresponding coupled waveguides can be replaced with  $\alpha'$ ,  $\beta'(f)$ ,  $r'_{1,0}$ , and  $r'_{2,0}(f)$  for the waves from the corresponding coupled waveguides coupled to the output port. The numerical model

of the scalar diffraction theory for the concave grating in the planar waveguide can be obtained from Eq. (3.9).

At first, the signal at a frequency of  $f$  is coupled out from the output end of input port 2 (port 1) to the slab waveguide, diffracted by the concave grating, focused to the position along the imaging curve, and coupled into the input end of the  $j$ th coupled waveguide. The spectral response for the wave from input port 2 (port 1) to the  $j$ th coupled waveguide is denoted by  $I_{2,j}(f)$  ( $I_{1,j}(f)$ ) and can be obtained from the overlap integral of the imaging field with the mode field of the  $j$ th coupled waveguide. When the  $2 \times 2$  switch is turned off, it is in the cross state [25]. After the signal passes through the switch, the signal is coupled out from the output end of the  $j$ th coupled waveguide to the slab waveguide. The transmission efficiency of the light transmitted across the  $j$ th coupled waveguide, switch, and  $j$ th coupled waveguide is denoted by  $\eta_{j,2 \rightarrow 1'}$  ( $\eta_{j,1 \rightarrow 2'}$ ). Then the signal is diffracted again by the concave grating, focused to the position along the imaging curve, and coupled into the input end of output port 1 (port 2). The spectral response for the wave from the  $j$ th coupled waveguide to output port 1 (port 2) is denoted by  $I_{j,1'}(f)$  ( $I_{j,2'}(f)$ ) and can be obtained from the overlap integral of the imaging field with the mode field of output port 1 (port 2). We use the transmission characteristics  $T_{1'}(f)$  and  $T_{2'}(f)$  to denote the intensity of the light with a frequency of  $f$  detected at output port 1 and port 2. When all the switches are off, the transmission characteristics,  $T_{1'}(f)$  and  $T_{2'}(f)$ , can be expressed as

$$T_{1'}(f) = \sum_j I_{2,j}(f) \cdot \eta_{j,2 \rightarrow 1'} \cdot I_{j,1'}(f), \quad (5.3)$$

$$T_{2'}(f) = \sum_j I_{1,j}(f) \cdot \eta_{j,1 \rightarrow 2'} \cdot I_{j,2'}(f). \quad (5.4)$$

When the  $j$ th  $2 \times 2$  switch is turned on, it is in the bar state [25]. The  $j$ th terms  $I_{2,j}(f)$  and  $\eta_{j,2 \rightarrow 1'}$  in Eq. (5.3) will be replaced with  $I_{1,j}(f)$  and  $\eta_{j,1 \rightarrow 1'}$ , respectively, while the  $j$ th terms  $I_{1,j}(f)$  and  $\eta_{j,1 \rightarrow 2'}$  in Eq. (5.4) will be replaced with  $I_{2,j}(f)$  and  $\eta_{j,2 \rightarrow 2'}$ , respectively. Then the  $j$ th signal is extracted from input port 1 (port 2) to output port 1 (port 2). The transmission efficiencies will deteriorate due to the additional losses, including the bending losses of the coupled waveguide and the insertion loss of the switch. The thermo-optic (TO) phase shifter based on the temperature dependence refractive index change



of the silica waveguide can be used for the  $2 \times 2$  switches [2,18], since the TO switch can be integrated with the OADM on the Si substrate. The performance of the extinction ratios of OADM mainly depends on what kind of the  $2 \times 2$  switch is used and has been dramatically improved by using the double-gate TO switches [2,18].

## 5.2 Design Example and Characteristics

For a design example, the waveguide consists of a  $6\text{-}\mu\text{m}$ -thick SiON core layer with an upper  $6\text{-}\mu\text{m}$ -thick and a lower  $10\text{-}\mu\text{m}$ -thick SiO<sub>2</sub> cladding layers. The side views of the channel waveguide and the slab waveguide are shown in Fig. 5-2. The grating can be achieved by etching a trench to the lower cladding layer and then coated with metal at the back wall to enhance the reflectivity [10]. With a index difference  $\Delta$  of 0.75 %, the refractive indices of SiO<sub>2</sub> and SiON are 1.450 and 1.461, respectively, and the refractive index of the Si substrate is 3.476 at an operating wavelength of 1550.12 nm. By using the transfer-matrix method [29], there are two TE modes and TM modes in the slab waveguide region. However, only the fundamental even TE and TM modes are excited when the waves are coupled from the single-mode fiber to the channel waveguide. The effective indices for the fundamental even TE and TM modes are  $n_{\text{eff,TE}_0} = 1.45839$  and  $n_{\text{eff,TM}_0} = 1.45837$ , respectively. The problem of the polarization dependence is not serious in our case. The propagation losses due to the leakages to the silicon substrate can be neglected.

There are 16 channels in the C-band with a channel spacing of 0.4 nm (50 GHz) according to ITU grids [1]. We take the TE mode for example. The effective index for the fundamental TE mode (TE<sub>0</sub>) in the slab waveguide region is  $n_{\text{eff,TE}_0} = 1.45839$ . The design wavelength is  $\lambda_0 = 1550.12$  nm. The grating period along the grating chord is  $d = 10$   $\mu\text{m}$  and the incident angle for the design input port is  $\alpha = 62.00^\circ$ . The diffraction order is  $m = 16$  and the FSR ( $= \lambda_0/m$ ) can be calculated as 96.88 nm, while the FSR in [2] is 26.40 nm. Then the diffraction angle for the design coupled waveguide can be obtained as  $\beta(f_0) = 54.85^\circ$  from Eq. (3.17). The distance from the output end of the design input port to the grating pole is  $r_{1,0} = 25000$   $\mu\text{m}$  and the distance from the grating pole to the input end of the design coupled waveguide is  $r_{2,0} = 25000$   $\mu\text{m}$ . The position of the design input port and coupled waveguide can be obtained. The effective half widths

of the channel waveguides for the fundamental modes along the  $x'$ -axis and the  $x''$ -axis are  $4.35 \mu\text{m}$  obtained with BeamPROP software from R-Soft. The half angle  $\sigma$  for the Gaussian beam divergence at  $1/e$  amplitude can be obtained as  $4.46^\circ$  and the number of the grating periods is calculated as  $N = 828$ . After determining the position of the vertex of each groove from the solution of the root for Eq. (5-2), the effective radius of the grating curvature can be obtained as  $R = 47352 \mu\text{m}$  from Eq. (3.8).

The incident angles for input port 1 and port 2 are  $\alpha_1 = 64.00^\circ$  and  $\alpha_2 = 60.00^\circ$ , respectively, and the diffraction order is  $m = 16$ . Then the diffraction angles for the design wavelength can be obtained as  $\beta_1(f_0) = 53.31^\circ$  and  $\beta_2(f_0) = 56.58^\circ$ , respectively. The distance from the output ends of input port 1 and port 2 to the grating pole are  $25000 \mu\text{m}$  and the distances from the grating pole to the input ends of the corresponding coupled waveguides can be obtained from Eq. (3.8). The incident angles for output port 1 and port 2 are  $\alpha'_1 = -64.00^\circ$  and  $\alpha'_2 = -60.00^\circ$ , respectively, and the diffraction order is  $m' = -16$ . Then the diffraction angles for the design wavelength can be obtained as  $\beta'_1(f_0) = -53.31^\circ$  and  $\beta'_2(f_0) = -56.58^\circ$ , respectively. The distances from the grating pole to the input ends of output port 1 and port 2 are  $25000 \mu\text{m}$  and the distances from the output ends of the corresponding coupled waveguides to the grating pole can be obtained from Eq. (3.8).

Fig. 5-4 shows the bending loss versus the radius of the curvature in a  $90^\circ$  arc channel waveguide for the fundamental TE mode ( $\text{TE}_0$ ) at a design wavelength of  $1550.12 \text{ nm}$ , which is obtained with the 2D S-Bend waveguides in the BeamPROP software from R-Soft by using the effective index method (EIM). Here, we consider that only the fundamental even TE and TM modes are excited when the waves are coupled from the single-mode fiber to the channel waveguide. With a refractive index difference  $\Delta$  between the core layer and the cladding layer of  $0.75 \%$ , the bending radii of all the coupled waveguides in our case are chosen to be higher than  $7.5 \text{ mm}$  and the bending loss is lower than  $0.15 \text{ dB}$ . The bending loss of a channel waveguide in  $90^\circ$  arc at a wavelength of  $1.55 \mu\text{m}$  was found to be negligible for a index difference  $\Delta$  of  $0.75 \%$  with a core size of  $6 \times 6 \mu\text{m}^2$  when the radius of the curvature was more than  $5 \text{ mm}$  [45,46]. For the separation between two neighbor  $2 \times 2$  switches being chosen as  $2000 \mu\text{m}$ , the total die size in our case is  $70 \times 61 \text{ mm}^2$  with a channel spacing of  $50 \text{ GHz}$ , while the total die size in [2] is  $87 \times 74 \text{ mm}^2$  with a channel spacing of  $100 \text{ GHz}$ .

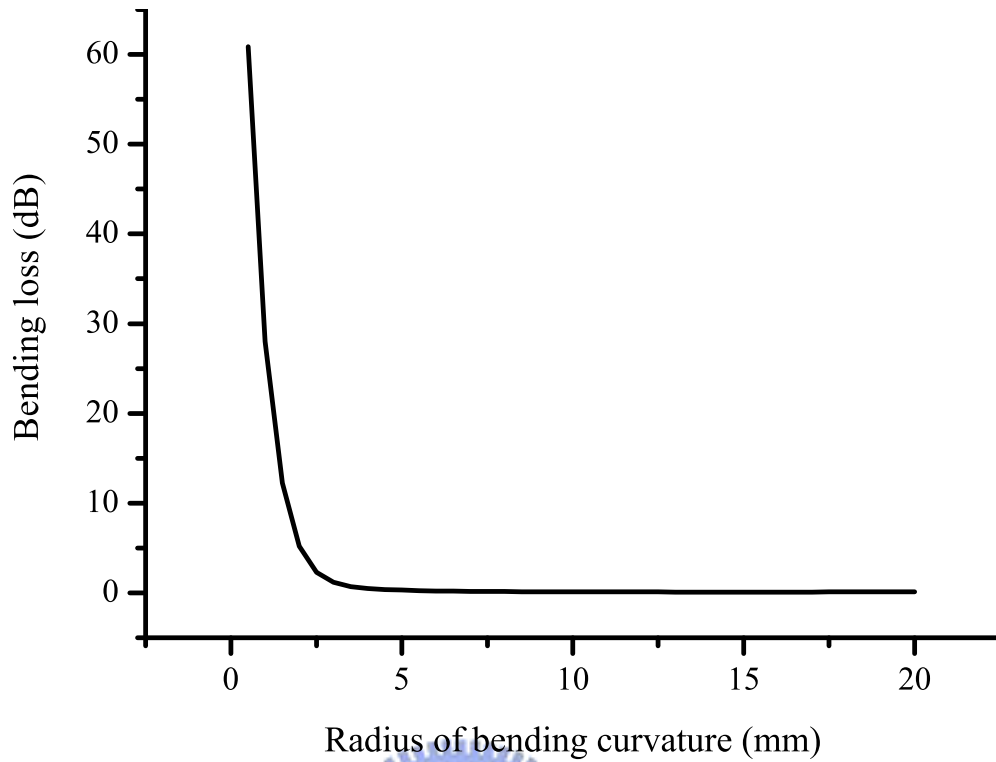


Figure 5-4: Bending loss versus the radius of the curvature in a  $90^\circ$  arc channel waveguide for the fundamental TE mode ( $TE_0$ ) at a design wavelength of 1550.12 nm.

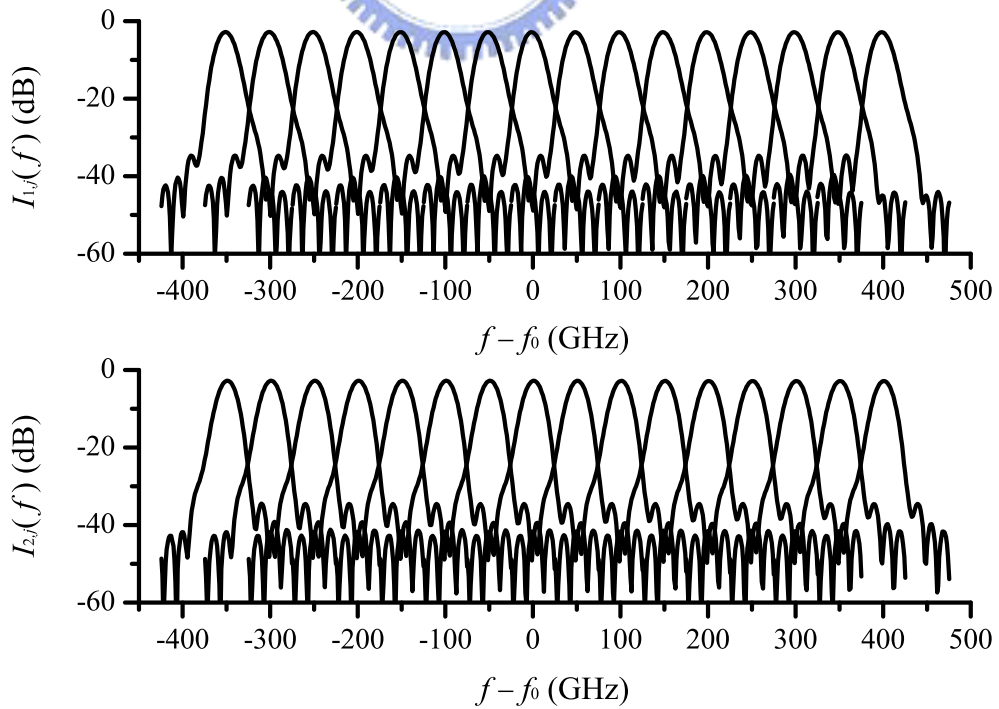


Figure 5-5: 16-channel spectral responses for the waves from input port 1 and port 2 coupled to the corresponding  $j$ th coupled waveguides.

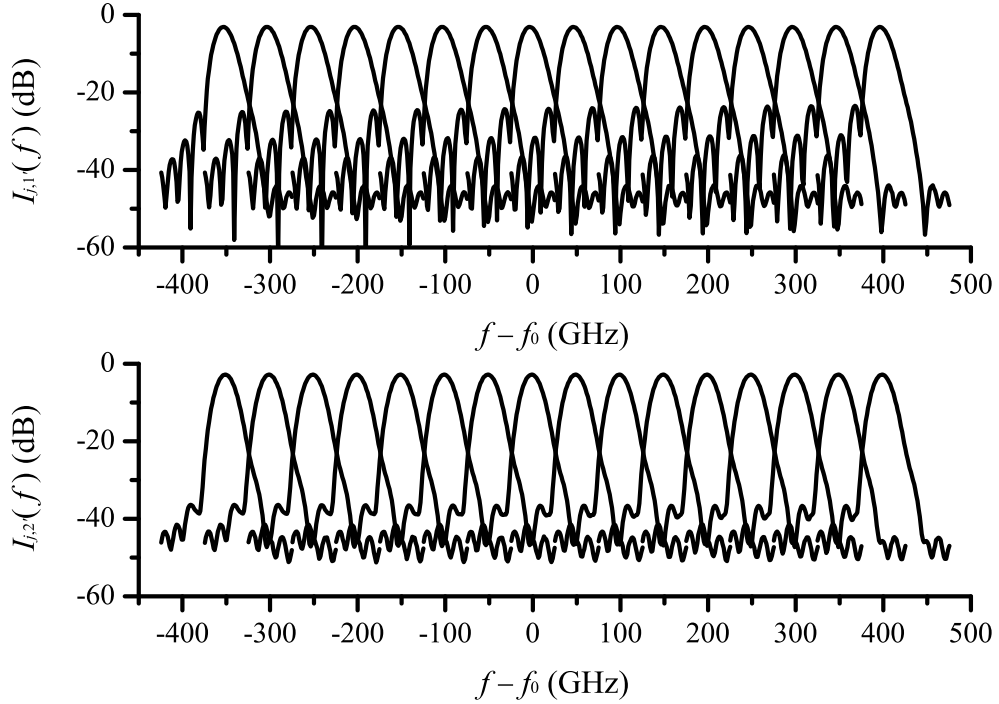


Figure 5-6: 16-channel spectral responses for the waves from the corresponding  $j$ th coupled waveguides coupled to output port 1 and port 2.

Without considering the scattering loss and side-wall tilt loss at the grating facet, the spectral responses,  $I_{1,j}$  and  $I_{2,j}$ , of the 16 channels for the waves from input port 1 and port 2 coupled to the corresponding  $j$ th coupled waveguides are shown in Fig. 5-5. Here, the fiber coupling loss is not considered. The insertion losses of the central channel are 2.90 and 2.81 dB, respectively, which include the excess loss and the undesired-order loss. The excess loss is the coupling loss from the slab waveguide to the coupled waveguide and the undesired-order loss is the loss for the diffraction of the light into undesired adjacent orders. The propagation loss due to the leakages to the silicon substrate is negligible in our case. The extinction ratio of a  $2 \times 2$  TO switch with a Mach-Zehnder interferometer configuration is higher than 30.00 dB and the insertion loss is about 1.00 dB [45, 47]. The double-gate TO switch is chosen in our analysis for a higher extinction ratio. The extinction ratio and insertion loss of the double-gate TO switch would be 60.00 and 2.00 dB, respectively, which are twice the extinction ratio and insertion loss of the single TO switch. The loss across the coupled waveguide and the switch is 2.30 dB, where 2.00 dB comes from the insertion loss of the switch and 0.30 dB comes from two bending losses of the coupled waveguide. So the transmission efficiencies for all the channels are chosen as  $-2.30$  dB. The spectral responses,  $I_{j,1'}$  and  $I_{j,2'}$ , of the 16 channels for the waves from the corresponding  $j$ th coupled waveguides coupled to output port 1 and port 2 are shown

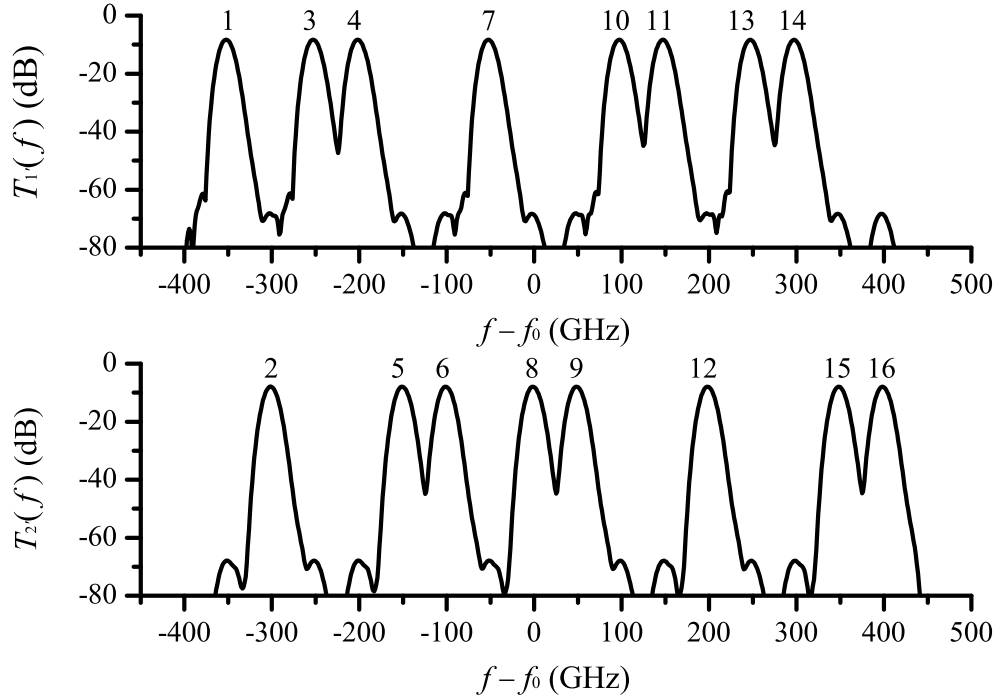


Figure 5-7: Transmission characteristics  $T_{1'}(f)$  and  $T_{2'}(f)$  at output port 1 and port 2.

in Fig. 5-6. The insertion losses of the central channel are 3.52 and 2.86 dB, respectively.

When the switches  $SW_1$ ,  $SW_3$ ,  $SW_4$ ,  $SW_7$ ,  $SW_{10}$ ,  $SW_{11}$ ,  $SW_{13}$ , and  $SW_{14}$ , for example, are turned on, the selected signals are extracted from the main port to the drop port. The transmission characteristics  $T_{1'}(f)$  and  $T_{2'}(f)$  are shown in Fig. 5-7. Here, the signals from the add port are not included. It shows that the extinction ratios are higher than 59.20 dB, which are predominated by the extinction ratios of the switches, with the insertion losses of 8.01 to 8.80 dB. The proposed scheme provides the design of an OADM with a higher FSR, smaller die size, and higher spectral resolution compared with [2,18].

### 5.3 Summary

In summary, a novel optical add-drop multiplexer employing a planar waveguide concave grating is proposed. The structures and design are discussed in detail. For the design example, the FSR is 96.88 nm and the total die size is  $70 \times 61 \text{ mm}^2$  with a separation between two neighbor  $2 \times 2$  switches of  $2000 \mu\text{m}$ . Simulation results show that the extinction ratios are higher than 59.20 dB with the insertion losses of 8.01 to 8.80 dB.

# Chapter 6

## Conclusion

In this dissertation, the characteristics of the planar waveguide concave gratings for the flat-top design have been investigated and the applications to integrated-optic components have been proposed. Analytic theories for the planar waveguide concave gratings have been reviewed. By introducing the characteristic matrix, the dispersion relations and effective indices for the TE and TM modes in multilayer slab waveguide can be obtained. Moreover, three-type designs of the concave gratings are introduced. Among the three types, the recursive-definition type is chosen for our analysis.

A modified formula for the three-focal-point method is proposed and compared with a numerical model of the scalar diffraction theory by a design example. Simulation results show that the deviation between two cases become serious as the ratio  $E_2/E_1$  of the peak amplitudes for the central and outmost subimages approaches unity. The changed passband width can be achieved by changing the ratio  $E_2/E_1$  of the peak amplitudes for the central and outmost subimages. The spectral response of the demultiplexer with a ripple below 0.04 dB is achieved.

The impact of fabrication errors relevant to the phase and amplitude errors on a flat-top planar waveguide demultiplexer is evaluated. Simulation results show that the phase errors caused by the deviations of the positions for the vertices of the grating facets are the main sources of the crosstalk, and the amplitude errors caused by the roundings of the grating corners and the grating side-wall angle offset from the vertical cause additional losses. When the standard deviation of the position errors increases from 0 to 100 nm, the mean value of the crosstalks for 50 samples increases from  $-36.34$  to  $-29.78$  dB. With a crosstalk criterion of  $-30$  dB in our case, a photomask resolution lower than 40

nm is required.

A five-focal-point method is also analyzed for the optimal design of a flat-top planar waveguide demultiplexer. The multiobjective genetic algorithm is used to optimize the parameters. A larger  $-1$ -dB passband width of 30.53 GHz and a lower ripple of  $1.09 \times 10^{-4}$  dB with a channel spacing of 50 GHz are achieved. It shows that the five-focal-point method gives a near-equivalent ratio of the  $-1$ -dB passband width to the channel spacing and a lower ripple  $R_{\text{ripple}}$  compared with the three-focal-point method based on the Gaussian approximation.

To mitigate the polarization-dependent loss (PDL) which comes from the induced surface current of the metal especially in a Littrow mount, a planar waveguide concave grating employing dielectric mirrors is proposed. The transfer-matrix method is used to obtain the reflectance  $R$  and the number  $N_{\text{slot}}$  of the air slots is chosen to be 15. Simulation results show that the reflectance is high for a wide range of the wavelength. The FullWAVE software from R-Soft is used to analyze the reflectance for the 2D waveguide with etched air slots. The PDL below 0.05 dB can be achieved with the odd multiple  $m_{\text{quar}}$  of quarter-wavelength being 11, the number  $N_{\text{slot}}$  of the air slots being 15, and the etched depth  $D_{\text{etch}}$  being  $15 \mu\text{m}$ . The impact of the fabrication error of etched air slots is also taken into account. To yield a proposed grating with high-reflectance, the width variation  $\Delta w$  should be below  $\pm 0.1 \mu\text{m}$ .

In addition, a novel optical add-drop multiplexer employing a planar waveguide concave grating for the higher free spectral range (FSR) and smaller die size is proposed. The structure and design are discussed in detail. For the design example, the FSR is 96.88 nm and the total device size is  $70 \times 61 \text{ mm}^2$  with a separation between two neighbor  $2 \times 2$  switches of  $2000 \mu\text{m}$ . Simulation results show that the extinction ratios are greater than 59.20 dB with the insertion losses of 8.01 to 8.80 dB.

In future work, based on the Gaussian approximation the relation between  $E_2/E_1$ , the ratio of the peak amplitudes for the central and outmost subimages, and  $a$ , the optimal half-separation between the two outmost subimages, should be added with the modified terms for a lower deviation compared with that obtained from the numerical analysis. An OADM employing a planar waveguide concave grating should be combined with the flat-top design for the temperature independent operation.



# Appendix A

## Characteristic Matrix

The general solution of the wave equations for the TE mode can be obtained as

$$\begin{aligned} U &= A \exp(-j\kappa x) + B \exp(+j\kappa x) \\ &= \frac{1}{2} (U_0 + V_0/\kappa) \cdot \exp(-j\kappa x) + \frac{1}{2} (U_0 - V_0/\kappa) \cdot \exp(+j\kappa x) \\ &= U_0 \cdot \cos(\kappa x) - V_0/\kappa \cdot j \sin(\kappa x), \end{aligned} \quad (\text{A.1})$$

$$\begin{aligned} V &= \kappa [A \exp(-j\kappa x) - B \exp(+j\kappa x)] \\ &= \kappa \left[ \frac{1}{2} (U_0 + V_0/\kappa) \cdot \exp(-j\kappa x) - \frac{1}{2} (U_0 - V_0/\kappa) \cdot \exp(+j\kappa x) \right] \\ &= \kappa [-U_0 \cdot j \sin(\kappa x) + V_0/\kappa \cdot \cos(\kappa x)]. \end{aligned} \quad (\text{A.2})$$

A rearrangement leads to a simple matrix relation between the input variables,  $U_0$  and  $V_0$ , and the output variables,  $U$  and  $V$ ,:

$$\begin{aligned} \begin{bmatrix} U \\ V \end{bmatrix} &= \begin{bmatrix} \cos(\kappa x) & (-j/\kappa) \sin(\kappa x) \\ -j\kappa \sin(\kappa x) & \cos(\kappa x) \end{bmatrix} \begin{bmatrix} U_0 \\ V_0 \end{bmatrix} \\ \Rightarrow \begin{bmatrix} U_0 \\ V_0 \end{bmatrix} &= \begin{bmatrix} \cos(\kappa x) & (j/\kappa) \sin(\kappa x) \\ j\kappa \sin(\kappa x) & \cos(\kappa x) \end{bmatrix} \begin{bmatrix} U \\ V \end{bmatrix}. \end{aligned} \quad (\text{A.3})$$



# Appendix B

## Modified Formula

Based on the Gaussian approximation, the spectral response of one channel can be obtained from the following overlap integral:

$$\begin{aligned}
 I(f) &= \left\{ E_1 \exp \left[ -\frac{(x'' + a - D_s(f - f_0))^2}{w_{\text{image}}^2} \right] + E_2 \exp \left[ -\frac{(x'' - D_s(f - f_0))^2}{w_{\text{image}}^2} \right] \right. \\
 &\quad \left. + E_3 \exp \left[ -\frac{(x'' - a - D_s(f - f_0))^2}{w_{\text{image}}^2} \right] \right\} \cdot \exp \left[ -\left( \frac{x''}{w_{\text{outwg}}} \right)^2 \right]^2 \\
 &= \left\{ E_1 \exp \left[ -\frac{(D_s(f - f_0) + a)^2}{w_{\text{image}}^2} \right] + E_2 \exp \left[ -\frac{(D_s(f - f_0))^2}{w_{\text{image}}^2} \right] \right. \\
 &\quad \left. + E_3 \exp \left[ -\frac{(D_s(f - f_0) - a)^2}{w_{\text{image}}^2} \right] \right\} \otimes \exp \left[ -\frac{(D_s(f - f_0))^2}{w_{\text{outwg}}^2} \right]^2 \\
 &= \left\{ E_1 \exp \left[ -\frac{(D_s(f - f_0) + a)^2}{w_{\text{image}}^2} \right] + E_2 \exp \left[ -\frac{(D_s(f - f_0))^2}{w_{\text{image}}^2} \right] \right. \\
 &\quad \left. + E_1 \exp \left[ -\frac{(D_s(f - f_0) - a)^2}{w_{\text{image}}^2} \right] \right\} \otimes \exp \left[ -\frac{(D_s(f - f_0))^2}{w_{\text{outwg}}^2} \right]^2 \\
 &= \left\{ 2E_1 \exp \left[ -\frac{a^2 + D_s^2(f - f_0)^2}{w_{\text{image}}^2 + w_{\text{outwg}}^2} \right] \cdot \cosh \left[ \frac{2aD_s(f - f_0)}{w_{\text{image}}^2 + w_{\text{outwg}}^2} \right] \right. \\
 &\quad \left. + E_2 \exp \left[ -\frac{D_s^2(f - f_0)^2}{w_{\text{image}}^2 + w_{\text{outwg}}^2} \right] \right\}^2. \tag{B.1}
 \end{aligned}$$

The first-order derivative of the spectral response can be expressed as

$$\begin{aligned}
I'(f) = & 2 \left\{ 2E_1 \exp \left[ -\frac{a^2 + D_s^2 (f - f_0)^2}{w_{\text{image}}^2 + w_{\text{outwg}}^2} \right] \cdot \cosh \left[ \frac{2aD_s (f - f_0)}{w_{\text{image}}^2 + w_{\text{outwg}}^2} \right] \right. \\
& \left. + E_2 \exp \left[ -\frac{D_s^2 (f - f_0)^2}{w_{\text{image}}^2 + w_{\text{outwg}}^2} \right] \right\} \\
& \times \left\{ 2E_1 \cdot \left[ -\frac{2D_s^2 (f - f_0)}{w_{\text{image}}^2 + w_{\text{outwg}}^2} \right] \cdot \exp \left[ -\frac{a^2 + D_s^2 (f - f_0)^2}{w_{\text{image}}^2 + w_{\text{outwg}}^2} \right] \cdot \cosh \left[ \frac{2aD_s (f - f_0)}{w_{\text{image}}^2 + w_{\text{outwg}}^2} \right] \right. \\
& + 2E_1 \cdot \left[ \frac{2aD_s}{w_{\text{image}}^2 + w_{\text{outwg}}^2} \right] \cdot \exp \left[ -\frac{a^2 + D_s^2 (f - f_0)^2}{w_{\text{image}}^2 + w_{\text{outwg}}^2} \right] \cdot \sinh \left[ \frac{2aD_s (f - f_0)}{w_{\text{image}}^2 + w_{\text{outwg}}^2} \right] \\
& \left. + E_2 \cdot \left[ -\frac{2D_s^2 (f - f_0)}{w_{\text{image}}^2 + w_{\text{outwg}}^2} \right] \cdot \exp \left[ -\frac{D_s^2 (f - f_0)^2}{w_{\text{image}}^2 + w_{\text{outwg}}^2} \right] \right\}. \tag{B.2}
\end{aligned}$$

The second-order derivative of the spectral response at a central frequency of  $f_0$  can be simplified as

$$\begin{aligned}
I''(f_0) = & 2 \left[ 2E_1 \exp \left( -\frac{a^2}{w_{\text{image}}^2 + w_{\text{outwg}}^2} \right) + E_2 \right] \\
& \times \left[ 2E_1 \cdot \left( -\frac{2D_s^2}{w_{\text{image}}^2 + w_{\text{outwg}}^2} \right) \cdot \exp \left( -\frac{a^2}{w_{\text{image}}^2 + w_{\text{outwg}}^2} \right) \right. \\
& + 2E_1 \cdot \left( \frac{2aD_s}{w_{\text{image}}^2 + w_{\text{outwg}}^2} \right)^2 \cdot \exp \left( -\frac{a^2}{w_{\text{image}}^2 + w_{\text{outwg}}^2} \right) \\
& \left. + E_2 \cdot \left( -\frac{2D_s^2}{w_{\text{image}}^2 + w_{\text{outwg}}^2} \right) \right] \\
= & 2 \left[ 2E_1 \exp \left( -\frac{a^2}{w_{\text{image}}^2 + w_{\text{outwg}}^2} \right) + E_2 \right] \\
& \times \left[ 2E_1 \cdot \left( \frac{2D_s^2}{w_{\text{image}}^2 + w_{\text{outwg}}^2} \right) \cdot \exp \left( -\frac{a^2}{w_{\text{image}}^2 + w_{\text{outwg}}^2} \right) \cdot \left( -1 + \frac{2a^2}{w_{\text{image}}^2 + w_{\text{outwg}}^2} \right) \right. \\
& \left. + E_2 \cdot \left( -\frac{2D_s^2}{w_{\text{image}}^2 + w_{\text{outwg}}^2} \right) \right]. \tag{B.3}
\end{aligned}$$

For the flat spectral response, the second-order derivative of the spectral response at a central frequency of  $f_0$  should be zero and the following formula can be obtained:

$$\begin{aligned}
& 2E_1 \cdot \left( \frac{2D_s^2}{w_{\text{image}}^2 + w_{\text{outwg}}^2} \right) \cdot \exp \left( -\frac{a^2}{w_{\text{image}}^2 + w_{\text{outwg}}^2} \right) \cdot \left( -1 + \frac{2a^2}{w_{\text{image}}^2 + w_{\text{outwg}}^2} \right) \\
& + E_2 \cdot \left( -\frac{2D_s^2}{w_{\text{image}}^2 + w_{\text{outwg}}^2} \right) = 0 \\
\Rightarrow & 2E_1 \cdot \left( \frac{2D_s^2}{w_{\text{image}}^2 + w_{\text{outwg}}^2} \right) \cdot \exp \left( -\frac{a^2}{w_{\text{image}}^2 + w_{\text{outwg}}^2} \right) \cdot \left( -1 + \frac{2a^2}{w_{\text{image}}^2 + w_{\text{outwg}}^2} \right) \\
& = E_2 \cdot \left( \frac{2D_s^2}{w_{\text{image}}^2 + w_{\text{outwg}}^2} \right) \\
\Rightarrow & 2E_1 \exp \left( -\frac{a^2}{w_{\text{image}}^2 + w_{\text{outwg}}^2} \right) \cdot \left( -1 + \frac{2a^2}{w_{\text{image}}^2 + w_{\text{outwg}}^2} \right) = E_2 \\
\Rightarrow & \frac{E_2}{E_1} = 2 \exp \left( -\frac{a^2}{w_{\text{image}}^2 + w_{\text{outwg}}^2} \right) \cdot \left( \frac{2a^2}{w_{\text{image}}^2 + w_{\text{outwg}}^2} - 1 \right). \tag{B.4}
\end{aligned}$$



# Bibliography

- [1] S. V. Kartalopoulos, *Introduction to DWDM Technology*. New York: IEEE Press, 2000, pp. 175–203.
- [2] K. Okamoto, M. Okuno, A. Himeno, and Y. Ohmori, “16-channel optical add/drop multiplexer consisting of arrayed-waveguide gratings and double-gate switches,” *Electron. Lett.*, vol. 32, no. 16, pp. 1471–1472, Aug. 1996.
- [3] A. Rigny, A. Bruno, and H. Sik, “Multigrating method for flattened spectral response wavelength multi/demultiplexer,” *Electron. Lett.*, vol. 33, no. 20, pp. 1701–1702, Sept. 1997.
- [4] K. Takada, M. Ade, T. Shibita, and K. Okamoto, “A 25-GHz-spaced 1080-channel tandem multi/demultiplexer covering the S-, C-, and L-bands using an arrayed-waveguide grating with Gaussian passbands as primary filter,” *IEEE Photon. Technol. Lett.*, vol. 14, no. 5, pp. 648–650, May 2002.
- [5] J.-J. He, B. Lamontagne, A. Delâge, L. Erickson, M. Davies, and E. S. Koteles, “Monolithic integrated wavelength demultiplexer based on a waveguide Rowland circle grating in InGaAsP/InP,” *J. Lightwave Technol.*, vol. 16, no. 4, pp. 631–638, Apr. 1998.
- [6] J.-J. He, E. S. Koteles, B. Lamontagne, L. Erickson, A. Delâge, and M. Davies, “Integrated polarization compensator for WDM waveguide demultiplexers,” *IEEE Photon. Technol. Lett.*, vol. 11, no. 2, pp. 321–322, Feb. 1999.
- [7] Z. Shi and S. He, “A three-focal-point method for the optimal design of a flat-top planar waveguide demultiplexer,” *IEEE J. Sel. Top. Quantum Electron.*, vol. 8, no. 6, pp. 1179–1185, Nov./Dec. 2002.

- [8] J.-J. He, "Phase-dithered waveguide grating with flat passband and sharp transitions," *IEEE J. Sel. Top. Quantum Electron.*, vol. 8, no. 6, pp. 1186–1193, Nov./Dec. 2002.
- [9] J. Song, D. Pang, and S. He, "A planar waveguide demultiplexer with a flat passband, sharp transitions and a low chromatic dispersion," *Opt. Commun.*, vol. 227, pp. 89–97, 2003.
- [10] S. Janz, A. Balakrishnan, S. Charbonneau, P. Cheben, M. Cloutier, A. Delâge, K. Dossou, L. Erickson, M. Gao, P. A. Krug, B. Lamontagne, M. Packirisamy, M. Pearson, and D.-X. Xu, "Planar waveguide echelle gratings in silica-on-silicon," *IEEE Photon. Technol. Lett.*, vol. 16, no. 2, pp. 503–505, Feb. 2004.
- [11] H. W. Yen, H. R. Friedrich, R. J. Morrison, and G. L. Tangonan, "Planar Rowland spectrometer for fiber-optic wavelength demultiplexing," *Opt. Lett.*, vol. 6, no. 12, pp. 639–641, Dec. 1981.
- [12] Y. Fujii and J. Minowa, "Optical demultiplexer using a silicon concave diffraction grating," *Appl. Opt.*, vol. 22, no. 7, pp. 974–978, Apr. 1983.
- [13] E. Gini, W. Hunziker, and H. Melchior, "Polarization independent InP WDM multiplexer/demultiplexer module," *J. Lightwave Technol.*, vol. 16, no. 4, pp. 625–630, Apr. 1998.
- [14] X. Chen, J. N. McMullin, C. J. Haugen, and R. G. DeCorby, "Planar concave grating demultiplexer for coarse WDM based on confocal ellipses," *Opt. Commun.*, vol. 237, pp. 71–77, 2004.
- [15] M. Ishikawa, T. Miura, A. Matsutani, and F. Koyama, "Design and fabrication of grating demultiplexer using hollow optical waveguide," *Jpn J. Appl. Phys.*, vol. 43, no. 8B, pp. 5761–5765, Aug. 2004.
- [16] J. B. D. Soole, K. R. Poguntke, A. Scherer, H. P. LeBlanc, C. Chang-Hasnain, J. R. Hayes, C. Caneau, R. Bhat, and M. A. Koza, "Wavelength-selectable laser emission from a multistriple array grating integrated cavity laser," *Appl. Phys. Lett.*, vol. 61, no. 23, pp. 2750–2752, Dec. 1992.

- [17] Y. Inoue, A. Kaneko, F. Hanawa, H. Takahashi, K. Hattori, and S. Sumida, "Athermal silica-based arrayed-waveguide grating multiplexer," *Electron. Lett.*, vol. 33, no. 23, pp. 1945–1947, 1997.
- [18] T. Saida, A. Kaneko, T. Goh, M. Okuno, A. Himeno, K. Takiguchi, and K. Okamoto, "Athermal silica-based optical add/drop multiplexer consisting of arrayed waveguide gratings and double gate thermo-optical switches," *Electron. Lett.*, vol. 36, no. 6, pp. 528–529, 2000.
- [19] M. R. Amersfoort, J. B. D. Soole, H. P. LeBlanc, N. C. Andreadakis, A. Rajhel, and C. Caneau, "Passband broadening of integrated arrayed waveguide filters using multimode interference couplers," *Electron. Lett.*, vol. 32, no. 5, pp. 449–451, Feb. 1996.
- [20] C. Dragone, "Efficient techniques for widening the passband of a wavelength router," *J. Lightwave Technol.*, vol. 16, no. 10, pp. 1895–1906, Oct. 1998.
- [21] C. R. Doerr, L. W. Stulz, and R. Pafchek, "Compact and low-loss integrated box-like passband multiplexer," *IEEE Photon. Technol. Lett.*, vol. 15, no. 7, pp. 918–920, July 2003.
- [22] Z. Shi, J.-J. He, and S. He, "An analytic method for designing passband flattened DWDM demultiplexers using spatial phase modulation," *J. Lightwave Technol.*, vol. 21, no. 10, pp. 2314–2321, Oct. 2003.
- [23] C. Dragone, "Low-loss wavelength routers for WDM optical networks and high-capacity IP routers," *J. Lightwave Technol.*, vol. 23, no. 1, pp. 66–79, Jan. 2005.
- [24] Z. Shi, J.-J. He, and S. He, "Waveguide echelle grating with low polarization-dependent loss using single-side metal-coated grooves," *IEEE Photon. Technol. Lett.*, vol. 16, no. 8, pp. 1885–1887, Aug. 2004.
- [25] K. Okamoto, K. Takiguchi, and Y. Ohmori, "16-channel optical add/drop multiplexer using silica-based arrayed-waveguide gratings," *Electron. Lett.*, vol. 31, no. 9, pp. 723–724, Apr. 1995.

- [26] C.-T. Lin, Y.-T. Huang, and J.-Y. Huang, “The impact of fabrication errors on a flat-top grating-based planar waveguide demultiplexer,” *Jpn J. Appl. Phys.*, vol. 46, no. 11, pp. 7356–7358, Nov. 2007.
- [27] M. Mitchell, *An Introduction to Genetic Algorithms*. London: MIT Press, 1996, pp. 1–12.
- [28] C.-T. Lin, Y.-T. Huang, and J.-Y. Huang, “A planar waveguide concave grating employing dielectric mirrors,” *Opt. Commun.*, vol. 281, pp. 1072–1076, 2008.
- [29] H. Kogelnik, “Theory of optical waveguides,” in *Guided-Wave Optoelectronics*, T. Tamir, Ed. Berlin, Germany: Springer-Verlag, 1990, ch. 2.
- [30] M. C. Hutley, *Diffraction Gratings*. London: Academic Press, 1982.
- [31] W. B. Peatman, *Gratings, Mirrors and Slits: Beamline Design for Soft X-Ray Synchrotron Radiation Sources*. Netherlands: Gordon and Breach Science Publishers, 1997.
- [32] K. A. McGreer, “Theory of concave gratings based on a recursive definition of facet positions,” *Appl. Opt.*, vol. 35, no. 30, pp. 5904–5910, Oct. 1996.
- [33] H. Nishihara, M. Haruna, and T. Suhara, “Optical waveguide theory,” in *Optical Integrated Circuits*. New York: McGraw-Hill, 1989, ch. 2.
- [34] C.-T. Lin, Y.-T. Huang, J.-Y. Huang, and H.-H. Lin, “Integrated planar waveguide concave gratings for high density WDM systems,” in *2005 Optical Communications Systems and Networks (OCSN 2005)*, Banff, Alberta, Canada, July 19–21, 2005, pp. 98–102.
- [35] K. A. McGreer, “Diffraction from concave gratings in planar waveguides,” *IEEE Photon. Technol. Lett.*, vol. 7, no. 3, pp. 324–326, Mar. 1995.
- [36] C. D. Lee, W. Chen, Q. Wang, Y.-J. Chen, W. T. Beard, D. Stone, R. F. Smith, R. Mincher, and I. R. Stewart, “The role of photomask resolution on the performance of arrayed-waveguide grating devices,” *J. Lightwave Technol.*, vol. 19, no. 11, pp. 1726–1733, Nov. 2001.

- [37] Y. Chu, X. Zheng, H. Zhang, X. Liu, and Y. Guo, "The impact of phase errors on arrayed waveguide gratings," *IEEE J. Sel. Top. Quantum Electron.*, vol. 8, no. 6, pp. 1122–1129, Nov./Dec. 2002.
- [38] H. Wen, D. Pang, and Z. Qiang, "The impact of phase and amplitude errors on an etched diffraction grating demultiplexer," *Opt. Commun.*, vol. 236, pp. 1–6, 2004.
- [39] R. J. Deri, J. S. Kallman, and S. P. Djajili, "Quantitative analysis of integrated optic waveguide spectrometers," *IEEE Photon. Technol. Lett.*, vol. 6, no. 2, pp. 242–244, Feb. 1994.
- [40] W. van Etten and J. van der Plaats, *Fundamentals of Optical Fiber Communications*. New York: Prentice-Hall, 1991, p. 253.
- [41] Z. Shi, J.-J. He, and S. He, "Analysis and design of a concave diffraction grating with total-internal-reflection facets by a hybrid diffraction method," *J. Opt. Soc. Am. A*, vol. 21, no. 7, pp. 1198–1206, July 2004.
- [42] J. Song, J.-J. He, and S. He, "Polarization performance analysis of etched diffraction grating demultiplexer using boundary element method," *IEEE J. Sel. Top. Quantum Electron.*, vol. 11, no. 1, pp. 224–231, Jan./Feb. 2005.
- [43] J. Song, J.-J. He, and S. He, "Fast analysis method for polarization-dependent performance of a concave diffraction grating with total-internal-reflection facets," *J. Opt. Soc. Am. A*, vol. 22, no. 9, pp. 1947–1951, Sept. 2005.
- [44] F. L. Pedrotti and L. S. Pedrotti, "Theory of multilayer films," in *Introduction to Optics*. New Jersey: Prentice-Hall, 1993, ch. 19.
- [45] M. Kawachi, "Silica waveguides on silicon and their application to integrated-optic components," *Opt. Quantum Electron.*, vol. 22, no. 5, pp. 391–416, Sept. 1990.
- [46] N. Takato, K. Jinguji, M. Yasu, H. Toba, and M. Kawachi, "Low-loss high-silica single-mode channel waveguides," *Electron. Lett.*, vol. 22, no. 6, pp. 321–322, Mar. 1986.
- [47] X. Wu, L. Liu, Y. Zhang, D. Li, W. Wang, and L. Xu, "Low electric power driven thermo-optic multimode interference switches with tapered heating electrodes," *Opt. Commun.*, vol. 258, pp. 135–143, 2006.



# 簡 歷

## 一、基本資料

姓 名：林 俊 廷

英文姓名：Lin, Chun-Ting

姓 別：男

出生日期：民國六十六年六月七日

籍 貫：台北市

## 二、主要學歷

國立交通大學電子物理學系 1996/09 - 2000/06

國立交通大學電子物理研究所碩士班 2000/09 - 2002/06

國立交通大學光電工程研究所博士班 2002/09 - 2008/07

## 三、博士論文：平面波導式凹面光柵元件之設計、分析與應用

Design, Analysis, and Application of the Planar Waveguide Concave  
Grating Devices



## 四、著作

### A. 期刊論文

1. C.-T. Lin, Y.-T. Huang, and J.-Y. Huang, "The impact of fabrication errors on a flat-top grating-based planar waveguide demultiplexer," *Japan Journal of Applied Physics*, vol. 46, no. 11, pp. 7356–7358, Nov. 2007.
2. C.-T. Lin, Y.-T. Huang, and J.-Y. Huang, "A planar waveguide concave grating employing dielectric mirrors," *Optics Communications*, vol. 281, pp.1072–1076, 2008.
3. C.-T. Lin, Y.-T. Huang, and J.-Y. Huang, "Quantitative analysis of a flat-top planar waveguide demultiplexer," accepted for publication in *Journal of Lightwave Technology*.
4. C.-T. Lin, Y.-T. Huang, and J.-Y. Huang, "16-channel optical add-drop multiplexer employing a planar waveguide concave grating," submitted to *Journal of Lightwave Technology*.
5. C.-T. Lin, Y.-T. Huang, and J.-Y. Huang, "A five-focal-point method for the optimal design of a flat-top planar waveguide demultiplexer," submitted to *Journal of Lightwave Technology*.

## B. 國際會議論文

1. S.-H. Lin and J.-T. Lin, "Analysis and design of a concave grating using Rowland circle approximation," *Topical Meeting on Optics in Computing*, Grand Hotel, Taipei, Taiwan, R.O.C., April, 2002.
2. C.-T. Lin, Y.-T. Huang, J.-Y. Huang, and H.-H. Lin, "Integrated planar waveguide concave gratings for high density WDM systems," *The IASTED International Conf. on Optical Communication Systems and Networks (OCSN 2005)*, Banff, Alberta, Canada, July, 2005.
3. C.-T. Lin, Y.-T. Huang, and J.-Y. Huang, "16-Channel Optical Add-Drop Multiplexer Consisting of a Planar Waveguide Concave Grating," *The 6th WSEAS International Conference on System Science and Simulation in Engineering (ICOSSSE'07)*, Venice, Italy, Nov. 21-24, 2007.

## C. 國內會議論文

1. 林俊廷, 林烜輝, 周正三, 張哲瑋, 林暉雄, "微凹面型光柵分光元件的分析與應用," *2001 Optics and Photonics Taiwan '01*, pp. 295-297, Kaohsiung, Taiwan, R.O.C., Dec., 2001.
2. 林暉雄, 林俊廷, 傅同龍, 林宇仁, 周曉宇, "凹面型微光柵波長分波元件之設計與實現," *第六屆奈米工程暨微系統技術研討會*, Tainan, Taiwan, R.O.C., Dec., 2002.
3. 林暉雄, 林俊廷, 傅同龍, 林宇仁, 楊宗勳, 周曉宇, 陸懋宏, "側壁凹面型微光柵在光纖通訊上之應用與研究," *2002 Optics and Photonics Taiwan '02*, pp.509-511, Taipei, Taiwan, R.O.C., Dec., 2002.
4. C.-T. Lin, Y.-T. Huang, J.-Y. Huang, H.-H. Lin, Y.-J. Lin, and T.-L. Fu, "Integrated planar waveguide concave gratings for high density WDM systems," *2004 Optics and Photonics Taiwan '04*, Jhongli, Taiwan, R.O.C., Dec., 2004.
5. C.-T. Lin, Y.-T. Huang, J.-Y. Huang, and H.-H. Lin, "The three-focal-point optimal design of a flat-top planar waveguide concave grating for DWDM systems," *2005 Optics and Photonics Taiwan '05*, Tainan, Taiwan, R.O.C., Dec., 2005.
6. C.-T. Lin, Y.-T. Huang, J.-Y. Huang, and H.-H. Lin, "A planar waveguide concave grating employing a dielectric mirror," *2006 Optics and Photonics Taiwan '06*, Hsinchu, Taiwan, R.O.C., Dec., 2006.